Ivane Javakhishvili Tbilisi State University

Faculty of Exact and Natural Sciences
Department of Electrical and Electronics Engineering

Irma Shamatava

Subsurface metallic targets detection and classification using low frequency electromagnetic fields

Doctoral THESIS
To obtain academic degree of Doctor of Sciences in
Electrical and Electronics Engineering

Doctoral program manager:

Professor   Dr.   George Gvedashvili

Supervisor:
Professor   Dr.   Roman Jobava

Tbilisi 2015

ივანე ჯავახიშვილის სახელობის თბილისის სახელმწიფო უნივერსიტეტი

ირმა შამათავა

ზუსტ და საბუნებისმეტყველო მეცნიერებათა ფაკულტეტი
ელექტრული ელექტრონული ინჟინერიის დეპარტამენტი

მიწისქვეშა მეტალური ობიექტების დეტექტირება და კლასიფიცირება ელექტრომაგნიტური ველებით

ს ა დ ო ქ ტ ო რ ო დ ი ს ე რ ტ ა ც ი ა

ხელმძღვანელი:

სადოქტორო პროგრამის ხელმძღვანელი:
აკადემიური დოქტორი, პროფესორი გიორგი ღვედაშვილი

სამეცნიერო ხელმძღვანელი:
აკადემიური დოქტორი, პროფესორი რომან ჯობავა

თბილისი 2015 წელი

მოტივაცია

მიწისქვეშა აუფეთქებელი ჭურვების აღმოჩენა და განეიტრალება საკმარისად რთული და ძვირადღირებული პროცედურაა. ძირითადად დედამიწა მიწისქვეშა აუფეთქებელი ჭურვებით დანაგვიანდა ომებისა და სამხედრო წვრთნების პროცესში . ისეთ ქვეყნებშია კი, როგორიც ამერიკის შეერთებული შტატებია, სადაც არ ყოფილა სამამულო და სამოქალაქო ომები UXO-თი დანაგვიანებულია დაახლოებიტ 11 მილიონი აკრი (44515 კმ²) ხმელეთი,რაც საქართველოს ტერიტორიის 64%-ია და 10 მილიონი აკრი (4046.9 კმ²) წყალქვეშა ტერიტორია [1-7]. აღსანიშნავია, რომ მიწისქვეშა აუფეთქებელი ჭურვები დღემდე პრობლემად რჩება. ევროპის ქვეყნებში დღესაც გვხვდება დიდი რაოდენობით მიწისქვეშა აუფეთქებელი ჭურვები პირველი და მეორე მსოფლიო ომებიდან,ხოლო სამხრეთმოსავლეთ აზიის ქვეყნებში ეს ნაღმები 1964–1973 წლების ვიეტნამის ომებიდანაა შემორცენილი.ისტორიული მონაცემების მიხედვით, 1946 წლიდან საფრანგეთში მოგროვილი და განადგურებული იქნა 18 მილიონი საარტილერიო ჭურვი და 600 000 საჰაერო ბომბი. მხოლოდ ქალაქი ვირდიმის სიხლოვეს პირელი მსოფლიო ომის დროინდელი, დაახლოებით 12 მილიონი აუფეთქებელი ჭურვია აღმოჩენილი. გარდა ამისა, კუბის ტელევიზიის ინფორმაციით ესპანეთ-ამერიკის ომში გამოყენებული მიწისქვეშა ჭურვების აფეთქების შვიდი შემთხვევა არის დაფიქსირებული ბოლო 30 წლის მანძილზე.

მიწისქვეშა აუფეთქებელი ჭურვები უდიდესი პრობლემაა ყოფილი საბჭოთა კავშირის ქვეყნებში. საბჭოთა არმიას სოფელ აგსტაფაში აზერბაიჯანის ტერიტორიაზე ჰქონდა 138 ბუნკერისაგან შემდგარი ჭურვების საწყობი, რომელიც განსაზღვრული იყო მთელი სამხრეთ კავკასიისთვის. 1991 წელს, როდესაც საბჭოთა კავშირი დაინგრა, რუსეთის არმიამ გადაწყვიტა ამ ბუნკერების აფეთქება. რა თქმა უნდა, ყველა ჭურვი არ განადგურდა და ათასობით მიწისქვეშა აუფეთქებელი ჭურვი მიმოიფანტა დაახლოებით 4400 ჰექტარზე. აზერბაიჯანის მთავრობის მონცემების თანახმად ბოლო 20 წლის განმავლობაში რამდენიმე ჭურვის აფეთქებაა დაფიქსირებული. ერთ-ერთ ასეთ აფეთქებას 32 ადამიანის სიცოცხლე შეეწირა.

პრობლემები შეიქმნა ბოლო ომებისა და ეთნიკური კონფლიქტების ზონებშიც, მათ შორის საქართველოში. უკანასკნელი 2008 წლის რუსეთ-საქართველოს ომის დროს გამოყენებული იყო კლასტერული ბომბები, რომლებიც განსაკუთრებით საშიშია მშვიდობიან მოსახლეობისთვის და რომლის მსხვერპლი უმეტესად ბავშვები არიან.ზემოჩამოთვლილი პრობლემებიდან გამომდინარე აუფეთქებელი ნაღმებით დანაგვიანებული ტერიტორიების გაწმენდა მსოფლიოს ყველა ქვეყნის ერთ-ერთ უმთავრეს ამოცანას წარმოადგენს.

ნაღმების ძირითადი შემადგენელი ნაწილი არის მეტალი, რაც მეტალდეტექტორებით მათი მარტივად დეტექტირების საშუალებას იძლევა. სამწუხაროდ ასეთი სენსორები რეაგირებენ არა მარტო აუფეთქებელ ჭურვებზე, არამედ ნებისმიერ მიწისქვეშა მეტალურ სხეულზე. უკანასკნელ წლებში სამხედრო ტერიტორიებზე ჩატარებულმა სამუშაოებმა აჩვენა, რომ დეტექტირებულ სხეულთა 95% არის აფეტქე ბული ჭურვის ნარჩენები, რაც არანაირ საფრთხეს არ წარმოადგენს. ამიტომ

დანაგვიანებული ტერიტორიების სწრაფი უზიფათო საჭირო გახდა ახალი ტექნოლოგიების შექმნა, რომლებიც მოახდენენ არა მარტო სხეულების დეტექტირებას, არამედ მათ ზუსტ იდენტიფიცირებასაც. უკანასკნელი ორი ათწლეულის განმავლობაში ინტენსიური კვლევის საფუძველზე დადგინდა, რომ დაბალსიხშირული ელექტრომაგნიტური ინდუქციით ზონდირების ტექნოლოგია მიწისქვეშ მეტალური სხეულების დეტექტირებისა და იდენტიფიცირების საუკეთესო საშუალებას წარმოადგენს.

დანაგვიანებული ტერიტორიების მიწისქვეშ აუფეთქებელი ჭურვებისგან გაწმენდის პროცესი შედგება სამი ძირითადადინაწილისგან: 1)მონაცემების შეგროვება სენსორ-დეტექტორების საშუალებით; 2)მონაცემების დამუშავება და აღმოჩენილი ობიექტების ფიზიკური ფიზიკური პარამეტრების დადგენა; და 3) მონაცემებიდან მიღებული მონაცემებიდან მიღებული ფიზიკური პარამეტრების მეშვეობით მიწისქვეშ ობიექტების იდენტიფიცირება.

მოცემული ნაშრომი ეძღვნება ზემოაღნიშნული პროცესის სამივე ეტაპს. კერძოდ, ნაშრომი აერთიანებს ფიზიკურად სრულყოფილი პირდაპირი და შებრუნებული ამოცანების იმ მეთოდებს, რომლებიც თანამედროვე გეოფიზიკური სენსორების მონაცემების ეფექტური დამუშავებით საიმედო და ზუსტ UXO დისკრიმინაციის საშუალებას იძლევიან.

- *ნაშრომის მიზანი და ძირითადი შედეგები:*

- *სადისერტაციო ნაშრომის მთავარი მიზანია ფიზიკურად სრულყოფილი პირდაპირი და შებრუნებული ამოცანების ამოხსნის მეთოდოლოგიის შემუშავება, მათი გამოყენებით დაბალსიხშირული EMI-ის პრინციპზე დაფუძნებული სენსორების მონაცემთა დამუშავების სპეციალური, ეფექტური მეთოდიკის შექმნა.*

- *ზემოაღნიშნული მიზნების მისაღწევად სადისერტაციო ნაშრომში შემუშავებული და წარმოდგენილია:* ჰიბრიდული, დამხმარე წყაროებისა (MAS) და ე.წ. თხელი სასაზღვრო ფენით აპროქსიმაციის მეთოდების (TSA) [1] კომბინაცია EMI-იის მოვლენის ფიზიკური არსის შესასწავლად;

- ნორმალიზებული ზედაპირული მაგნიტური წყაროების მეთოდი (NSMS) [2]. EMI სენსორების მონაცემთა ინვერტირებისათვის და მიწისქვეშ UXO ობიექტების კლასიფიცირებისათვის; ორთონორმალიზებული მოცულობითი მაგნიტური წყაროების მეთოდი (ONVMS) [3] ახალი თაობის EMI სენსორთა სისტემის მონაცემთა ანალიზისათვის და მიწისქვეშ UXO ობიექტების კლასიფიცირებისათვის.

- სადისერტაციო ნაშრომში წარმოდგენილია ზემოთ ჩამოთვლილი მეთოდების კომბინაცია სიგნალების დამუშავების და ინვერტირების თანამედროვე მეთოდებთან, როგორიცაა:

- ერთობლივი დიაგონალიზაციის მეთოდი, თანამედროვე გეოფიზიკური EMI სენსორების მულტისტატიკური მატრიცის საკუთარი მნიშვნელობების დასადგენად და მონაცემთა წინასწარი დამუშავებისათვის (JD) [4];

- დიფერენციალური ევოლუციის მეთოდი, მი�წისქვშა UXO ობიექტების ორიენტაციისა და მდებარეობის (DE) დასადგენად [2, 5 მაგნიტური ველის, ვექტორული და სკალარული პოტენციალების მეთოდი (HAP) UXO ობიექტის ლოკალიზაციისათვის [6].

ზემოაღნიშნული სიგნალთა დამუშავების პირდაპირი და შებრუნებულ ალგორითმები გამოყენებულ იქნა თანამედროვე EMI სენსორების მონაცემების დამუშავებისა და UXO ობიექტთა კლასიფიცირებისათვის. კერძოდ:

- შექმნილია სპეციფიური მონაცემთა ბიბლიოთეკა, რომელიც შეიცავს წინასწარგანსაზღვრული კლასის UXO ობიექტების ეფექტურ პოლარიზაციას მონაცემთა ბაზის სახით. EMI სენსორებით შეგროვილი მონაცემებისა და ამ ბიბლიოთეკის მონაცემთა ურთიერთშედარების გზით ხორციელდება UXO ობიექტების კლასიფიცირება და იდენტიფიცირება.

- შემუშავებული მეთოდები ადაპტირებულია თანამედროვე EMI სენსორებისთვის, როგორებიცაა: MetalMapper, TEMTADS, MPV, BUD [7].

შექმნილია მონაცემთა სპეციალური ბაზა, რომელიც შეიცავს UXO–თი დაბინძურების დეტალურ ინფორმაციას შემდეგი სამხედრო ბაზებისათვის: Camp Sibert – alabama, Camp San Luis Obispo – კალიფორნია და Camp Butner - ჩრდილოეთ კაროლაინა.

დისერტაციის სტრუქტურა

დისერტაცია შედგება სამი თავისაგან.

პირველი თავში აღწერილია დაბალსიხშირული ელექტრომაგნიტური ინდუქციით (EMI) ზონდირების მეთოდის თეორიულ საფუძვლები, რომელიც განსაზღვრავენ თანამედროვე გეოფიზიკური სესორ-დეტექტორების მუშაობის ზირითად პრინციპს.

ნაშრომში მიმოხილულია და შემუშავებულია დაბალსიხშირული ელექტრომაგნიტური ტალღების გაბნევის ამოცანების ამოხსნის რამდენიმე მეთოდი.

კერძოდ:

დამხმარე გამომსხივებლების მეთოდი (MAS), რომელიც წარმატებით გამოიყენება ელექტრომაგნიტური ტალღების გაბნევის ამოცანების ამოხსნისას სხვადასხვა ზომისა თუ ფორმის სხეულებისთვის. ეს მეთოდი საკმარისად მოსახერხებელი აღმოჩნდა მიმღებ-გადამცემი EMI სენსორებისა და სენსორთა

სისტემების მოდელირებისას; შემუშავებულია დამხმარე წყაროებისა და თხელი, სასაზღვრო ფენის (thin skin depth) კომბინირებული მეთოდოლოგია ელექტრომაგნიტური ამოცანების ამოსახსნელად მაღალი გამტარებლობის მქონე მეტალური და მაგნიტური სხეულებისთვის ფართო სიხშირულ დიაპაზონში .

წარმოდგენილია, სხეულების მიერ არეკვლილი ელექტრომაგნიტური სიგნალის მიახლიებითი აღსაწერის ექვივალენტური დიპოლური მოდელი. დიპოლური მოდელის მიხედვით მთელი სხეულის მიერ არეკვლილი სიგნალი შეცვლილია ერთი ექვივალენტური დიპოლის გამოსხივებით, რომელიც მოთავსებულია სხეულის გეომეტრიულ ცენტრში. ეს მიახლოება კარგად მუშაობს მცირე ზომის ერთგვაროვანი სხეულებისთვის, როდესაც მანძილი სხეულსა და სენსორს შორის რამოდენიმე სხეულის ზომის რიგისაა, მაგრამ იძლევა არასასურველ ცდომილებას არაერთგვაროვანი, რეალური UXO სხეულებისათვის;

განმხოლოებული, არაერთგვაროვანი სხეულიდან არეკვლილი სიგნალების დიდი სიზუსტით მოდელირებისათვის, შემუშავებულია ნორმალიზებული ზედაპირული მუხტების მეთოდი (NSMS).

NSMS დაფუძნებულია ჰიუგენსის პრინციპზე და მუხტებს ანაწილებს წარმოსახვით ჩაკეტილ ზედაპირებზე. ამ მუხტების მნიშვნელობები გამოითვლება EMI სენსორებით გაზომილი მონაცემებით და სრული მუხტის ეს მნიშვნელობა გამოიყენება სხეულების იდენტიფიცირებისათვის. ეს მეთოდიკა ეფექტურად მუშაობს არაერთგვაროვანი, განმხოლოებული სხეულებისთვის, მაგრამ ჩვეულებრივად, რეალურ სიტუაციაში აუფეთქებელი ბომბის გარშემო ყოველთვის არის რამდენიმე აფეთქებული ჭურვის ნაწილები.

მრავალი სხეულის იდენტიფიცირებისა და ლოკალიზაციის პრობლემის გადასაწყვეტად შემუშავებულ იქნა, ორთონორმირებული მოცულობითი მაგნიტური წყაროების მეთოდი (ONVMS) .

ONVMS მეთოდიკა ეფექტურად გამოიყენება როგორც განმხოლოებული, ასევე მრავალი სხეულის იდენტიფიცირება-ლოკალიზაციისათვის. თანამედროვე გეოფიზიკურ სენსორები შედგება რამდენიმე გადამცემისა და მიმღებისაგან და ამ სენსორებიდან მიღებული ინფორმაციის სრული დამუშავება ხდება ე.წ. ერთობლივი დიაგონალიზაციის მეთოდით. ერთობლივი დიაგონალიზაციის მეთოდი საშუალებას იძლევა შებრუნებული ამოცანის ამოხსნის გარეშე პირაპირ, გაზომილი მონაცემებით დადგინდეს დეტექტირებულ სხეულთა რაოდენობა და ხშირ შემთხვევაში მოხდეს მათი ზუსტი იდენტიფიცირება/ლოკალიზაცია.

ვინაიდან, UXO ობიექტების საიმედო იდენტიფიცირების პრობლემა, როგორც წესი, შებრუნებული ამოცანის ამოხსნაზე დაიყვანება, მეორე თავში აღწერილია ამ ამოცანების ამოხსნის სხვადასხვა მეთოდიკა, რისთვისაც აუცილებელია აუფეთქებელი ჭურვების ადგილმდებარეობის, ორიენტაციისა და ფიზიკური პარამეტრების საკმარისად ზუსტი წინასწარი დადგენა. ერთ-ერთი ასეთი ფიზიკური პარამეტრია, მაგალითად, მაგნიტური პოლარიზაცია სხეულის ღერძის გასწვრივ. თავის მხრივ, სხეულის მდებარეობისა და ორიენტაციის დადგენა დაიყვანება არაწრფივი ამოცანების ამოხსნაზე, ხოლო მაგნიტური პოლარიზაცია, რომელიც არის ყოველი სხეულის უნიკალური მახასიათებელი, და გამოიყენება მათი კლასიფიცირებისათვის, მოითხოვს წრფივი ამოცანების ამოხსნას. როგორც წესი, არაწრფივი ამოცანების ამოსახსნელად იყენებენ კარგად ცნობილ გრადიენტული მინიმიზაციის მეთოდს, რომელიც ჩვეულებრივად, ძალზე მგრძნობიარეა ლოკალური მინიმუმების მიმართ, ამიტომ დისერტაციაში განიხილება პირდაპირი ძებნის ალგორითმი (დიფერენციალური ევოლუცია), რომელიც ყოველთვის იძლევა გლობალური მინიმუმის მოძებნის გარანტიას. ანაშრომში დიფერენციალური ევოლუცია არის კომბინირებული NSMS და OVNSMS მეთოდებთან, ხოლო სხეულის ადგილმედებარეობის სწრაფად და ზუსტად დადგენისათვის შემუშავებულია HAP მეთოდი, რომელიც ობიექტის ადგილმდებარეობას განსაზღვრავს მის მიერ გამოსხივებული მაგნიტურ ველის, ვექტორულ და სკალარულ პოტენციალებს საშუალებით.

მესამე თავში წარმოდგენილია და აღწერილია ახალი თაობის EMI სენსორები , METALMEPPER, TEMTADS, MPV da BUD სისტემები, რომლებიც ნაშრომში გამოყენებულია სამხედრო ბაზებზე UXO ობიექტების დეტექტირებისა და იდენტიფიცირებისათვის. აქვე წარმოგიდგენილია ამ კვლევის შედეგები რეალური სამხედრო ბაზების პოლიგონებიდან, კერძოდ, Camp Sibert alabamidan, Camp San Luis Obispo-კალიფორნიიდან და Camp Butn ჩრდილოეთ კაროლაინადან.

Motivation

The detection and removal of buried unexploded ordnance (UXO) is an expensive and difficult task. In the United States, an estimated 11 million acres(44515 km², which is about 64 % of entire Georgia's territory) of land and one million acres (4046.9 km²) of underwater lands may be contaminated with UXO [1-7]. Some of these lands are military practice ranges, to be turned over to the public for recreation or economical Exploitation; others are the sites of long passed conflicts. UXO may remain dangerous over many years. Cuban television reported the detonation of a projectile in Santiago Harbor, some 100 years after it was fired during the Spanish American War. Cuban sources noted that it was the seventh such piece of ordnance from the war to explode in Cuba over the past thirty years. On a vastly larger scale, since 1946 the French Department du Dominate has collected and destroyed more than 18 million artillery shells and 600,000 bombs dropped from airplanes. However, near the city of Verdun, alone, it is estimated that there are about 12 million unexploded shells still remaining from World War 1, many in degraded condition and containing toxic materials. Elsewhere in France are sites where hundreds of thousands or even millions of missiles rained down upon the landscape during that conflict, sometimes only within a matter of hours or days.

During the First World War overall about 15% of bombs failed to detonate. Thus, even after all the intervening time, the remains of this and other conflicts pose an enormous problem in the present. Including military training areas and regions where peaceful uses of ordnance were attempted, the problem of buried UXO is terribly widespread, from the jungles of Vietnam and the warm beaches of Puerto Rico and Hawaii, to the glaciers of British Columbia and the Aleutian Islands in Alaska.

The problem is more acute in European countries, where millions of buried UXOs remain from two world wars, as well as in south East Asian countries. For an example, by an estimate about 270 million bombs were dropped in Laos between 1964 and 1973. Out of this 80 million bombs failed to explore and still remains dangerous for public.

The UXO continues to pose problem at active and former Soviet Union military bases. Such as in Saloglu village, Agstafa district of Azerbaijan soviet army had the largest warehouses in the South-Caucasus region, consisting of 138 bunkers. In 1991, when Azerbaijan regained independence, the warehouse was destroyed by the soviet army before departing. As the result of the explosion thousands pieces of UXO were scattered over a large area of 4,400 hectares continuously posing a serious humanitarian, socio-economic and environmental threat to the local population. Since the explosion, 152 UXO-related accidents with 32 people killed were reported.

The problems have been worsening due to recent wars and ethnic conflict in worldwide, including my country of Georgia. During recent Russia-Georgia war in 2008, cluster bombs were dropped in Georgia. A cluster bomb consists of a few dozens of smaller sublimations that are dispersed before detonation, to ensure coverage of the widest area possible. Part of the

bumblers detonate at the cluster bomb's initial use. The rest of them remain on the surface as landmines. Children are consequently the most common victims of these landmines. Munitions of the sort were used in Iraq, Kosovo, Afghanistan, Lebanon, Vietnam and other places.

Mostly UXO are metallic or containing substantial metallic parts, which makes them easily detectable with current metal detectors. However, metal detectors detect not only UXO-s, they also detect all metallic targets as well. Recent studies have showed that, the over whelming task of finding and removing these UXOs is hampered by the fact that approximately 95 % of the costs are spent for digging non-UXO targets. Hence, accurate Discrimination techniques are needed. Over last two decades, low frequency electromagnetic induction sensing technology has merged as ultimate tool for subsurface UXO targets detection and discrimination.

Overall, UXO cleanup process consists three main parts: 1) Subsurface targets detection using geophysical sensors; 2) The data processing and targets parameters extraction by solving inverse electromagnetic induction problems; 3) Targets classification as UXO and non-UXO targets using the extracted targets parameters. This thesis describes all upon mentioned three parts for UXO classification. Namely, the work combines advanced physically complete forward and inverse methods, which provide effective and accurate UXO classification from current state of the art geophysical tensors data.

Objective and main results

The main objective of this work was to develop physically complete forward and inverse models in combination with state-of-the-art signal processing methodologies for robust UXO discrimination at live UXO sites using advanced electromagnetic induction (EMI) sensors data sets.

To achieve this objective, in this thesis:

We developed/extended physically complete forward approaches:

- Hybrid MAS/TSA algorithm [1] for understanding underline physics of EMI phenomenon.
- Normalized surface magnetic source model (NSMS) [2] for EMI sensors data inversion and classification.
- Orthonormalized volume magnetic source model (ONVMS) [3] for next generation EMI systems data analysis and subsurface multiple targets classification.

These models were combined with advanced signal processing and data-inversion approaches, which provided robust regularization and classification feature parameters estimations for targets intrinsic, such as magnetic polarizabilities, multi-static data matrix eigenvalues, and extrinsic, i.e. targets locations and orientations. These advanced signal processing algorithms are:

- Joint diagonalization for multi-target data pre-processing (JD) [4]
- Differential evolution (DE) [2, 5] for estimating targets locations and orientations.
- A field-potential (HAP) method to locate targets [6].

Our advanced forward-inverse and signal processing algorithms have been applied to next generation sensors data sets collected at several live UXO sites.

➢ We developed site specific UXO libraries for each live UXO sites. These libraries were used for targets classification via a finger-print matching technique.

➢ Our models were adapted to all next-generation sensors, including the MetalMapper, TEMTADS, MPV, and BUD, data sets. The models were applied to blind live-site UXO discriminations studies [7]. The studies have demonstrated the excellent discrimination capabilities.

The theses structure:

Theses consist three main parts: first part provides a road map for implementing forward and inverse electromagnetic induction numerical methods for UXO detection and classification from basic physics to live UXO discrimination studies. In a real field the electromagnetic signals become convoluted with noise due to the instrument, magnetic soil and widespread background clutter. To understand and account for different noise source, the thesis provides mathematical fundamentals, physical meanings and practical realizations of forward and inverse signal processing approaches for unexploded

Specifically,

First the thesis outlines the combined Method of Auxiliary Sources (MAS) and thin skin approximation (TSA), which is an advanced, physically complete forward EMI model, for solving low frequency electromagnetic induction problems involving metallic objects placed in heterogeneous magnetic and conducting soils. Then, the normalized surface magnetic source (charge/dipole) model (NSMS), and ortho-normalized volume magnetic source (ONVMS) technique are presented for accurately representing the EMI responses of subsurface metallic targets. Third, we formulate and develop an inversion framework featuring robust regularization and parameter-determination methodologies (for both linear intrinsic signatures and non-linear extrinsic particulars) based on advanced signal processing algorithms. Namely, the models were combined with EMI data inversion approaches, such as the gradient search, direct search-differential evolution and etc., for extracting targets intrinsic (effective dipole polarizabilities) and extrinsic (locations and orientations) from advanced EMI sensor data; Fourth, We combine EMI models and classification methodologies to process complex,

heterogeneous geophysical data, and finally we demonstrate the discrimination capability of the combined approach by applying it to blind live-site UXO discrimination studies.

Overview of Chapter 1

The chapter 1 outlines the theoretical basis of the detailed 3d EMI solvers, and advanced fast EMI forward models that we use to study low frequency EMI scattering phenomena and to represent the EMI response of obscured targets, respectively. We first present the Method of Auxiliary Sources (MAS) and thin skin approximation (TSA) for solving EMI problems in great details. Then we show the single-dipole model, which is usually insufficient in itself for representing targets EMI signals accurately. After that we introduce and study in detail the NSMS model, which distributes dipoles on a closed surface surrounding a target of interest. And then we derive and describe the ONVMS technique, which infuses dipoles throughout the subsurface volume illuminated by a sensor. We end by describing a data-preprocessing technique based on joint diagonalization that estimates the number of targets in a measurement with no need for data inversion; the method, moreover, can provide initial estimates of target locations and perform rudimentary discrimination.

The Method of Auxiliary Sources (MAS) for solution of the full electromagnetic (EMI) problem for penetrable, highly conducting and permeable metallic targets. The MAS is a numerical technique, originally designed for solving various electromagnetic radiations and scattering problems. It has been demonstrated that the MAS is a robust, easy to implement, accurate and sufficient method for studying a wide range of electromagnetic problems, such as investigation of waveguide structures, antennas, scattering, electromagnetic wave propagation in complex media, etc. Later MAS successfully was combined with small penetration approximation (SPA) and thin skin approximations (TSA) for analysis of low frequency EMI scattering phenomena. In standard MAS for EMI, boundary value problems are solved numerically by representing the electromagnetic fields in each domain of the structure under investigation by a finite linear combination of analytical solutions of the relevant field equations, corresponding to sources situated at some distance away from the boundaries of each domain.

EMI scattering responses are usually expressed in terms of the induction number. It is well established that the electromagnetic field inside a conductor decays over distances of the order of the skin depth. This reduces the efficiency and accuracy of the MAS at high induction numbers due to singularities that appear in the scattering matrix. To overcome this problem, a combined MAS-thin skin approximation (MAS-TSA) has developed. The TSA is based on the divergence-free Maxwell's equation for the magnetic field and it approximates magnetic fields normal derivatives with magnetic field on the targets surface. The model has been used to solve a variety of EMI problems from the magnetostatic regime up to 1 MHz for land-based UXO detection and discrimination.

In general UXO discrimination is a non-linear inverse problem, which requires high fidelity forward models. The most frequently used method for representing the EMI response of a

metallic target in both frequency and time domains approximates the whole object with a set of orthogonal co-located point dipoles that fire up in response to the primary field; the induced dipole moment is related to the primary field through a symmetric polarizability tensor. The use of this dipole approximation is motivated by its speed and simplicity; this simplicity, however, rests on assumptions that often become problematic and limit the model's usefulness. One such assumption is that the buried target of interest is either far enough from the transmitter loop, or small enough, that the primary field is essentially uniform throughout its extent. Usually, complex targets composed of different materials and different sections that contribute appreciably to the response—and, in the case of UXO, containing such complicating features as fins and rings—simply cannot be modeled accurately with a single point dipole. Such cases require more advanced methods that will capture the underlying physics correctly. One such technique is the NSMS model.

The NSMS method can be considered as a generalized surface dipole model, and indeed reduces to the point dipole model in a special limiting case. The NSMS approach models an object's response to the primary field of a sensor by distributing a set of equivalent elementary magnetic sources—normally oriented dipoles in this case—over an auxiliary surface that surrounds it. Such a surface distribution can be hypothetically generated by spreading positive magnetic charge over the outer side of the equivalent surface (usually a prolate spheroid) and an identical distribution of opposite sign on its inner side, resulting in a double layer of magnetic charge separated by an infinitesimal distance. This double layer introduces the proper discontinuities in the tangential components of the magnetic flux density vector but does not affect the transition of its normal component, which must always be continuous given the lack of free magnetic charges in nature. The resulting magnetic-moment distribution radiates a field that by construction satisfies the governing EMI equations and can thus account for the secondary field outside the object. The particulars of location and orientation are divided out by normalizing the dipole density at every point with the component of the primary magnetic field normal to the surface. The resulting surface amplitude of the NSMS distribution is a property of the object, and its integral over the surface constitutes a sort of global magnetic polarizability that is independent of the computational constructs—primary field, surrounding surface, object location and orientation, etc.—introduced for its determination. The surface amplitude can be determined directly for library-matching purposes by minimizing the difference between measured and modeled data for a known combination of object and sensor at a given relative location and orientation.

The NSMS technique has demonstrated good computational speed and superior classification performance when applied to EMI datasets consisting of well-isolated single targets, but is found to degrade quickly on both counts when confronted with multi-target cases. This has forced us to generalize the model further and develop the ONVMS procedure. The ONVMS model, a further extension of NSMS, is based on the assumption that a collection of subsurface objects can be replaced with a set of magnetic dipole sources, distributed over a volume. Since all actual radiating sources are located within the scatterers—rather than in the soil or air—the spatial distribution of these fictitious dipoles (their amplitudes scaled by the primary field)

indicates the locations and orientations of any targets present inside the computational volume. The great advantage of the ONVMS technique over the other models discussed above is that it takes into account mutual couplings between different sections of the different targets while simultaneously avoiding the appearance of singular matrices in multi-target situations. It is thus gracefully indifferent to the number of targets: Once the amplitudes and the locations of the corresponding dipoles are determined, one need only look at their clustering patterns, compute the time-dependent total polarizability tensor for each group, and subsequently diagonalize each such tensor using joint diagonalization. The resulting diagonal elements have been found to be intrinsic to the objects they represent, and can be used, on their own or combined with other quantities, in discrimination analysis. Recent ESTCP live-site discrimination studies have clearly indicated the superior discrimination performance of the ONVMS method in combination with the statistical processing approaches described below.

One of the main challenges one faces when attempting multi-target inversion and classification is the inability to estimate the number of targets. In order to overcome this problem, we implemented a technique based on joint diagonalization that estimates the number of targets present in the field of view of the sensor as it takes a data shot, in real time and without requiring a forward model, and, in a good number of cases, even provides the capability to perform a quick inversion-free characterization and classification of these targets. JD determines the eigenvalues and eigenvectors of a square time- or frequency-dependent multi-static response (MSR) matrix synthesized directly from measured data. The number of nonzero eigenvalues of the matrix (i.e., those above a noise threshold) is related to the number of elementary sources in the illuminated cell; moreover, the time-decay patterns of these non-vanishing eigenvalues are intrinsic properties of the targets to which the sources correspond and can ultimately provide dependable classification features.

Overview of Chapter 2

 Chapter 2 discusses inverse models: the methods used to harness the forward models so they provide relevant intrinsic and extrinsic information starting from measured data. After presenting some traditional gradient-search based methods and pointing out some of their limitations we describe differential evolution (DE), a state-of-the-art global-search method, similar in character to genetic algorithms, that has shown remarkable flexibility and usefulness. We end by describing the HAP method, a semi-analytic non-iterative procedure to locate buried targets.

Determining a buried object's orientation and location is a non-linear problem. Inverse-scattering problems are solved by determining an objective function, as a goodness-of-fit measure between modeled and measured magnetic field data. Standard gradient search approaches often suffer from a surfeit of local minima that sometimes result in incorrect estimates for location and orientation. To avoid this problem we recently developed a different class of global optimization search algorithms. One such technique is the Differential Evolution(DE) method, a heuristic, parallel, direct-search method for minimizing non-linear functions of continuous variables that is very easy to implement and has good convergence

properties. We combined DE with ONVMS to invert digital geophysical EMI data. All EMI optimizations were split into linear and nonlinear parts, iterating between them to minimize the objective function. Once the target locations are found, the amplitudes of responding ONVMS are determined and used to classify the object relative to items of interest.

In the EMI regime, the secondary magnetic fields measured by the EMI receivers are induced by eddy currents magnetic dipoles which are distributed non-uniformly inside the scatterer. There are some particular points, named "scattered field singularities" (SFS), where most of these sources are concentrated. Recent studies show that under certain conditions the entire scatterer can be replaced with several responding elementary sources by putting them at SFS points. We have found a new analytic expression for estimating the location, orientation, and polarizability elements of a buried object starting from measured EMI data without solving traditional ill-posed inverse-scattering problems. The algorithm (dubbed "HAP") is based on the fact that a target's response can be approximated by dipole sources concentrated at SFS points. It utilizes three global values at a single location in space: (1) the magnetic field vector $\mathbf{H}$, (2) the vector potential $\mathbf{A}$, and (3) the scalar magnetic potential ψ. Since among these quantities only the $\mathbf{H}$ field (and sometimes only one of its components) is measurable, we employ a variation of the NSMS model to obtain $\mathbf{A}$ and ψ we distribute elementary sources on an auxiliary planar layer, located between the sensor and the object, and find their amplitudes by fitting measured data.

Overview of Chapter 3

Chapter 3 presents and describes the next-generation EMI sensors—the METALMEPPER, the TEMTADS array, the MPV portable instrument, and the BUD system—that took all the data we use and that represent the state of the UXO remediation hardware. We present the results of several testing and validation studies carried out on laboratory, test stand and US army standardized Aberdeen Proving Ground in Maryland test-site data from these devices. Also Provides a detailed account of the discrimination and classification studies performed on data from actual UXO sites—the Camp Sibert in Alabama, Camp San Luis Obispo in California, and Camp Butner in North Carolina—in which several combinations of the techniques presented in the previous chapters were used. We describe our solution strategies and the results we obtained.

References

1. F. Shubitidze, K. O'Neill, K. Sun, I. Shamatava, and K.D. Paulsen, "A hybrid full MAS and combined MAS-TSA algorithm for broadband electromagnetic induction problem", *Applied computational electromagnetic society Journal*, pages: 112-126, March, 2004.

2. F. Shubitidze, K. O'Neill, B.E. Barrowes, I. Shamatava, J.P. Fernández, K. Sun and K.D. Paulsen, "Application of the normalized surface magnetic charge model to UXO discrimination in cases with overlapping signals", *Journal of Applied Geophysics Vol 61 Issues 3-4, 2007* Pages 292-303.

3. F. Shubitidze, J. P. Fernández, B. E. Barrowes, I. Shamatava, A. Bijamov, K. O'Neill, D. Karkashadze, "The Orthonormalized Volume Magnetic Source Model for Discrimination of Unexploded Ordnance," *IEEE Transactions on Geoscience and Remote Sensing,* vol 8, pp 5218-5229.

4. F. Shubitidze, J. P. Fernández, I. Shamatava, B. E. Barrowes, and K. O'Neill, "Joint diagonalization applied to the detection and discrimination of unexploded ordnance," *Geophysics*, vol. 77, no. 4, pp. WB149–WB160, 2012.

5. F. Shubitidze, K. O'Neill, I. Shamatava , K. Sun , and K. D. Paulsen. 2005, "Combined differential evolution and surface magnetic charge model algorithm for discrimination of UXO from non-UXO items: Simple and general inversions", Proceeding SPIE, Defense and Security, Orlando, Fl, 2005, 12 pages.

6. F. Shubitidze, D. Karkashadze, B. E. Barrowes, I. Shamatava, and K. A. O'Neill, "A New Physics-based Approach for Estimating a Buried Object's Location, Orientation and Magnetic Polarization from EMI Data," *Journal of Environmental and Engineering Geophysics,* vol. 13, pp. 115-130, Sep 2008.

7. A. Bijamov, F. Shubitidze, J. P. Fernández, B. E. Barrowes, I. Shamatava,and K. O'Neill, "Camp Butner live-site UXO classification using hierarchical clustering and Gaussian mixture modeling," *IEEE Trans. Geosci.Remote Sens.*, vol. 52, no. 8, pp. 5218–5229, Aug. 2014

Contents

List of figures

List of Acronyms

3D	Three-Dimensional
AIC	Akaike Information Criterion
APG	Aberdeen Proving Ground
BIC	Bayesian Information Criterion
BOR	Body of Revolution
BUD	Berkeley UXO Discriminator
cm	Centimeter
CRREL	Cold Regions Research and Engineering Laboratory
DE	Differential Evolution
DGPS	Differential Global Positioning System
DoD	Department of Defense
DOE	Department of Energy
EM	Expectation Maximization
EMI	Electromagnetic Induction
ESTCP	Environmental Security Technology Certification Program
FD	Frequency Domain
GSEA	Generalized Standardized Excitation Approach
HAP	(1) magnetic field vector $\mathbf{H}$, (2) vector potential $\mathbf{A}$, (3) scalar magnetic Potential ψ
Hz	Hertz
ID	Identification
LS	Least Squares
m	Meter
MAS	Method of Auxiliary Sources
MD	Multi-Dipole
MDL	Minimum Description Length
MEG	Magnetoencephalographic
ML	Maximum Likelihood
mm	Millimeter
ms	Millisecond
μs	Microsecond
MM	MetalMapper
MNM	Multivariate Normal Mixture
MPV	Man-Portable Vector
MT	Mixed Theory
MUSIC	Multiple Signal Classification
NMMS	Non-metric Multidimensional Scaling
NRL	Naval Research Laboratory
NSMC	Normalized Surface Magnetic Charge
NSMS	Normalized Surface Magnetic Source
ONVMS	Ortho-Normalized Volume Magnetic Source Model

PCA	Principal Component Analysis
PNN	Probabilistic Neural Network
RBF	Radial Basis Function
ROC	Receiver Operating Characteristic
RSS	Residual Sum of Squares
RTS	Robotic Total Station
SEA	Standard Excitation Approach
SFS	Scattered Field Singularities
SLO	San Luis Obispo
SNR	Signal-to-Noise Ratio
SS	Sum of Squares
SVM	Support Vector Machine
TD	Time Domain
TEM	Time Domain Electromagnetic
TEMTADS	Time Domain Electromagnetic Towed Array Detection System
TNLL	Twice-Negative Log-Likelihood Function
TOI	Target Of Interest
TSA	Thin Skin Approximation
UXO	Unexploded Ordnance
VRM	Viscous Magnetic Remanenc

Abstract

Unexploded Ordinances (UXO) cleanup is one of most pressing environmental problems worldwide. Most if not all UXO are metallic or containing substantial amount of metals. Therefore they can easily be detected with metal detectors. However, the well-known and prohibitive cost of carefully excavating all geophysical anomalies detected at lands contaminated with unexploded ordnance (UXO) is one of the greatest impediments to performing an efficient and thorough cleanup of former battlefields and of USA Department of Defense (DOD) and Department of Energy (DOE) sites. Thus there are argent needs for innovative discrimination techniques that can quickly and reliably distinguish between hazardous UXO and non-hazardous metallic items. The key to success lies in the development of advanced processing techniques that can analyze and process sophisticated magnetic or electromagnetic induction data, with its novel waveforms, ever improving quality, and vector or tensor character, so as to maximize the probability of correct classification and minimize the false-alarm rate.

This thesis provides a road map for implementing forward and inverse electromagnetic induction numerical methods for UXO detection and classification from basic physics to live UXO discrimination studies. It develops and validates innovative, robust, and practical approaches for UXO localization and classification under realistic (noisy, cluttered background) field conditions by combining advanced electromagnetic induction (EMI) forward and inverse models. In a real field the electromagnetic signals become convoluted with noise due to the instrument, magnetic soil and widespread background clutter. To understand and account for different noise source, the thesis provides mathematical fundamentals, physical meanings and practical realizations of forward and inverse signal processing approaches for unexploded ordnance (UXO) detection and discrimination at live-UXO sites.

Namely, first the thesis outlines the Method of Auxiliary Sources (MAS), which is an advanced, physically complete forward EMI model, for solving low frequency electromagnetic induction problems involving metallic objects placed in heterogeneous magnetic and conducting soils.

Then, the normalized surface magnetic source (charge/dipole) model (NSMS), and ortho-normalized volume magnetic source (ONVMS) technique are presented for accurately representing the EMI responses of subsurface metallic targets. The models were combined with EMI data inversion approaches, such as the gradient search, direct search-differential evolution and etc., for extracting targets intrinsic (effective dipole polarizabilities) and extrinsic (locations and orientations) from advanced EMI sensor data; third we used extracted intrinsic parameters for discriminating UXO targets from non-hazardous anomalies.

Finally, the combined advanced EMI forward, inverse and classification models were applied to ESTCP live site UXO data sets. Live site discrimination studies showed the excellent discrimination performance of the advanced models when applied to next-generation-sensor data collected at various live sites, such as Camp Butner, NC and Camp Beale, CA as well as APG test sites. The technology was able to single out UXO ranging in caliber from 20 mm up to 155 mm. In addition, the ONVMS technique was seen to provide excellent classification in both single- and multiple-target scenarios when combined with advanced multi-axis/transmitter/receiver sensors data.

Acknowledgements

Introduction

Motivation
The detection and removal of buried unexploded ordnance (UXO) is an expensive and difficult task. In the United States, an estimated 11 million acres(44515 km^2, which is about 64 % of entire Georgia's territory) of land and one million acres (4046.9 km^2) of underwater lands may be contaminated with UXO [1-7]. Some of these lands are military practice ranges, to be turned over to the public for recreation or economical Exploitation; others are the sites of long passed conflicts. UXO may remain dangerous over many years. Cuban television reported the detonation of a projectile in Santiago Harbor, some 100 years after it was fired during the Spanish American War. Cuban sources noted that it was the seventh such piece of ordnance from the war to explode in Cuba over the past thirty years. On a vastly larger scale, since 1946 the French Department du Dominate has collected and destroyed more than 18 million artillery shells and 600,000 bombs dropped from airplanes. However, near the city of Verdun, alone, it is estimated that there are about 12 million unexploded shells still remaining from World War 1, many in degraded condition and containing toxic materials. Elsewhere in France are sites where hundreds of thousands or even millions of missiles rained down upon the landscape during that conflict, sometimes only within a matter of hours or days.

During the First World War overall about 15% of bombs failed to detonate. Thus, even after all the intervening time, the remains of this and other conflicts pose an enormous problem in the present. Including military training areas and regions where peaceful uses of ordnance were attempted, the problem of buried UXO is terribly widespread, from the jungles of Vietnam and the warm beaches of Puerto Rico and Hawaii, to the glaciers of British Columbia and the Aleutian Islands in Alaska.

The problem is more acute in European countries, where millions of buried UXOs remain from two world wars, as well as in south East Asian countries. For an example, by an estimate about 270 million bombs were dropped in Laos between 1964 and 1973. Out of this 80 million bombs failed to explore and still remains dangerous for public.

The UXO continues to pose problem at active and former Soviet Union military bases. Such as in Saloglu village, Agstafa district of Azerbaijan soviet army had the largest warehouses in the South-Caucasus region, consisting of 138 bunkers. In 1991, when Azerbaijan regained independence, the warehouse was destroyed by the soviet army before departing. As the result of the explosion thousands pieces of UXO were scattered over a large area of 4,400 hectares continuously posing a serious humanitarian, socio-economic and environmental threat to the local population. Since the explosion, 152 UXO-related accidents with 32 people killed were reported.

The problems have been worsening due to recent wars and ethnic conflict in worldwide, including my country of Georgia. During recent Russia-Georgia war in 2008, cluster bombs were dropped in Georgia. A cluster bomb consists of a few dozens of smaller sublimations that are dispersed before detonation, to ensure coverage of the widest area

possible. Part of the bumblers detonate at the cluster bomb's initial use. The rest of them remain on the surface as landmines. Children are consequently the most common victims of these landmines. Munitions of the sort were used in Iraq, Kosovo, Afghanistan, Lebanon, Vietnam and other places.

Mostly UXO are metallic or containing substantial metallic parts, which makes them easily detectable with current metal detectors. However, metal detectors detect not only UXO-s, they also detect all metallic targets as well. Recent studies have showed that, the over whelming task of finding and removing these UXOs is hampered by the fact that approximately 95 % of the costs are spent for digging non-UXO targets. Hence, accurate Discrimination techniques are needed. Over last two decades, low frequency electromagnetic induction sensing technology has merged as ultimate tool for subsurface UXO targets detection and discrimination.

Overall, UXO cleanup process consists three main parts: 1) Subsurface targets detection using geophysical sensors; 2) The data processing and targets parameters extraction by solving inverse electromagnetic induction problems; 3) Targets classification as UXO and non-UXO targets using the extracted targets parameters. This thesis describes all upon mentioned three parts for UXO classification. Namely, the work combines advanced physically complete forward and inverse methods, which provide effective and accurate UXO classification from current state of the art geophysical tensors data.

Objective and main results

The main objective of this work was to develop physically complete forward and inverse models in combination with state-of-the-art signal processing methodologies for robust UXO discrimination at live UXO sites using advanced electromagnetic induction (EMI) sensors data sets.

To achieve this objective, in this thesis:

We developed/extended physically complete forward approaches:

- Hybrid MAS/TSA algorithm [1] for understanding underline physics of EMI phenomenon.
- Normalized surface magnetic source model (NSMS) [2] for EMI sensors data inversion and classification.
- Orthonormalized volume magnetic source model (ONVMS) [3] for next generation EMI systems data analysis and subsurface multiple targets classification.

These models were combined with advanced signal processing and data-inversion approaches, which provided robust regularization and classification feature parameters estimations for targets intrinsic, such as magnetic polarizabilities, multi-static data matrix eigenvalues, and extrinsic, i.e. targets locations and orientations. These advanced signal processing algorithms are:

- Joint diagonalization for multi-target data pre-processing (JD) [4]
- Differential evolution (DE) [2, 5] for estimating targets locations and orientations.
- A field-potential (HAP) method to locate targets [6].

Our advanced forward-inverse and signal processing algorithms have been applied to next generation sensors data sets collected at several live UXO sites.

➢ We developed site specific UXO libraries for each live UXO sites. These libraries were used for targets classification via a finger-print matching technique.

➢ Our models were adapted to all next-generation sensors, including the MetalMapper, TEMTADS, MPV, and BUD, data sets. The models were applied to blind live-site UXO discriminations studies [7]. The studies have demonstrated the excellent discrimination capabilities.

The theses structure

Theses consist three main parts: first part provides a road map for implementing forward and inverse electromagnetic induction numerical methods for UXO detection and classification from basic physics to live UXO discrimination studies. In a real field the electromagnetic signals become convoluted with noise due to the instrument, magnetic soil and widespread background clutter. To understand and account for different noise source, the thesis provides mathematical fundamentals, physical meanings and practical realizations of forward and inverse signal processing approaches for unexploded

Specifically,

First the thesis outlines the combined Method of Auxiliary Sources (MAS) and thin skin approximation (TSA), which is an advanced, physically complete forward EMI model, for solving low frequency electromagnetic induction problems involving metallic objects placed in heterogeneous magnetic and conducting soils. Then, the normalized surface magnetic source (charge/dipole) model (NSMS), and ortho-normalized volume magnetic source (ONVMS) technique are presented for accurately representing the EMI responses of subsurface metallic targets. Third, we formulate and develop an inversion framework featuring robust regularization and parameter-determination methodologies (for both linear intrinsic signatures and non-linear extrinsic particulars) based on advanced signal processing algorithms. Namely, the models were combined with EMI data inversion approaches, such as the gradient search, direct search-differential evolution and etc., for extracting targets intrinsic (effective dipole polarizabilities) and extrinsic (locations and orientations) from advanced EMI sensor data; Fourth, We combine EMI models and classification methodologies to process complex, heterogeneous geophysical data, and finally we demonstrate the discrimination capability of the combined approach by applying it to blind live-site UXO discrimination studies.

Overview of Chapter 1

The chapter 1 outlines the theoretical basis of the detailed 3d EMI solvers, and advanced fast EMI forward models that we use to study low frequency EMI scattering phenomena and to represent the EMI response of obscured targets, respectively. We first present the Method of Auxiliary Sources (MAS) and thin skin approximation (TSA) for solving EMI problems in great details. Then we show the single-dipole model, which is usually insufficient in itself for representing targets EMI signals accurately. After that we introduce and study in detail the NSMS model, which distributes dipoles on a closed surface surrounding a target of interest. And then we derive and describe the ONVMS technique, which infuses dipoles throughout the subsurface volume illuminated by a sensor. We end by describing a data-preprocessing technique based on joint diagonalization that estimates the number of targets in a measurement with no need for data inversion; the method, moreover, can provide initial estimates of target locations and perform rudimentary discrimination.

The Method of Auxiliary Sources (MAS) for solution of the full electromagnetic (EMI) problem for penetrable, highly conducting and permeable metallic targets. The MAS is a numerical technique, originally designed for solving various electromagnetic radiations and scattering problems. It has been demonstrated that the MAS is a robust, easy to implement, accurate and sufficient method for studying a wide range of electromagnetic problems, such as investigation of waveguide structures, antennas, scattering, electromagnetic wave propagation in complex media, etc. Later MAS successfully was combined with small penetration approximation (SPA) and thin skin approximations (TSA) for analysis of low frequency EMI scattering phenomena. In standard MAS for EMI, boundary value problems are solved numerically by representing the electromagnetic fields in each domain of the structure under investigation by a finite linear combination of analytical solutions of the relevant field equations, corresponding to sources situated at some distance away from the boundaries of each domain.

EMI scattering responses are usually expressed in terms of the induction number. It is well established that the electromagnetic field inside a conductor decays over distances of the order of the skin depth. This reduces the efficiency and accuracy of the MAS at high induction numbers due to singularities that appear in the scattering matrix. To overcome this problem, a combined MAS-thin skin approximation (MAS-TSA) has developed. The TSA is based on the divergence-free Maxwell's equation for the magnetic field and it approximates magnetic fields normal derivatives with magnetic field on the targets surface. The model has been used to solve a variety of EMI problems from the magnetostatic regime up to 1 MHz for land-based UXO detection and discrimination.

In general UXO discrimination is a non-linear inverse problem, which requires high fidelity forward models. The most frequently used method for representing the EMI response of a metallic target in both frequency and time domains approximates the whole object with a set of orthogonal co-located point dipoles that fire up in response to the primary field; the induced dipole moment is related to the primary field through a symmetric polarizability tensor. The use of this dipole approximation is motivated by its

speed and simplicity; this simplicity, however, rests on assumptions that often become problematic and limit the model's usefulness. One such assumption is that the buried target of interest is either far enough from the transmitter loop, or small enough, that the primary field is essentially uniform throughout its extent. Usually, complex targets composed of different materials and different sections that contribute appreciably to the response—and, in the case of UXO, containing such complicating features as fins and rings—simply cannot be modeled accurately with a single point dipole. Such cases require more advanced methods that will capture the underlying physics correctly. One such technique is the NSMS model.

The NSMS method can be considered as a generalized surface dipole model, and indeed reduces to the point dipole model in a special limiting case. The NSMS approach models an object's response to the primary field of a sensor by distributing a set of equivalent elementary magnetic sources—normally oriented dipoles in this case—over an auxiliary surface that surrounds it. Such a surface distribution can be hypothetically generated by spreading positive magnetic charge over the outer side of the equivalent surface (usually a prolate spheroid) and an identical distribution of opposite sign on its inner side, resulting in a double layer of magnetic charge separated by an infinitesimal distance. This double layer introduces the proper discontinuities in the tangential components of the magnetic flux density vector but does not affect the transition of its normal component, which must always be continuous given the lack of free magnetic charges in nature. The resulting magnetic-moment distribution radiates a field that by construction satisfies the governing EMI equations and can thus account for the secondary field outside the object. The particulars of location and orientation are divided out by normalizing the dipole density at every point with the component of the primary magnetic field normal to the surface. The resulting surface amplitude of the NSMS distribution is a property of the object, and its integral over the surface constitutes a sort of global magnetic polarizability that is independent of the computational constructs—primary field, surrounding surface, object location and orientation, etc.—introduced for its determination. The surface amplitude can be determined directly for library-matching purposes by minimizing the difference between measured and modeled data for a known combination of object and sensor at a given relative location and orientation.

The NSMS technique has demonstrated good computational speed and superior classification performance when applied to EMI datasets consisting of well-isolated single targets, but is found to degrade quickly on both counts when confronted with multi-target cases. This has forced us to generalize the model further and develop the ONVMS procedure. The ONVMS model, a further extension of NSMS, is based on the assumption that a collection of subsurface objects can be replaced with a set of magnetic dipole sources, distributed over a volume. Since all actual radiating sources are located within the scatterers—rather than in the soil or air—the spatial distribution of these fictitious dipoles (their amplitudes scaled by the primary field) indicates the locations and orientations of any targets present inside the computational volume. The great advantage of the ONVMS technique over the other models discussed above is that it takes into account mutual couplings between different sections of the different targets while simultaneously avoiding the appearance of singular matrices in multi-target situations. It

is thus gracefully indifferent to the number of targets: Once the amplitudes and the locations of the corresponding dipoles are determined, one need only look at their clustering patterns, compute the time-dependent total polarizability tensor for each group, and subsequently diagonalize each such tensor using joint diagonalization. The resulting diagonal elements have been found to be intrinsic to the objects they represent, and can be used, on their own or combined with other quantities, in discrimination analysis. Recent ESTCP live-site discrimination studies have clearly indicated the superior discrimination performance of the ONVMS method in combination with the statistical processing approaches described below.

One of the main challenges one faces when attempting multi-target inversion and classification is the inability to estimate the number of targets. In order to overcome this problem, we implemented a technique based on joint diagonalization that estimates the number of targets present in the field of view of the sensor as it takes a data shot, in real time and without requiring a forward model, and, in a good number of cases, even provides the capability to perform a quick inversion-free characterization and classification of these targets. JD determines the eigenvalues and eigenvectors of a square time- or frequency-dependent multi-static response (MSR) matrix synthesized directly from measured data. The number of nonzero eigenvalues of the matrix (i.e., those above a noise threshold) is related to the number of elementary sources in the illuminated cell; moreover, the time-decay patterns of these non-vanishing eigenvalues are intrinsic properties of the targets to which the sources correspond and can ultimately provide dependable classification features.

Overview of Chapter 2

Chapter 2 discusses inverse models: the methods used to harness the forward models so they provide relevant intrinsic and extrinsic information starting from measured data. After presenting some traditional gradient-search based methods and pointing out some of their limitations we describe differential evolution (DE), a state-of-the-art global-search method, similar in character to genetic algorithms, that has shown remarkable flexibility and usefulness. We end by describing the HAP method, a semi-analytic non-iterative procedure to locate buried targets.

Determining a buried object's orientation and location is a non-linear problem. Inverse-scattering problems are solved by determining an objective function, as a goodness-of-fit measure between modeled and measured magnetic field data. Standard gradient search approaches often suffer from a surfeit of local minima that sometimes result in incorrect estimates for location and orientation. To avoid this problem we recently developed a different class of global optimization search algorithms. One such technique is the Differential Evolution (DE) method, a heuristic, parallel, direct-search method for minimizing non-linear functions of continuous variables that is very easy to implement and has good convergence properties. We combined DE with ONVMS to invert digital geophysical EMI data. All EMI optimizations were split into linear and nonlinear parts, iterating between them to minimize the objective function. Once the target locations are

found, the amplitudes of responding ONVMS are determined and used to classify the object relative to items of interest.

In the EMI regime, the secondary magnetic fields measured by the EMI receivers are induced by eddy currents magnetic dipoles which are distributed non-uniformly inside the scatterer. There are some particular points, named "scattered field singularities" (SFS), where most of these sources are concentrated. Recent studies show that under certain conditions the entire scatterer can be replaced with several responding elementary sources by putting them at SFS points. We have found a new analytic expression for estimating the location, orientation, and polarizability elements of a buried object starting from measured EMI data without solving traditional ill-posed inverse-scattering problems. The algorithm (dubbed "HAP") is based on the fact that a target's response can be approximated by dipole sources concentrated at SFS points. It utilizes three global values at a single location in space: (1) the magnetic field vector $\mathbf{H}$, (2) the vector potential $\mathbf{A}$, and (3) the scalar magnetic potential ψ. Since among these quantities only the $\mathbf{H}$ field (and sometimes only one of its components) is measurable, we employ a variation of the NSMS model to obtain $\mathbf{A}$ and ψ we distribute elementary sources on an auxiliary planar layer, located between the sensor and the object, and find their amplitudes by fitting measured data.

Overview of Chapter 3

Chapter 3 presents and describes the next-generation EMI sensors—the METALMEPPER, the TEMTADS array, the MPV portable instrument, and the BUD system—that took all the data we use and that represent the state of the UXO remediation hardware. We present the results of several testing and validation studies carried out on laboratory, test stand and US army standardized Aberdeen Proving Ground in Maryland test-site data from these devices. Also Provides a detailed account of the discrimination and classification studies performed on data from actual UXO sites—the Camp Sibert in Alabama, Camp San Luis Obispo in California, and Camp Butner in North Carolina—in which several combinations of the techniques presented in the previous chapters were used. We describe our solution strategies and the results we obtained.

References
8. F. Shubitidze, K. O'Neill, K. Sun, I. Shamatava, and K.D. Paulsen, "A hybrid full MAS and combined MAS-TSA algorithm for broadband electromagnetic induction problem", *Applied computational electromagnetic society Journal*, pages: 112-126, March, 2004.
9. F. Shubitidze, K. O'Neill, B.E. Barrowes, I. Shamatava, J.P. Fernández, K. Sun and K.D. Paulsen, "Application of the normalized surface magnetic charge model to UXO discrimination in cases with overlapping signals", *Journal of Applied Geophysics Vol 61 Issues 3-4, 2007* Pages 292-303.
10. F. Shubitidze, J. P. Fernández, B. E. Barrowes, I. Shamatava, A. Bijamov, K. O'Neill, D. Karkashadze, "The Orthonormalized Volume Magnetic Source Model for Discrimination of Unexploded Ordnance," *IEEE Transactions on Geoscience and Remote Sensing,* vol 8, pp 5218-5229.

11. F. Shubitidze, J. P. Fernández, I. Shamatava, B. E. Barrowes, and K. O'Neill, "Joint diagonalization applied to the detection and discrimination of unexploded ordnance," *Geophysics*, vol. 77, no. 4, pp. WB149–WB160, 2012.

12. F. Shubitidze, K. O'Neill, I. Shamatava , K. Sun , and K. D. Paulsen. 2005, "Combined differential evolution and surface magnetic charge model algorithm for discrimination of UXO from non-UXO items: Simple and general inversions", Proceeding SPIE, Defense and Security, Orlando, Fl, 2005, 12 pages.

13. F. Shubitidze, D. Karkashadze, B. E. Barrowes, I. Shamatava, and K. A. O'Neill, "A New Physics-based Approach for Estimating a Buried Object's Location, Orientation and Magnetic Polarization from EMI Data," *Journal of Environmental and Engineering Geophysics,* vol. 13, pp. 115-130, Sep 2008.

14. A. Bijamov, F. Shubitidze, J. P. Fernández, B. E. Barrowes, I. Shamatava,and K. O'Neill, "Camp Butner live-site UXO classification using hierarchical clustering and Gaussian mixture modeling," *IEEE Trans. Geosci.Remote Sens.*, vol. 52, no. 8, pp. 5218–5229, Aug. 2014

Chapter 1. Forward models

1.1 Introduction

Cleaning up buried UXO has been identified as very high priority environmental and military problem for many years. In many cases upon UXO impact into ground the ordinances are broken in parts without explosions and are remaining very dangerous for long time. Further, in many highly contaminated sites, multiple UXO together with widespread clutter appear simultaneously within the field of view of the sensor and it is extremely difficult to distinguish them reliably from typically widespread pieces of metal clutter. Thus a current research goal is to isolate ways to discriminate objects of concern from surrounding metallic clutter, once an item has been detected. Broadband (20 Hz ~ 100 kHz) electromagnetic induction (EMI) sensors are promising tool for the detection and discrimination of buried unexploded ordinance (UXO) [1-75]. The discrimination, which in general is an inverse problem, requires very fast and accurate representation of EMI response. This has driven the development of new analyses and analytical tools for studying EMI scattering problems. The only well-established analytical solutions to date for broadband EMI scattering are for the case of the sphere in both frequency and time domain [76, 77] and cylinder of infinite length oriented transverse to the primary field [78]. Recently progress has been reported for analytical solution of EMI scattering from spheroids [18, 27, 36], including specialization to treat high frequency conditions, when penetration of the object is slight [27, 36] (SPA, the small penetration approximation). Some evaluation problems for the spheroidal shapes remain, in the mid-region of the EMI band. Particularly for arbitrary 3-D geometries, one must usually resort to numerical models to obtain results most relevant to the variety of target types that must be considered. Targets of arbitrary shape have been attacked using the Method of Moments (MoM) with an impedance boundary condition (IBC) [79]. More recently, bodies of revolution (BOR) have been modeled using the MoM with full, rigorous boundary conditions, requiring substantial computation times [15]. FEM –BEM approaches [28, 29] not reliant on the IBC were developed. In parallel with the above-mentioned analytical work on spheroid solutions, a compact numerical formulation has been produced for arbitrary shapes using the Thin Skin Approximation (TSA) [24], which only applies the divergence equation for magnetic field inside the target. This performs very well for the difficult realm of high frequency conditions, and for high permeability cases has remarkably broadband applicability.

Finally, the electromagnetic sensing group at Thayer School of Engineering, Dartmouth College has developed the Method of Auxiliary Sources (MAS [25]) for solution of the full EMI problem for penetrable, highly conducting and permeable metallic targets. The MAS is a numerical technique, originally designed for solving various electromagnetic radiation and scattering problems [80-88]. It has been demonstrated that the MAS is a robust, easy to implement, accurate and sufficient method for studying a wide range of electromagnetic problems, such as investigation of waveguide structures, antennas, scattering, electromagnetic wave propagation in complex media, etc. Later MAS

successfully was combined with SPA [36] and TSA [24] for analysis of low frequency EMI scattering phenomena. In standard MAS for EMI [25], boundary value problems are solved numerically by representing the electromagnetic fields in each domain of the structure under investigation by a finite linear combination of analytical solutions of the relevant field equations, corresponding to sources situated at some distance away from the boundaries of each domain.

EMI scattering responses are often expressed relative to the induction number $\chi \equiv \sqrt{-2j\pi\nu\sigma\mu}\,a$, where j is the square root of minus one a (m) is a characteristic dimension of the object (usually the smallest one), ν = frequency (Hz), $\mu = \mu_o\mu_r$ - magnetic permeability and σ (S/m) is the scatterer's electrical conductivity. The quantity χ is proportional to a/δ, where δ is the skin depth. The main limitation of MAS is its reduced accuracy and efficiency when dealing with the high frequency EMI induction problem [25]. The reason is that at high induction numbers the electromagnetic fields inside metallic objects produced by auxiliary magnetic dipoles placed on the external auxiliary surface(s) decay over distances on the order of δ. Under a level of numerical resolution fine enough to represent the object shape accurately, but no finer than that, matrix elements become almost zero (within the accuracy of the computer. The matrix becomes ill-conditioned and the solution unstable. To avoid this kind of difficulty recently several types of approximations were developed, such as the Thin Skin (TS) and small penetration (SP) approximations, which are related to impedance boundary conditions. The accuracy and validity of the TSA in conjunction with the BEM have been studied previously [24], in application to highly conducting and permeable (e.g. steel) metallic objects with regular geometries, such as the sphere, ellipsoid, prolate and oblate spheroid, subject to a uniform primary magnetic field. Under these constraints, it has been shown that for a wide class of EMI scattering problems, the TSA is very accurate and efficient over entire broadband EMI frequency range [24]. It is easy to implement for an arbitrary geometry. At the same time, the BEM-TSA cannot treat low induction number cases reliably, particularly for non-permeable materials. Recently, a hybrid MAS-SPA algorithm was developed in [55]. It has been shown that MAS-SPA is very efficient for analyzing EMI responses at high induction numbers for spheroidal objects. The algorithm is using a factor f [55], which can readily be obtained only for the canonical objects. However, it is very difficult to extend this algorithm for an arbitrary object. The combined MAS/TSA algorithm was introduced and tested for highly permeable and conducting regular shapes under highly variable primary (transmitted) field's as well non-regular geometries [74]. In this chapter a hybrid algorithm applying the standard MAS at low frequency and the combined MAS/TSA at high frequency is proposed. The ultimate goal is to use the full MAS formulation at low induction numbers, and to employ the MAS/TSA formulation at high frequency to connect electromagnetic fields inside and outside of the scatterer. In the combined MAS/TSA algorithm, the number of unknowns is reduced by a factor of 3, in an arbitrary *3-D* EMI problem, relative to the original full MAS. Single frequency computations are approximately four times faster. For multi-frequency cases, the matrices expressing magnetic fields produced by auxiliary magnetic charges do not depend on frequency and can be stored for use, without recalculation, over an extended band.

UXO discrimination is an inverse problem that demands a fast and accurate representation of a target's EMI response. Much of my research in this thesis has had to do with the development, implementation, and testing of models that provide such representations in a physically complete, noise-tolerant way that allows them to perform adequately in realistic settings and to set the stage for dependable live-site UXO discrimination. Electromagnetic induction (EMI) sensing, in both frequency and time domains, is emerging as one of the most promising remote sensing technologies for detection and discrimination of buried metallic objects, particularly unexploded ordinance (UXO). UXO sites are highly contaminated with metallic clutter so that the major problem is discrimination not detection. In order to overcome this problem, first underline physics of EMI field scattering phenomena needs to be studied using numerical methods. One of such computational fast and effective methods is the Method of auxiliary sources.

In the MAS, boundary value problems are solved numerically by representing the electromagnetic fields in each domain of the structure under investigation by a finite linear combination of analytical solutions of the relevant field equations, corresponding to sources situated at some distance away from the boundaries of each domain. The "auxiliary sources" producing these analytical solutions are chosen to be elementary dipoles/charges located on fictitious auxiliary surfaces that usually conform to the actual surface(s) of the structure. In practice, at least as the method is realized here, we only require points on the auxiliary and actual surfaces; thus we do not need to the detailed mesh structures required by other methods such FEM [28, 29], and method of moments [30].

The two auxiliary surfaces are set up inside and outside the scattering object. The fields outside of the structure are considered to originate from a set of auxiliary magnetic charges placed inside the object, while the fields inside the object are taken to arise from a set of auxiliary magnetic dipoles placed outside. The interior and exterior fields thus constructed are required to obey Maxwell's boundary conditions—the continuity of the tangential magnetic field components and the jump condition for the normal magnetic field components—as evaluated at arrays of selected points on the physical surface(s) of the structure. This results in a matrix equation in which the amplitudes of the auxiliary sources are the unknowns to be determined. Once these amplitudes are found the solution is complete: the electromagnetic field—as well as any quantity related to it—can easily be computed throughout the computational space.

In general UXO discrimination is a non-linear inverse problem, which requires high fidelity forward models [31-33]. The most frequently used method for representing the EMI response of a metallic target in both frequency and time domains approximates the whole object with a set of orthogonal co-located point dipoles that fire up in response to the primary field; the induced dipole moment is related to the primary field through a symmetric polarizability tensor. The use of this dipole approximation is motivated by its speed and simplicity; this simplicity, however, rests on assumptions that often become problematic and limit the model's usefulness. One such assumption is that the buried target of interest is either far enough from the transmitter loop, or small enough, that the

primary field is essentially uniform throughout its extent. Usually, complex targets composed of different materials and different sections that contribute appreciably to the response—and, in the case of UXO, containing such complicating features as fins and rings—simply cannot be modeled accurately with a single point dipole. Such cases require more advanced methods that will capture the underlying physics correctly. One such technique is the NSMS model.

The NSMS method [2-5] can be considered as a generalized surface dipole model, and indeed reduces to the point dipole model in a special limiting case. The NSMS approach models an object's response to the primary field of a sensor by distributing a set of equivalent elementary magnetic sources—normally oriented dipoles in this case—over an auxiliary surface that surrounds it. Such a surface distribution can be hypothetically generated by spreading positive magnetic charge over the outer side of the equivalent surface (usually a prolate spheroid) and an identical distribution of opposite sign on its inner side [3], resulting in a double layer of magnetic charge separated by an infinitesimal distance. This double layer introduces the proper discontinuities in the tangential components of the magnetic flux density vector **B** but does not affect the transition of its normal component, which must always be continuous given the lack of free magnetic charges in nature. The resulting magnetic-moment distribution radiates a field that by construction satisfies the governing EMI equations and can thus account for the secondary field outside the object. The particulars of location and orientation are divided out by normalizing the dipole density at every point with the component of the primary magnetic field normal to the surface. The resulting surface amplitude Ω of the NSMS distribution is a property of the object, and its integral Q over the surface constitutes a sort of global magnetic polarizability that is independent of the computational constructs—primary field, surrounding surface, object location and orientation, etc.—introduced for its determination. The surface amplitude can be determined directly for library-matching purposes by minimizing the difference between measured and modeled data for a known combination of object and sensor at a given relative location and orientation.

The NSMS technique has demonstrated good computational speed and superior classification performance when applied to EMI datasets consisting of well-isolated single targets, but is found to degrade quickly on both counts when confronted with multi-target cases. This has forced us to generalize the model further and develop the ONVMS procedure.

The ONVMS model [3], a further extension of NSMS, is based on the assumption that a collection of subsurface objects can be replaced with a set of magnetic dipole sources, distributed over a volume. Since all actual radiating sources are located within the scatterers—rather than in the soil or air—the spatial distribution of these fictitious dipoles (their amplitudes scaled by the primary field) indicates the locations and orientations of any targets present inside the computational volume. The great advantage of the ONVMS technique over the other models discussed above is that it takes into account mutual couplings between different sections of the different targets while simultaneously avoiding the appearance of singular matrices in multi-target situations. It is thus

gracefully indifferent to the number of targets: Once the amplitudes and the locations of the corresponding dipoles are determined, one need only look at their clustering patterns, compute the time-dependent total polarizability tensor for each group, and subsequently diagonalize each such tensor using joint diagonalization. The resulting diagonal elements have been found to be intrinsic to the objects they represent, and can be used, on their own or combined with other quantities, in discrimination analysis. Recent ESTCP live-site discrimination studies have clearly indicated the superior discrimination performance (illustrated in chapter 5) of the ONVMS method in combination with the statistical processing approaches described in Chapter 2.

One of the main challenges one faces when attempting multi-target inversion and classification is the inability to estimate the number of targets. In order to overcome this problem, we implemented a technique based on joint diagonalization [35] that estimates the number of targets present in the field of view of the sensor as it takes a data shot, in real time and without requiring a forward model, and, in a good number of cases, even provides the capability to perform a quick inversion-free characterization and classification of these targets. JD determines the eigenvalues and eigenvectors of a square time- or frequency-dependent multi-static response (MSR) matrix synthesized directly from measured data. The number of nonzero eigenvalues of the matrix (i.e., those above a noise threshold) is related to the number of elementary sources in the illuminated cell; moreover, the time-decay patterns of these non-vanishing eigenvalues are intrinsic properties of the targets to which the sources correspond and can ultimately provide dependable classification features.

1.2   Magneto-quasistatic assumption

All solutions in this chapter are based in part on two reasonable assumptions. The first is that, throughout the entire UWB EMI frequency band, electromagnetic phenomena are magneto-quasistatic. While this may be taken as something of a foregone conclusion in low frequency EMI, we examine the assumption explicitly here because recent developments have raised the upper frequency limits for EMI practice to about 300 kHz. This makes the magneto-quasistatic assumption more suspects.

Consider a highly conducting and permeable metallic scattering object, with relative permeability μ_r and conductivity σ [S/m] is embedded in a uniform background. The time dependence expression of $e^{j\omega t}$ is suppressed subsequently. In the EMI problem considered here, the frequency range is from 0 Hz up to 300 kHz. The governing equations that form the basis for any pertinent analysis of EMI scattering physics are Maxwell's equations. In both static and transient fields, Maxwell's magnetic field divergence equation must be satisfied.

$$\nabla \cdot \mathbf{H} = 0 \tag{1}$$

Where this form of the equation assumes spatially uniform μ. In practice here we will assume that μ may vary between different portions of an object of interest, but that it is

constant within any given section or sub-region. Thus (1) applies within every (sub) region, except on boundaries, where we apply a boundary condition instead.

The particular equations in Maxwell's complete set that pertain most directly to induction are Faraday's and Ampere's Laws,

$$\nabla \times \mathbf{E} = -j\mu\omega\mathbf{H} \tag{2}$$

$$\nabla \times \mathbf{H} = \sigma\mathbf{E} + j\varepsilon\omega\mathbf{E} \tag{3}$$

where $\mathbf{E}$ is the electric filed (V/m) and $\mathbf{H}$ is magnetic field (A/m). The quantity $j\omega\varepsilon\mathbf{E} = \dfrac{\partial \mathbf{D}}{\partial t}$ is called the displacement current, where ε is the permittivity of the medium (farad/m). Note that, even in the frequency domain, ε as used here does *not* include any portion resulting from the electrical conductivity of the medium, σ, the effects of which will always be expressed separately. The term $\sigma\mathbf{E}$ represents actual electric currents in the medium. We wish to examine the magnitudes of these terms, relative to each other and also relative to the various derivatives on the left side of the equation. We will do this by tracing the influence of each of the terms on the right hand side within an equation entirely in $\mathbf{H}$, obtained by combining (3) with other of Maxwell's equations. Taking the curl of (3) and performing manipulations yields

$$\nabla^2\mathbf{H} \;=\; j\omega\sigma\mu\mathbf{H} - \omega^2\varepsilon\mu\mathbf{H} \tag{4}$$

The first and second terms on the right in (4) descend from the first and second terms on the right in (3), respectively. Specifically, the relative magnitude of the first (second) term on the right hand side of (3) corresponds to the relative magnitude of the first (second) term on the right hand side of,(4) and we will analyze the latter. The three parameter regions where this equation will be examined are those for air (free space), the soil, and the metallic scatterers.

The situation is different in each of the three parameter regions. In the air we assume that σ is approximately zero, so that the second term in (4) drops out. This leaves a classical wave equation with wavenumber k defined as

$$k \;=\; \frac{2\pi}{\lambda} \;=\; \omega\sqrt{\varepsilon\mu} \tag{5}$$

Where λ is the wavelength. Higher frequencies produce shorter wavelengths. At the top of the MF-EMI band (300 kHz), this expression indicates that the electromagnetic wavelength is one kilometer. Typical distances over which we are concerned about electromagnetic interactions are on the order of 1 m. Thus there is negligible phase difference between different points within the domain of consideration in the air. Fields change essentially in unison throughout, with the structure of static fields, gaining time dependence only through the action of sources and boundary conditions. This results in the uniform time factor $e^{j\omega t}$, and a quasi-static phenomenology. The The ultimate

significance of this in connection with the equations above is that *both* terms on the right hand side of (4) are negligible, as both are FD expressions for time derivatives. Thus the corresponding terms in (3) are also negligible, and the H field is irrational ($\nabla \times \mathbf{H} = 0$). An irrotational field may be represented as the gradient of a scalar potential, ψ (A/m^2).

$$\mathbf{H} = -\nabla \psi \tag{6}$$

Substituting (6) in (1) produces the governing equation for the air region.

$$\nabla^2 \psi = 0 \tag{7}$$

Representing of the magnetic field by the scalar potential ψ, instead of a vector potential, has two main advantages: first the calculation of Greens function related to the Laplace equation (7) is very simple and fast, and second the scattered magnetic field can be represented as summation of the fields produced by a set of magnetic charges. This reduces number of unknowns at least a factor of 2 relative to the vector potential representation. Within the soil, σ is nonzero and the ratio of the magnitude of the third to the second term in (4) is $\omega\varepsilon/\sigma$. As a "worst" case, i.e. the one that most threatens the MQS assumption, we assume $\omega \sim 10^6$ rad/s, $\sigma \sim 10^{-2}$ S/m, and $\varepsilon \sim 10^{-10}$ F/m. This combination of parameters means that we would be operating at the extreme upper limit of the MF-EMI band and presupposes a particularly unlucky set of soil properties, with low conductivity but rather high dielectric constant. Even this combination of parameters implies that the third (displacement current) term is not larger than the second (electric current) term. To estimate the significance of the electric currents in the soil, compare their magnitude to those induced in the metallic target. By general continuity conditions, the electric field E will be on the same order in the soil immediately surrounding the target and in the parts of the metal where the most significant currents are flowing. As the currents are equal to σE, the ratio of currents in metal and soil will be approximately equal to the ratio of their conductivities. A reasonable upper bound on soil conductivity is $\sigma \sim 10^{-2}$ S/m. A typical metal of interest has $\sigma \sim 10^7$ S/m. Thus the currents in the metal are about nine orders of magnitude stronger than those in the soil. Unless the metal scatterer is extremely small and simultaneously the sensor samples an enormously larger volume of soil (not the case here), the fields in the soil will be dominated by those produced by currents in the metal. That is, the electric currents in the soil will not be a significant factor in determining the fields in the soil. Thus we conclude that the term containing the soil currents may be dropped (first term on the right in(4)). We have already concluded that the second term is not more significant than the first; therefore the entire right hand side of (4) is again negligible. Thus, in the soil as in the air, we conclude that the magnetic fields are irrotational and can be represented using a scalar potential, i.e with the governing equation(7).

Within the metal, we again examine the quantity $\omega\varepsilon/\sigma$. Using the typical values cited above we immediately conclude that the displacement current term is negligible compared to the electric current term. However, the electric currents within the metal are by no means negligible; rather, they are a fundamental source of the scattered signals. Thus two terms remain in(4), which may be construed as a Helmholtz equation

$$\nabla^2\mathbf{H} + k^2\mathbf{H} = 0, \ \ k=\sqrt{-j\omega\sigma\mu} \tag{8}$$

where k is sometimes referred to as a wavenumber, by analogy with higher frequency solutions to the equation. However note that (8) is *not* a wave equation, as the second term $-j\omega\sigma\mu\mathbf{H}$ is the frequency domain equivalent of $\sigma\mu$ times the *first* derivative $\mathbf{H}$ with respect to time, not the second derivative. We can create "traveling wiggles" within the metal by imposing sinusoidal behavior on its surface. However these are not true waves, e.g. they do not reflect. As in the wave case, fundamental solutions of (8) can be expressed as

$$\mathbf{H} \propto \frac{e^{jkR}}{\mu_r R}; k = \gamma + i\gamma \ ; \ \gamma = \frac{\sqrt{\omega\sigma\mu}}{\sqrt{2}}, \ \mathbf{R} = \mathbf{r}-\mathbf{r}' \tag{9}$$

Because the real and imaginary parts of k are equal, the spatially oscillating factor e^{jkR} decays by $1/e$ in less than one sixth of its spatial period.

1.3 The method of auxiliary sources

In the EMI frequency regime the EM field penetrate inside the object. Internal and external fields at the surface of the object must satisfy the continuity of tangential components of $\mathbf{H}$ and normal component of $\mathbf{B}$

$$\hat{\mathbf{n}}\times(\mathbf{H}_1^{sc} + \mathbf{H}^{pr}) = \hat{\mathbf{n}}\times\mathbf{H}_2 \tag{10}$$

$$\hat{\mathbf{n}}\cdot(\mathbf{H}_1^{sc} + \mathbf{H}^{pr}) = \hat{\mathbf{n}}\cdot\mu_r\mathbf{H}_2 \tag{11}$$

Here $\hat{\mathbf{n}}$ is a unit normal vector on the real surface [89,104] $\mathbf{H}^{pr}$ is the primary magnetic field, $\mathbf{H}_1^{sc}$ is the scattered magnetic field radiated by the auxiliary magnetic charges, which we consider to be distributed over the inner auxiliary surface [25]; $\mathbf{H}_2$ is the total magnetic field inside the object, produced by the auxiliary magnetic sources placed on the outer auxiliary surface. Using conventional MAS [25] the boundary conditions (10) and (11) can be written in the following compact matrix form:

$$\begin{bmatrix} G_n^Q & \mu_r G_n^{P_u} & \mu_r G_n^{P_v} \\ G_u^Q & G_u^{P_u} & G_u^{P_v} \\ G_v^Q & G_v^{P_u} & G_v^{P_v} \end{bmatrix}\begin{bmatrix} Q \\ P_u \\ P_v \end{bmatrix} = -\begin{bmatrix} H_n^{pr} \\ H_u^{pr} \\ H_v^{pr} \end{bmatrix} \tag{12}$$

where Q is a vector containing the amplitude of auxiliary magnetic charges, P_k, k=u,v is a vector containing the amplitude of auxiliary magnetic dipoles oriented along u and v, which are orthogonal directions on an auxiliary surface, G_ξ^Q is exterior field expressed with Green's function $1/(4\pi R)$ where $R=|\mathbf{r}\text{-}\mathbf{r}'|$ and $G_\xi^{P_\gamma}$ is the interior solution expressed ultimately in terms dipole sources distributed over an exterior auxiliary surface, together with a Green function of the form $e^{jkR}/4\pi R$. More explicit form of the

G_ξ^Q, and $G_\xi^{P\gamma}$ matrices, where $\hat{\xi}=\hat{n},\ \hat{u},\ \hat{v}; \gamma = u,v$, is presented in [25]. When the skin depth becomes small so that both real and imaginary parts of k become high, the $G_\xi^{P_k}$ matrix's elements become very small compared to G_ξ^Q matrix elements. At relatively high frequency (more that 10 kHz for common steel, copper, aluminum, brass etc), the $G_\xi^{P_k}$ matrix elements decay very rapidly in space and linear system (12) becomes unstable.

1.4   Combination of MAS with TSA

To avoid this problem it is desirable to establish an alternative formulation that would be applicable for high frequencies. It is well known that at high induction numbers the internal field is non-zero only in a thin layer close the surface (Fig 1). Under this condition, divergence free Maxwell's equation applies just below surface [24, 74]. That equation and the thinness of the surface

Layer can be exploited to provide a boundary condition on the external field, obviating the necessity for complete solution of the internal field. We will proceed in a manner analogous to that in [24, 74], where linear interpolation of unknowns is used over piecewise flat surface elements, in a Galerkin integral treatment of the governing relation. Here consider a general curvilinear surface, with completely continuous tangents and normals, and a subdomain integration of the governing equation. Gauss's Law (the magnetic field divergence equation) is integrated over a thin finite volume just below the object's surface, to produce the relation

$$\nabla \cdot \mathbf{H}_2 = 0 \quad \Box \quad \oiint_A \mathbf{H}_2 \cdot d\mathbf{A} = 0 \tag{13}$$

or

$$H_{2,n_2} \cdot A_{n_2} - H_{2,n_1} \cdot A_{n_1} + H_{2,u_2} \cdot A_{u_2} - H_{2,u_1} \cdot A_{u_1}$$
$$+ H_{2,v_2} \cdot A_{v_2} - H_{2,v_1} \cdot A_{v_1} = 0 \tag{14}$$

Where $A = A_{n_2} + A_{n_1} + A_{u_2} + A_{u_1} + A_{v_2} + A_{v_1}$ I s a total area of the thin volume Let us divide (14) equation by the layer thickness d and take limit as $d \to 0$, obtaining

$$A_n \frac{\partial H_{2,n}}{\partial n} + H_{2,n} \frac{\partial A_n}{\partial n} + H_{2,u_2} L_{u_2} - H_{2,u_1} L_{u_1}$$
$$+ H_{2,v_2} L_{v_2} - H_{2,v_1} L_{v_1} = 0 \tag{15}$$

Here $\partial n = \partial d$. The basic tenet of the TSA is that fields just below the surface within the thin layer vary approximately one-dimensionally, normal to the surface. Thus, as d -> 0 the normal component of the magnetic field $H_{2,n}$ and I t 's derivative $\dfrac{\partial H_{2,n}}{\partial n}$ along normal $\hat{n}$ are related to each other through:

$$\frac{\partial H_{2,n}}{\partial n} = jkH_{2,n}(0, u, v) \qquad (16)$$

Where $H_{2,n}(0, u, v)$ is the value as n->0 on the interior of the surface. Using boundary conditions (10) and (11) together with the TSA condition (16), equation (15) can be rewritten for external magnetic field on boundary in following form:
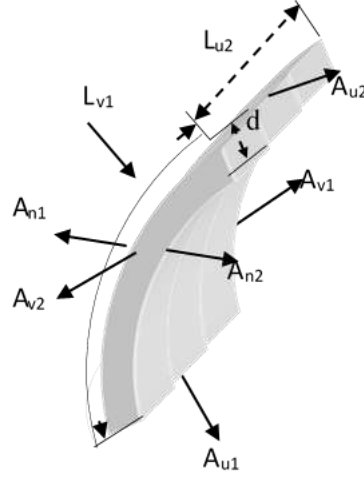
Figure 1.1: Geometry of volume just below the real surface A

$$\left[H_{1,n}^{sc} \frac{1}{\mu_r} \left(jkA_n + \frac{\partial A_n}{\partial n} \right) \right] +$$
$$\left[H_{1,u_2}^{sc} L_{u_2} - H_{1,u_1}^{sc} L_{u_1} + H_{1,v_2}^{sc} L_{v_2} - H_{1,v_1}^{sc} L_{v_1} \right] = -[Y] \qquad (17)$$

Or , in compact matrix form:

$$[Z][Q] = -[Y] \qquad (18)$$

Where

$$[Z] = \left[G_n^Q \frac{1}{\mu_r} \left(jkA_n + \frac{\partial A_n}{\partial n} \right) + G_{u_2}^Q L_{u_2} - G_{u_1}^Q L_{u_1} \right] +$$
$$\left[G_{v_2}^Q L_{v_2} - G_{v_1}^Q L_{v_1} \right] \qquad (19)$$

And

$$[Y] = \left[H_n^{pr} \frac{1}{\mu_r} \left(jkA_n + \frac{\partial A_n}{\partial n} \right) \right] +$$
$$\left[H_{u_2}^{pr} \cdot L_{u_2} - H_{u_1}^{pr} \cdot L_{u_1} + H_{v_2}^{pr} \cdot L_{v_2} - H_{v_1}^{pr} \cdot L_{v_1} \right] \qquad (20)$$

To apply MAS to the exterior region, a set of magnetic charges is placed mathematically inside the physical surface, on the auxiliary surface S_1^{aux} Figure 1.2. The secondary magnetic
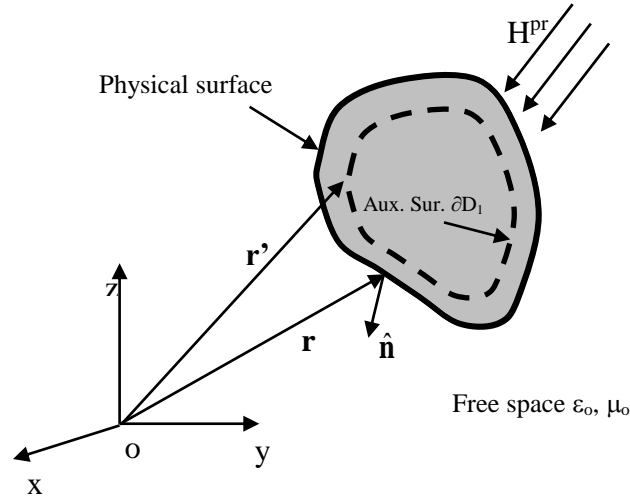
Figure 1.2: Combined MAS-TSA

field due to the target is expressed as a superposition of the fields generated from a finite number (N) of point charges, $\{Q_i\}$, $i = 1, 2, 3, ..., N$ placed on the surface S_1^{aux}. The total secondary magnetic field at the position $\vec{r}_n$ due to the auxiliary charges is expressed as Eq. 21 in [25]. By applying equation (17) at M collocation point on S and expressing $\vec{H}_1^{sc}$ using the $\{Q_i\}$, we cast into an NxM linear system of equations, where normally we set M = N.

The significance of all this is that TSA together with standard boundary conditions across the boundary allows us to write the entire problem in terms of *exterior* field quantities(17). These in turn can be solved for in terms of a simple set of *scalar* auxiliary source strengths, distributed relatively sparsely over an auxiliary surface. We term this combination the combined MAS-TSA algorithm, because it retains an MAS formulation for the exterior field, but treats the interior field only through the TSA. The "full MAS" designates an MAS formulation applied to both interior and exterior regions. One can also mix MAS and TSA in another sense, namely applying the full MAS where it is appropriate, and easily switching to the combined MAS/TSA where it is appropriate. This is fact provides a full EMI band simulator.

1.5   The single-dipole approximation

According to the Huygens Equivalence Principle, an object's entire response to a given excitation can be approximated as the summation of magnetic fields produced by

elementary magnetic dipoles/charges placed on a closed surface surrounding the target. Using the superposition principle, this set of dipoles can be approximated as one independent aggregate dipole. In the simple dipole model, the secondary magnetic field at $\mathbf{r}$ due to a dipole of moment $\mathbf{m}$ is:

$$\mathbf{H} = \frac{1}{4\pi R^3}(3\hat{\mathbf{R}}\hat{\mathbf{R}} - \bar{\bar{\mathbf{I}}}) \cdot \mathbf{m} \equiv \bar{\bar{\mathbf{G}}} \cdot \mathbf{m} \tag{21}$$

where $\hat{\mathbf{R}}$ is the unit vector along $\mathbf{R} = \mathbf{r}' - \mathbf{r}_d$, $\mathbf{r}_d$ is the dipole's position, and $\bar{\bar{\mathbf{I}}}$ is the identity dyad (see **Error! Reference source not found.**). The dipole moment $\mathbf{m}$ induced by the primary magnetic field $\mathbf{H}^{\mathrm{pr}}$ is given by

$$\mathbf{m} = \bar{\bar{\mathbf{M}}} \cdot \mathbf{H}^{\mathrm{pr}}(\mathbf{r}', \mathbf{r}_d) , \tag{22}$$

where $\bar{\bar{\mathbf{M}}}$, the target's magnetic polarizability tensor, is a symmetric matrix: $\mathbf{M}_{\alpha\beta} = \mathbf{M}_{\beta\alpha}$, $\alpha, \beta = x, y, z$. This tensor depends on the scatterer's shape, size, and material properties. In a coordinate system aligned with the scatterer's principal axes for different primary magnetic fields $\mathbf{H}^{\mathrm{pr}}(\mathbf{r}, \mathbf{r}_d)$, (22) can be written in matrix form as

$$\left[\mathbf{m}\right] = \bar{\bar{\mathbf{M}}} \cdot \left[\mathbf{H}^{\mathrm{pr}}\right]. \tag{23}$$
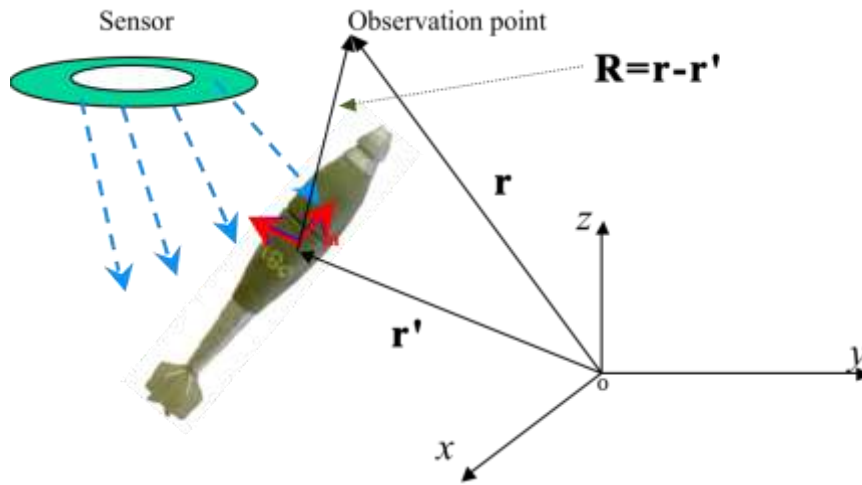
Figure 1.3: A dipole's location in a global coordinate system

Thus the secondary magnetic field is

$$\mathbf{H} = \bar{\bar{\mathbf{G}}} \cdot \bar{\bar{\mathbf{M}}} \cdot \left[\mathbf{H}^{\mathrm{pr}}\right] \equiv [\bar{\bar{\Upsilon}}] \cdot \left[\mathbf{M}\right]^{T} , \tag{24}$$

Where [**M**] is a 1×6 dimensional vector whose components (M_{xx}, M_{xy}, M_{xz}, M_{yy}, M_{yz}, M_{zz}) correspond to the elements of the target's magnetic polarizability tensor $\bar{\bar{\mathbf{M}}}$ and [Υ] is a 3×6 matrix,

$$\bar{\bar{\Upsilon}} = \frac{1}{4\pi R^5} \begin{pmatrix} \Upsilon_{11} & \Upsilon_{12} & \Upsilon_{13} & \Upsilon_{14} & \Upsilon_{15} & \Upsilon_{16} \\ \Upsilon_{21} & \Upsilon_{22} & \Upsilon_{23} & \Upsilon_{24} & \Upsilon_{25} & \Upsilon_{26} \\ \Upsilon_{31} & \Upsilon_{32} & \Upsilon_{33} & \Upsilon_{34} & \Upsilon_{35} & \Upsilon_{36} \end{pmatrix}, \tag{25}$$

whose elements are as follows:

$$\Upsilon_{11} = H_x^{\mathrm{pr}}\left(3R_x^2 - R^2\right) \qquad \Upsilon_{12} = 3R_x\left(R_x H_y^{\mathrm{pr}} + R_y H_x^{\mathrm{pr}}\right) - H_y^{\mathrm{pr}} R^2 \qquad \Upsilon_{13} = 3R_x\left(R_x H_z^{\mathrm{pr}} + R_z H_x^{\mathrm{pr}}\right) - H_z^{\mathrm{pr}} R^2$$

$$\Upsilon_{14} = 3R_x R_y H_y^{\mathrm{pr}} \qquad \Upsilon_{15} = 3R_x\left(R_y H_z^{\mathrm{pr}} + R_z H_y^{\mathrm{pr}}\right) \qquad \Upsilon_{16} = 3R_x R_z H_z^{\mathrm{pr}}$$

$$\Upsilon_{21} = 3R_y R_x H_x^{\mathrm{pr}} \qquad \Upsilon_{22} = 3R_y\left(R_x H_y^{\mathrm{pr}} + R_y H_x^{\mathrm{pr}}\right) - H_x^{\mathrm{pr}} R^2 \qquad \Upsilon_{23} = 3R_y\left(R_x H_z^{\mathrm{pr}} + R_z H_x^{\mathrm{pr}}\right)$$

$$\Upsilon_{24} = H_y^{\mathrm{pr}}\left(3R_y^2 - R^2\right) \qquad \Upsilon_{25} = 3R_y\left(R_y H_z^{\mathrm{pr}} + R_z H_y^{\mathrm{pr}}\right) - H_z^{\mathrm{pr}} R^2 \qquad \Upsilon_{26} = 3R_y R_z H_z^{\mathrm{pr}}$$

$$\Upsilon_{31} = 3R_z R_x H_x^{\mathrm{pr}} \qquad \Upsilon_{32} = 3R_z\left(R_x H_y^{\mathrm{pr}} + R_y H_x^{\mathrm{pr}}\right) \qquad \Upsilon_{33} = 3R_z\left(R_x H_z^{\mathrm{pr}} + R_z H_x^{\mathrm{pr}}\right) - H_x^{\mathrm{pr}} R^2$$

$$\Upsilon_{34} = 3R_z R_y H_y^{\mathrm{pr}} \qquad \Upsilon_{35} = 3R_z\left(R_y H_z^{\mathrm{pr}} + R_z H_y^{\mathrm{pr}}\right) - H_y^{\mathrm{pr}} R^2 \qquad \Upsilon_{36} = H_z^{\mathrm{pr}}\left(3R_z^2 - R^2\right)$$

Once the vector **M** is determined the magnetic polarizability tensor $\bar{\bar{\mathbf{M}}}$ is constructed as

$$\bar{\bar{\mathbf{M}}} = \begin{pmatrix} M_{xx} & M_{xy} & M_{xz} \\ M_{xy} & M_{yy} & M_{yz} \\ M_{xz} & M_{yz} & M_{zz} \end{pmatrix}, \tag{26}$$

and finally the $\bar{\bar{\mathbf{M}}}$ tensor's principal polarizability elements are determined in the target frame coordinate system, which is related to the global coordinate system via the Euler rotation tensor $\bar{\bar{\mathbf{A}}}(\psi, \theta, \phi)$, as

$$\bar{\bar{\mathbf{M}}} = \bar{\bar{\mathbf{A}}}\, \bar{\bar{\boldsymbol{\beta}}}\, \bar{\bar{\mathbf{A}}}^{\mathrm{T}} \equiv \bar{\bar{\mathbf{A}}} \begin{pmatrix} \beta_{xx} & 0 & 0 \\ 0 & \beta_{yy} & 0 \\ 0 & 0 & \beta_{zz} \end{pmatrix} \bar{\bar{\mathbf{A}}}^{\mathrm{T}}. \tag{27}$$

Body-of-revolution (BOR) symmetry (which most UXO possess) dictates that $\beta_{xx} = \beta_{yy}$ and that the third Euler angle ψ is zero. We thus obtain

$$\bar{\bar{\mathbf{A}}} = \begin{bmatrix} \cos\theta\cos\phi & \cos\theta\sin\phi & -\sin\theta \\ -\sin\phi & \cos\phi & 0 \\ \sin\theta\cos\phi & \sin\theta\sin\phi & \cos\theta \end{bmatrix},$$

(28)

where θ and ϕ are the angles between the local and global axes. Note that the tensor $\bar{\bar{\mathbf{M}}}$ depends on time or frequency while the Euler tensor does not. This suggests that one could apply joint diagonalization to separate the polarizability eigenvalues from the rotational eigenvectors; the attitude angles can in turn be extracted from the latter.

1.6 NSMS Method

1.6.1 Theoretical basis of NSMS

The NSMS model is based upon the assumption that the entire scatterer can be replaced with an auxiliary very thin surface shell. The primary magnetic field strikes the shell and induces on it a surface magnetization, in terms of which the secondary scalar potential can be written as [5]

$$\psi^{sc}(\mathbf{r}) = \frac{1}{4\pi} \oiint_S \mathbf{M}(\mathbf{r}') \cdot \nabla' \frac{1}{R} ds'$$

(29)

Here $\mathbf{R} = \mathbf{r} - \mathbf{r}'$, where $\mathbf{r}$ is the observation point and $\mathbf{r}'$ is on the surface S, and $\mathbf{M}(\mathbf{r}')$ is a surface density of magnetization, which can be defined as the induced magnetic moment per unit surface: $\mathbf{m} = \oiint_S \mathbf{M}(\mathbf{r}') ds'$. The surface density $\mathbf{M}$ of magnetic polarization may be resolved at every point on S into normal and tangential components by means of the identity

$$\mathbf{M} = (\hat{\mathbf{n}} \cdot \mathbf{M})\hat{\mathbf{n}} + (\hat{\mathbf{n}} \times \mathbf{M}) \times \hat{\mathbf{n}},$$

(30)

and combining (30), (29) and **Error! Reference source not found.** we get for the total scattered magnetic field

$$\mathbf{H}^{sc}(\mathbf{r}) = -\frac{1}{4\pi} \nabla \oiint_S (\hat{\mathbf{n}}' \cdot \mathbf{M}(\mathbf{r}'))\hat{\mathbf{n}}' \cdot \nabla' \frac{1}{R} ds'$$
$$-\frac{1}{4\pi} \nabla \oiint_S (\hat{\mathbf{n}}' \times \mathbf{M}(\mathbf{r}')) \times \hat{\mathbf{n}}' \cdot \nabla' \frac{1}{R} ds'.$$

(31)

The first integral in (31) may be interpreted as a scalar potential due to a double layer of moment

$$\boldsymbol{\tau}(\mathbf{r}') = (\hat{\mathbf{n}}' \cdot \mathbf{M}(\mathbf{r}'))\hat{\mathbf{n}}' = \sigma_m(\mathbf{r}')\hat{\mathbf{n}}',$$

(32)

and the second may be interpreted as a scalar potential due to a "free" magnetic charge distribution proportional to a discontinuity in the normal components of magnetic flux.

Since the normal component of the magnetic field is always continuous across a boundary between two media, the total scattered magnetic field can thus be written as

$$\mathbf{H}^{sc}(\mathbf{r}) = -\nabla \oiint_S \sigma_m(\mathbf{r}')g(\mathbf{r},\mathbf{r}')\,ds'$$

(33)

where

$$g(\mathbf{r},\mathbf{r}') = \frac{1}{4\pi}\hat{\mathbf{n}}'\cdot\nabla'\frac{1}{|\mathbf{r}-\mathbf{r}'|}.$$

(34)

Thus the EMI response of a permeable and conducting metallic object can be represented using a surface density $\sigma_m(s')$. At every point, the magnetic flux density $\mathbf{B}$ is

$$\mathbf{B} = \mu_0(\mathbf{H}+\mathbf{M}).$$

(35)

Using Gauss's law for the magnetic flux density in the volume enclosed by S and using the divergence theorem we obtain

$$\int_V \nabla\cdot\mathbf{B}\,dv = \mu_0 \oiint_S (\mathbf{H}\cdot\hat{\mathbf{n}}'+\mathbf{M}\cdot\hat{\mathbf{n}}')ds'$$
$$= \mu_0 \oiint_S (H_n(\mathbf{r}')+\sigma_m(\mathbf{r}'))ds' = 0,$$

(36)

and it follows that the magnetization density at a given point on the surface equals

$$\sigma_m(s') = -H_n(s') = -(H_n^{pr}(s')+H_n^{sc}(s'))$$
$$= -H_n^{pr}(s')(1+P(s')),$$

(37)

where $P(s')$ is in general position-dependent on S surface. In other words, the surface magnetic charge is proportional to the normal component $H_n^{pr}(s')$ of the primary magnetic field. This motivates us to introduce a normalized surface distribution $\Omega(s')$ through

$$\sigma_m(s') \equiv -\Omega(s')[\mathbf{H}^{pr}(s')\cdot\hat{\mathbf{n}}'],$$

(38)

which would result from exciting each patch of the surface S with a nonphysical unit primary magnetic field in the normal direction. After combining (33) and (38), the total scattered magnetic field can be expressed as

$$\mathbf{H}^{sc}(\mathbf{r}) = \oiint_S \Omega(\mathbf{r}')[\mathbf{H}^{pr}(\mathbf{r}')\cdot\hat{\mathbf{n}}']\nabla g(\mathbf{r},\mathbf{r}')ds'$$
$$= \oiint_S \Omega(\mathbf{r}')[\mathbf{H}^{pr}(\mathbf{r}')\cdot\hat{\mathbf{n}}']\frac{3\mathbf{R}(\mathbf{R}\cdot\hat{\mathbf{n}}')-R^2\hat{\mathbf{n}}'}{4\pi R^5}ds'.$$

(39)

In the following we will argue that Ω, and in particular its integral over the surface,

$$Q = \oiint_S \Omega \, ds' ,$$

(40)

contains all the information about an object that could be of need in the UXO discrimination problem, incorporating the effects of heterogeneity, interaction with other objects, and near- and far-field effects. We note that Q has dimensions of volume, which makes it comparable to the polarizability tensor elements of the point dipole model [6-13].

1.6.2 Formulation for bodies of revolution; determining NSMS amplitudes from data

Most UXO are bodies of revolution (BOR), and the simplicity and efficiency afforded by this simplification motivates specializing the above analysis to scatterers with BOR symmetry. The best choice for auxiliary surface is a prolate spheroid, since it has BOR symmetry but at the same time has the elongated shape of UXO and can be made to have a definite orientation. We take a spheroid of semiminor and semimajor axes a and $b \equiv ea$ with $e > 1$. In the prolate spheroidal coordinate system (ξ, η, φ) we can write (39) in the form (see Figure 4)

$$\mathbf{H}^{\mathrm{sc}}(\mathbf{r}) = \int_{-1}^{1} h_{\eta'} d\eta' \int_{0}^{2\pi} h_{\varphi'} d\varphi' \, \Omega(\eta', \xi_0, \varphi') \, [\mathbf{H}^{\mathrm{pr}}(\mathbf{r}') \cdot \hat{\boldsymbol{\xi}}'] \nabla g(\mathbf{r}, \mathbf{r}') ,$$

(41)

where the prolate spheroidal coordinates obey $-1 \le \eta \le 1$, $0 \le \xi < \infty$, $0 \le \varphi \le 2\pi$, $\mathbf{r}$ is the observation point, h_η and h_φ are the metric coefficients

$$h_\eta = \frac{d}{2} \sqrt{\frac{\xi_0^2 - \eta^2}{1 - \eta^2}} \quad \text{and} \quad h_\varphi = \frac{d}{2} \sqrt{(1 - \eta^2)(\xi_0^2 - 1)} ,$$

(42)

the spheroid is characterized by $\xi_0 = e / \sqrt{e^2 - 1}$, and $d = 2\sqrt{b^2 - a^2}$ is the focal distance.

For a body with BOR symmetry the NSMS amplitude is azimuthally constant, and moreover the variation of the induced magnetic charge density σ is accounted for by the normal component of the primary magnetic field. This implies that $\Omega(\eta', \xi_0, \varphi') = \Omega(\eta')$. For convenience we define

$$\mathbf{H}^{\mathrm{sc}}(\mathbf{r}) = \int_{-1}^{1} \Omega(\eta') \mathbf{K}(\eta', \mathbf{r}) \, d\eta' ,$$

(43)

where

$$\mathbf{K}(\eta', \mathbf{r}) = \int_{0}^{2\pi} [\mathbf{H}^{\mathrm{pr}}(\mathbf{r}') \cdot \hat{\boldsymbol{\xi}}'] \nabla g(\mathbf{r}, \xi_0, \eta', \varphi') h_\eta h_{\varphi'} d\varphi' ,$$

(44)

and assume that the NSMS can be approximated by a series of expansion functions $F_m(\eta')$ such that

$$\Omega(\eta') = \sum_{m=1}^{M} \Omega_m F_m(\eta')$$

(45)
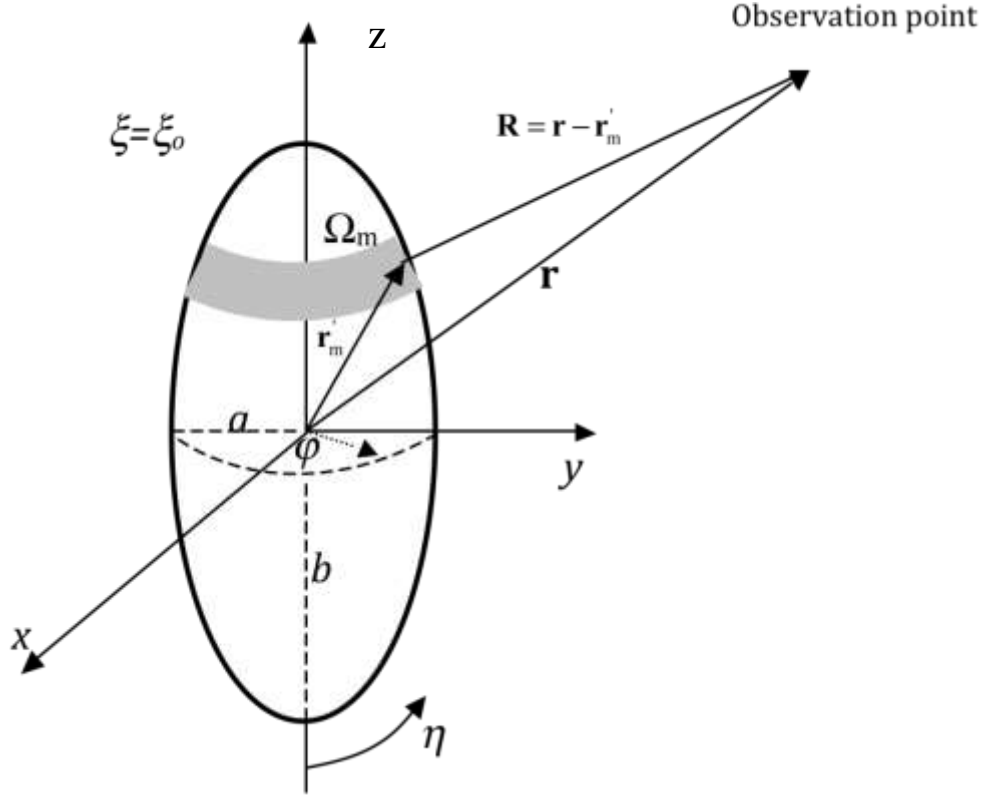
Figure 4: The NSMC that are distributed on a prolate spheroidal surface is implemented for a body of revolution. The prolate spheroidal coordinate system is specified by (ξ, η, φ).

For computational simplicity, in the subsequent analysis we assume the expansion functions $F_m(\eta)$ are a set of orthogonal pulse functions given by

$$F_m(\eta') = \begin{cases} 1, & \eta' \in \Delta\eta_m \\ 0, & \text{otherwise.} \end{cases}$$

(46)

The expansion in terms of pulse functions is a "stairstep" approximation to the NSMS distribution on the spheroid along η', where the spheroidal surface is divided into M belts. The expansion coefficient Ω_m thus corresponds to the NSMS amplitude at the m-th belt. Substituting into (43) we obtain

$$\mathbf{H}^{sc}(\mathbf{r}) = \int_{-1}^{1} \sum_{m=1}^{M} \Omega_m F_m(\eta') \mathbf{K}(\eta', \mathbf{r}) \, d\eta'$$

,

(47)

and the use of (46) in (47) enables us to write

$$\mathbf{H}^{\text{sc}}(\mathbf{r}) = \sum_{m=1}^{M} \Omega_m \int_{\Delta\eta_m} \mathbf{K}(\eta,\mathbf{r}) \, d\eta \equiv \sum_{m=1}^{M} \Omega_m \mathbf{f}(\eta_m,\mathbf{r})$$
$$= \Omega_1 \mathbf{f}(\eta_1,\mathbf{r}) + \Omega_2 \mathbf{f}(\eta_2,\mathbf{r}) + \cdots + \Omega_M \mathbf{f}(\eta_M,\mathbf{r}).$$

(48)

The physical interpretation of this equation is as follows. The spheroid has been divided up to M belts, each of surface $\Delta s_m = 2\pi h_{\eta'}^m h_{\varphi'}^m \Delta\eta_m$, as shown in Figure 4, with the NSMS being an unknown constant over each belt. At the center of each segment, the sum of the scattered fields from all M belts is set to equal the measured field $\mathbf{H}^{\text{data}}(\mathbf{r})$ at point $\mathbf{r}$ that is a known field arising from the scatterer. For a point $\mathbf{r}_n$ the latter equation leads to

$$\sum_{m=1}^{M} \Omega_m \mathbf{f}(\eta_m,\mathbf{r}_n) = \mathbf{H}^{\text{data}}(\mathbf{r}_n)$$

(49)

So far we have only generated one equation (or three if we have access to the full vector field) with M unknowns. We can obtain additional independent equations by using data collected at different points $\mathbf{r}_n$ with $n = 1, 2, \ldots, N$. Matching the modeled scattered magnetic field to the data at these N points results in the linear system

$$[\mathbf{Z}_{mn}][\mathbf{\Omega}_m] = [\mathbf{H}^{\text{data}}(\mathbf{r}_n)] ,$$

(50)

with

$$[\mathbf{Z}_{mn}] = \begin{bmatrix} \mathbf{f}(\eta_1,\mathbf{r}_1) & \mathbf{f}(\eta_2,\mathbf{r}_1) & \cdots & \mathbf{f}(\eta_M,\mathbf{r}_1) \\ \mathbf{f}(\eta_1,\mathbf{r}_2) & \mathbf{f}(\eta_2,\mathbf{r}_2) & \cdots & \mathbf{f}(\eta_M,\mathbf{r}_2) \\ \vdots & \vdots & \ddots & \vdots \\ \mathbf{f}(\eta_1,\mathbf{r}_N) & \mathbf{f}(\eta_2,\mathbf{r}_N) & \cdots & \mathbf{f}(\eta_M,\mathbf{r}_N) \end{bmatrix},$$

$$[\mathbf{\Omega}_m] = \begin{bmatrix} \Omega_1 & \Omega_2 & \ldots & \Omega_M \end{bmatrix}^{\text{T}},$$

$$[\mathbf{H}^{\text{data}}(\mathbf{r}_n)] = \begin{bmatrix} \mathbf{H}^{\text{data}}(\mathbf{r}_1) & \mathbf{H}^{\text{data}}(\mathbf{r}_2) & \mathbf{H}^{\text{data}}(\mathbf{r}_N) \end{bmatrix}^{\text{T}},$$

(51)

and $\mathbf{f}(\eta_m, \mathbf{r}_n)$ given by (48), whose solution can be written symbolically as

$$[\mathbf{\Omega}_m] = \frac{[\mathbf{Z}_m]^{\text{T}}[\mathbf{H}^{\text{data}}(\mathbf{r}_n)]}{[\mathbf{Z}_m]^{\text{T}}[\mathbf{Z}_m]} .$$

(52)

Once $[\mathbf{\Omega}_m]$ is determined the object's EMI response can be computed readily. The resulting discrete NSMS distribution can then be used to compute the total NSMS amplitude, which is a global measure of Ω for the entire object and can be used for discrimination:

$$Q = \sum_{m=1}^{M} \Omega_m \Delta S_m .$$

(53)

In the following sections we study some features of this global measure of response.

1.6.3   The dipole model as a limiting case of NSMS

Here we show that NSMS reduces in the limit to the point dipole model [6-11] of Section 1.5. Recall that the magnetic field due to a dipole of moment $\mathbf{m}$ is

$$\mathbf{H}^{sc}(\mathbf{r}) = \frac{1}{4\pi R^3}\mathbf{m}\cdot(3\hat{\mathbf{R}}\hat{\mathbf{R}} - \overline{\overline{\mathbf{I}}}),$$

(54)

where $\hat{\mathbf{R}}$ is the unit vector along $\mathbf{R} = \mathbf{r} - \mathbf{r}_d$ and $\mathbf{r}_d$ and $\mathbf{r}$ are respectively the location of the dipole and the observation point, as seen in Figure 5, while $\overline{\overline{\mathbf{I}}}$ is the identity dyad. The relation between the induced dipole moment $\mathbf{m}$ and the primary magnetic field $\mathbf{H}^{pr}$ at the dipole location is given by

$$\mathbf{m} = \overline{\overline{\mathbf{M}}}\cdot\mathbf{H}^{pr}(\mathbf{r}_d),$$

(55)

where the magnetic polarizability tensor $\overline{\overline{\mathbf{M}}}$ depends on the scatterer's shape, size, and material properties. For a body of revolution, the polarizability tensor in a coordinate system aligned with the scatterer's principal axes can be written as

$$\overline{\overline{\mathbf{M}}} = \begin{bmatrix} \beta_{\rho\rho} & 0 & 0 \\ 0 & \beta_{\rho\rho} & 0 \\ 0 & 0 & \beta_{zz} \end{bmatrix}$$

(56)

where the degeneracy in the "radial" element $\beta_{\rho\rho}$ displays the BOR symmetry explicitly. The target's principal axes and the global coordinate system are related by the Euler rotation tensor.

Now let us prove that in the dipole model is a limited case of the NSMS. To do that, first let us divide the surrounding spheroidal surface into three belts and assume that on the m-th belt the NSMS density follows a Dirac delta distribution (see Figure 5). With these assumptions the scattered magnetic field (54) becomes

$$\mathbf{H}^{sc}(\mathbf{r}) = \frac{1}{4\pi}\sum_{m=1}^{3}\frac{1}{R_m^3}\Omega_m H_m^{pr}(\mathbf{r}_m)\hat{\mathbf{n}}_m\cdot(3\hat{\mathbf{R}}_m\hat{\mathbf{R}}_m - \overline{\overline{\mathbf{I}}})$$

(57)

where now $\mathbf{R} = \mathbf{r} - \mathbf{r}_m$ points from $\mathbf{r}_m$ on the m-th belt to the observation point. As $S \to 0$ we have that $\mathbf{r}_m \to \mathbf{r}_d$, and $H_n^{pr}(\mathbf{r}_m) = H_n^{pr}(\mathbf{r}_d)$, and because $\hat{\mathbf{n}}_2 = \hat{\boldsymbol{\rho}} = \alpha_1\hat{\mathbf{x}} + \alpha_2\hat{\mathbf{y}}$, and $\hat{\mathbf{n}}_1 = -\hat{\mathbf{n}}_3 = \hat{\mathbf{z}}$, ($\alpha_1 = \cos\alpha$ and $\alpha_2 = \sin\alpha$, where α is the angle between $\hat{\boldsymbol{\rho}}$ and $\hat{\mathbf{x}}$) then (57) reduces to

$$\mathbf{H}^{sc}(\mathbf{r}) = \frac{3\hat{\mathbf{R}}\hat{\mathbf{R}} - \bar{\bar{\mathbf{I}}}}{4\pi R^3} \cdot (2\Omega_1 H_z^{pr}(\mathbf{r}_d)\hat{\mathbf{z}} + \Omega_2(H_x^{pr}(\mathbf{r}_d)\alpha_1\hat{\mathbf{x}} + H_x^{pr}(\mathbf{r}_d)\alpha_2\hat{\mathbf{y}}))$$

(58)

in terms of the Cartesian unit vectors $\hat{\mathbf{x}}$, $\hat{\mathbf{y}}$, and $\hat{\mathbf{z}}$. After introducing a diagonal tensor

$$\bar{\bar{\mathbf{M}}}_n = \begin{bmatrix} \Omega_2 & 0 & 0 \\ 0 & \Omega_2 & 0 \\ 0 & 0 & 2\Omega_1 \end{bmatrix}$$

(59)

and the vector $\mathbf{m}_n = \bar{\bar{\mathbf{M}}}_n \cdot \mathbf{H}^{pr}(\mathbf{r}_d)$, (58) can be written as

$$\begin{aligned} \mathbf{H}^{sc}(\mathbf{r}) &= \frac{1}{4\pi R^3}\mathbf{m}_n \cdot (3\hat{\mathbf{R}}\hat{\mathbf{R}} - \bar{\bar{\mathbf{I}}}) \\ &= \frac{1}{4\pi R^3}[\bar{\bar{\mathbf{M}}}_n \cdot \mathbf{H}^{pr}(\mathbf{r}_d)] \cdot (3\hat{\mathbf{R}}\hat{\mathbf{R}} - \bar{\bar{\mathbf{I}}}), \end{aligned}$$

(60)

which proves that in the limit the NSMS model is identical to the infinitesimal dipole approximation.
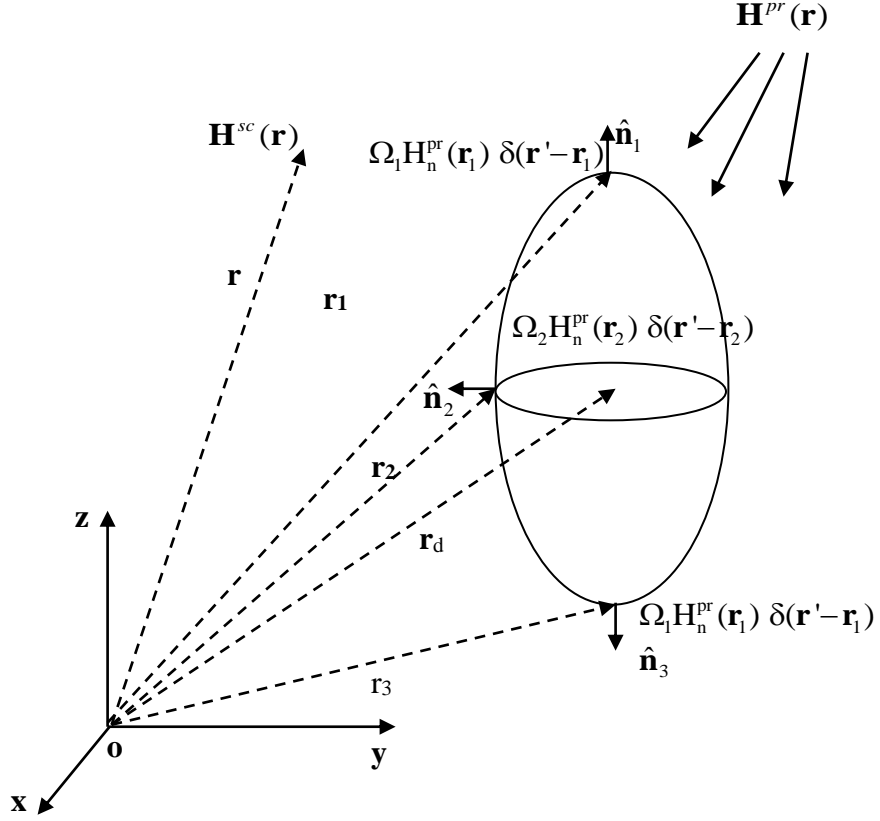
Figure 5: A schematic diagram for a dipole model.

1.6.4 Interpretation of the total NSMS

The total NSMS (and its time evolution) depends on the size, geometry, and material composition of the object in question. Early time gates bring out the high-frequency response to the shutdown of the exciting field; the induced eddy currents in this range are superficial, and a large NSMS amplitude at early times correlates with large objects whose surface stretches wide. At late times, where the eddy currents have diffused completely into the object and low-frequency harmonics dominate, the EMI response relates to the metal content (*i.e.*, the volume) of the target. Thus a smaller but compact object has a relatively weak early response that dies down slowly, while a large but thin or hollow object has a strong initial response that decays quickly. These features can be neatly summarized by the parameters of an empirical decay-law model like the Pasion-Oldenburg law see (64).

1.6.5 The parameterized NSMS

During APG standardized test-site discrimination studies (see Chapter 3.4) we use a parameterized version of NSMS to encapsulate the electromagnetic signature of a target [14]. In this version of the model—which provides at least three independent polarizability-like parameters for use in discrimination and thus in a sense extracts further information from the same data—the scatterer is associated with a surrounding sphere S on which a set of dipoles are distributed. The secondary field is expressed as

$$\mathbf{H}^{sc}(\mathbf{r},t)=\iint_S \frac{3\hat{\mathbf{R}}_{s'}\hat{\mathbf{R}}_{s'}-\mathbf{1}}{4\pi R_{s'}^3}\cdot\left\{\begin{bmatrix}\Omega_{xx}(\mathbf{r}_{s'},t) & \Omega_{xy}(\mathbf{r}_{s'},t) & \Omega_{xz}(\mathbf{r}_{s'},t) \\ \Omega_{yx}(\mathbf{r}_{s'},t) & \Omega_{yy}(\mathbf{r}_{s'},t) & \Omega_{yz}(\mathbf{r}_{s'},t) \\ \Omega_{zx}(\mathbf{r}_{s'},t) & \Omega_{zy}(\mathbf{r}_{s'},t) & \Omega_{zz}(\mathbf{r}_{s'},t)\end{bmatrix}\right\}\begin{bmatrix}H_x^{pr}(\mathbf{r}_{s'}) \\ H_y^{pr}(\mathbf{r}_{s'}) \\ H_z^{pr}(\mathbf{r}_{s'})\end{bmatrix}ds'\equiv\ddot{\mathbf{Z}}\cdot\mathbf{\Omega}, \qquad (61)$$

where $\mathbf{R}_{s'}$ points from the location $\mathbf{r}_{s'}$ of the s'-th patch on the sphere to the observation point $\mathbf{r}$ and the response amplitude of each patch is a combination of the primary field piercing it and the tensor of normalized strengths $\Omega_{ij}(\mathbf{r}_{s'},t)$, which, as usual [15], is symmetric: $\Omega_{ij}=\Omega_{ji}$. The z-axis is dictated by the direction of $\mathbf{m}$ from HAP or from the dipole model, and the x- and y-axes are arbitrarily chosen to be perpendicular to $\hat{\mathbf{z}}$ and to each other. The integral is again transformed to a matrix-vector product through numerical quadrature. The amplitude array $\mathbf{\Omega}$ is determined by minimizing in a least-squares sense the difference between measured data with a known object-sensor configuration and the predictions of equation (61). Once the tensor elements $\Omega_{ij}(s')$ are found one can define "total polarizabilities" by integrating over the sphere,

$$Q_{ij}(t)=\iint_S\Omega_{ij}(\mathbf{r}_{s'},t)\,ds'\,, \qquad (62)$$

and these can in turn be used to find "principal elements" through joint diagonalization:

$$\begin{bmatrix}Q_{xx}(t) & Q_{xy}(t) & Q_{xz}(t) \\ Q_{yx}(t) & Q_{yy}(t) & Q_{yz}(t) \\ Q_{zx}(t) & Q_{zy}(t) & Q_{zz}(t)\end{bmatrix}=\mathbf{\Lambda}\begin{bmatrix}Q_x(t) & 0 & 0 \\ 0 & Q_y(t) & 0 \\ 0 & 0 & Q_z(t)\end{bmatrix}\mathbf{\Lambda}'\,, \qquad (63)$$

where the matrix $\mathbf{\Lambda}$ is orthogonal and the prime denotes transposition. The information contained in the diagonal tensor can be summarized further by incorporating the empirical decay law of Pasion and Oldenburg [16]:

$$M_{\alpha\alpha}(t)\equiv Q_\alpha(t)=B_{\alpha\alpha}t^{-\beta_{\alpha\alpha}}e^{-\gamma_{\alpha\alpha}t}\,,\quad \alpha=x,\,y,\,z\,, \qquad (64)$$

where t is the time, $B_{\alpha\alpha}$, $\beta_{\alpha\alpha}$, and $\gamma_{\alpha\alpha}$ are the fitting parameters, and $M_{\alpha\alpha}(t)$ is the total NSMS along the x, y, and z directions in the body frame. The principal NSMS elements and the Pasion-Oldenburg parameters are intrinsic to the object and can be used, on their own or in combination with other quantities, in discrimination processing.

1.7   The orthonormalized volume magnetic source model

Most EMI sensors are composed of separate transmitting and receiving coils. When the operator activates the sensor, a current runs through the transmitter coils, which results in the establishment of a ("primary" or "principal") magnetic field in the surrounding space (Figure 1.2). According to the elementary atomic model of matter, all materials are composed of atoms, each with a positively charged nucleus and a number of orbiting negatively charged electrons. The orbiting electrons cause circulating currents and form microscopic magnetic dipoles. In the absence of an external magnetic field the magnetic dipoles of atoms of most materials have random orientations, resulting in no magnetic moment. The application of an external time varying magnetic field, by Faraday's law, induces eddy currents in highly conducting bodies by an alignment of the magnetic moments of the spinning electrons and a magnetic moment due to a change in the orbital motion of electrons. These currents and magnetization in turn generate a ("secondary" or "scattered") magnetic field that also varies with time and induces measurable currents in the receiving coils. The induced magnetic dipoles/eddy currents are distributed inside the object and produce a magnetic field intensity $\mathbf{H}$ outside. The magnetic field due to the i-th source can then be expressed at any observation point $\mathbf{r}$ as the matrix-vector product

$$\mathbf{H}_i(\mathbf{r}) = G_i(\mathbf{r})\mathbf{m}_i, \tag{65}$$

Where the Green function G_i is given in detail in equation (21). When there are several such sources, the total field can be expressed as a superposition:

$$\mathbf{H}(\mathbf{r}) = \sum_{i=1}^{M} G_i(\mathbf{r})\mathbf{m}_i = \begin{bmatrix} G_1 & G_2 & \cdots \end{bmatrix} \begin{bmatrix} \mathbf{m}_1 \\ \mathbf{m}_2 \\ \vdots \end{bmatrix}. \tag{66}$$

Before going further we note that our method takes as input the (in principle unknown) number M of radiating sources. For advanced EMI sensors such as the MetalMapper and 2×2 and 5×5 TEMTADS arrays we have developed a procedure based on joint diagonalization, sketched in Section 1.10, that estimates M starting from raw data and with no need for inversion. For other sensors one may proceed by letting M vary as part of an optimization routine.
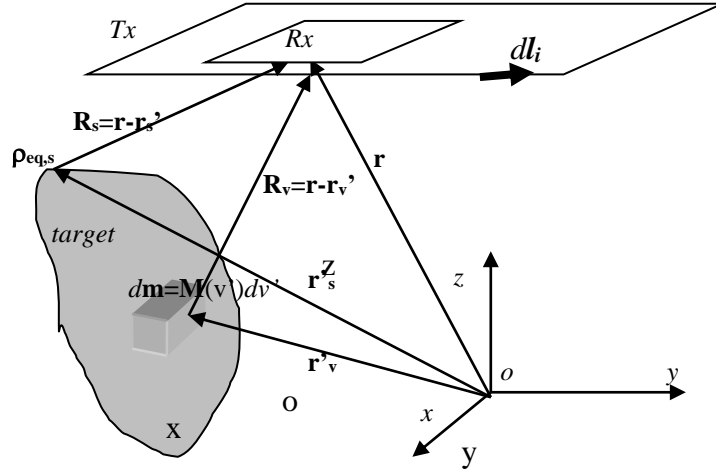
Figure 1.6: A metallic object under the transmitter. The target's
EMI response at the receiver coil can be calculated from the
equivalent surface or volume magnetic dipole moment dm.

The superposition (66) can be used (and often has) to carry out one- and multi-object inversions starting from data taken at an ensemble of points. All the measured $\mathbf{H}$-values—which can pertain to multiple transmitters, multiple receivers, and different vector components—are strung together in a one-dimensional array, while the corresponding Green functions are stacked as matrix rows. The resulting composite G matrix can then be (pseudo)inverted to find the strengths of the sources. This procedure, which is nothing other than the dipole model if each body is taken to be represented by one source only, works well for one or two sources, but for larger numbers becomes very time-consuming (since the Green matrix becomes very large) and increasingly ill-posed, usually requiring regularization. The ONVMS method is designed to circumvent these difficulties.

1.8 Orthonormal Green functions

The method starts from the realization that the matrix-vector product (65) is valid at any observation point $\mathbf{r}$ and, in particular, at every point $\mathbf{r}_s$. If we introduce the inner product

$$\left\langle A, B \right\rangle = \int_S A^T B \, ds = \int_{\mathrm{Rx}_0} A^T B \, ds + \int_{\mathrm{Rx}_1} A^T B \, ds + \cdots, \tag{67}$$

where the integral is computed over the "sensitive" surfaces of the sensor, and if furthermore we can find a basis of Green functions orthogonal under this measure,

$$\mathbf{H}(\mathbf{r}_s) = \sum_{j=1}^{M} \Psi_j(\mathbf{r}_s)\mathbf{b}_j \quad \text{such that} \quad \left\langle \Psi_j, \Psi_k \right\rangle = F_j \delta_{jk}, \tag{68}$$

where δ_{jk} is a Kronecker delta, then it is possible to find the source amplitudes $\mathbf{b}_j$ without costly and ill-conditioned inversions simply by exploiting the sifting property of the orthogonal basis:

$$\langle \Psi_k, \mathbf{H} \rangle = \sum_{j=1}^{M} \langle \Psi_k, \Psi_j \rangle \mathbf{b}_j = \sum_{j=1}^{M} F_k \delta_{kj} \mathbf{b}_j = F_k \mathbf{b}_k \quad (69)$$

and thus

$$\mathbf{b}_k = F_k^{-1} \langle \Psi_k, \mathbf{H} \rangle, \quad (70)$$

which clearly does not involve solving a linear system of equations; it is necessary to invert only the 6×6 matrix F_k. Moreover, this definition of the coefficients $\mathbf{b}_j$ guarantees that they are "optimal" in the sense that the expansion (68) yields the least mean-square error $\langle \mathbf{H} - \Sigma_{j=1}^{M} \Psi_j \mathbf{b}_j, \mathbf{H} - \Sigma_{j=1}^{M} \Psi_j \mathbf{b}_j \rangle$ [90, 100].

To construct the set of orthonormal Green functions we resort to a generalization of the Gram-Schmidt procedure [91]. Assuming that the Green matrices are linearly independent—i.e., that we cannot have a collection of distinctly located dipole sources combining to produce no measurable field unless their amplitudes all vanish—we define

$$\Psi_1 = G_1,$$
$$\Psi_2 = G_2 - \Psi_1 A_{21},$$
$$\vdots$$
$$\Psi_m = G_m - \sum_{k=1}^{m-1} \Psi_k A_{mk},$$
$$\vdots$$
$$\Psi_M = G_M - \sum_{k=1}^{M-1} \Psi_k A_{Mk}, \quad (71)$$

where the 6×6 matrices A_{jk} obey $A_{jk} = 0$ for $j \le k$. Enforcing the orthogonality relation (68) is equivalent to setting $\langle \Psi_n, G_m \rangle = F_n A_{mn}$ for $n < m$, and using this relation twice in definition (71) we find

$$A_{mn} = F_n^{-1} \left(C_{nm} - \sum_{k=1}^{n-1} A_{nk}^T F_k A_{mk} \right), \quad (72)$$

where the overlap integral $C_{mn} = \langle G_m, G_n \rangle$.

At the end of the process it is necessary to recover an expansion expressed, like (65), in terms of the actual Green functions, in part because the functions Ψ_j are orthogonal (and

defined) only at points on the receivers, and in part because of the non-uniqueness of the coefficients $\mathbf{b}_j$ due to the arbitrary order in which the G_j enter the recursion (71). To that end, we express

$$\Psi_m = \sum_{k=1}^{m} G_k B_{mk}\,,$$

(73)

and to find the coefficients B_{mk} we compare expansion (73) term by term to the definition (71) and use the rule that $A_{jk} = 0$ for $j \le k$ to find

$$B_{mm} = I,\ \text{ the identity,}$$
$$B_{m(m-1)} = -A_{m(m-1)},$$
$$B_{mq} = -\sum_{l=q}^{m-1} B_{lq} A_{ml}\ \text{ for } 1 \le q \le m-2,$$

(74)

in terms of which we recover the physical polarizability elements:

$$\mathbf{H} = \sum_{k=1}^{M} \Psi_k \mathbf{b}_k = \sum_{k=1}^{M}\left(\sum_{l=1}^{k} G_l B_{kl}\right)\mathbf{b}_k = \sum_{l=1}^{M} G_l\left(\sum_{k=l}^{M} B_{kl}\mathbf{b}_k\right) = \sum_{l=1}^{M} G_l \mathbf{m}_l\,.$$

(75)

1.9   ONVMS procedure

With all the pieces in place, we can sketch an algorithm to invert EMI data using the ONVMS model:

1) Given a number of sources and their tentative locations, find the Green tensors $G_i \equiv \bar{\bar{\Upsilon}}$ using equation (25) and compute the overlap integrals G_{mn} using the inner product(67)
.

2) Determine the first normalization factor, $F_1 = \langle G_1, G_1 \rangle$, and use it to find all the Gram-Schmidt coefficients A_{mn} with $n=1$: $A_{m1} = F_1^{-1} C_{1m}$.

3) Set $m=2$; compute, in sequence,

   a) The coefficients A_{mn} with $n = 2,\ldots,m-1$ using equation (72);

   b) The function Ψ_m using the expansion (71);

   c) The normalization factor $F_m = \langle \Psi_m, \Psi_m \rangle$;

Increase m by 1 and iterate until all sources have been included.

1) Once all the A_{mn}, F_m, and Ψ_m are known, find B_{mq} using (74).

2) Use the orthonormality of the new Green functions to determine the source amplitudes using $\mathbf{b}_q = F_q^{-1}\left\langle \Psi_q, \mathbf{H}^{\text{data}} \right\rangle$, as in (70). Take the measured field to be piecewise constant—i.e., constant throughout each receiver—when evaluating the integrals.

3) Use the computed $\mathbf{b}_q$, B_{mq}, and G_m, along with the expansion (75), to generate the secondary field prescribed by the given number of sources at the given locations.

4) Compare the model prediction with the measured data, vary the source locations, and iterate until the least-squares discrepancy between prediction and measurement attains a suitable minimum.

The procedure as written applies to only one time gate, but the extension to fully time-dependent functions is straightforward: we need only substitute the vectors $\mathbf{b}_q$ and $\mathbf{H}^{\text{data}}$ for two-dimensional arrays where the columns denote time. The relations between the two, namely (70) and (75), acquire multiple right-hand-sides, and the optimization mentioned on Step 7 of the algorithm is constrained further. As a final remark we note that rigorously speaking the coefficients $\mathbf{b}_q$ (and, for that matter, the amplitudes $\mathbf{m}_k$) are *not* the polarizabilities themselves but relate more closely to their time derivatives [31,32, 3].

The great advantage of the ONVMS technique is that it takes into account mutual couplings between different parts of targets and avoids matrix singularity problems in cases with multiple objects. Once the polarizability tensor elements and the locations of the elemental responding dipoles are determined one can group them according to their volume distribution. For each group a total polarizability tensor can be computed and diagonalized using joint diagonalization, the topic of Section 1.10. The resulting time-dependent diagonal elements have been shown to be intrinsic to the objects and can be used, on their own or combined with other quantities, in discrimination processin

1.10   Joint diagonalization for multi-target data pre-processing

In real life situations the targets of interest are usually surrounded by natural and artificial debris with metallic content, including, for instance, the remains of ordnance that did explode. Thus it is usually not clear how many objects are producing a given detected signal; all sensing methods, including EMI, are fraught with detection rates that overwhelm cleanup efforts and hike their cost. Here we introduce a data pre-processing technique based on joint diagonalization (JD) that estimates the number of targets present in the field of view of the sensor as it takes a data shot, and, in a good number of cases, even provides the capability to perform real-time characterization and classification of the targets without the need for a forward model.

Joint diagonalization has become an important tool for signal processing and inverse problems, used as part of independent component analysis [92], blind source separation or BSS [93], common principal component analysis, and, more recently, kernel-based nonlinear BSS [95,96]. We further extend the applicability of the method by using it to detect and locate buried targets without the need for inversion. As we say above, a variation of the method can be used to extricate time-dependent electromagnetic signatures from ttitude information. Here we will outline the detailed procedure as applied to the TEMTADS sensor array, a time-domain device with 25 transmitter/receiver pairs that provides 625 measurements over $N_g = 123$ time gates at each sensor location.

1.11 Algorithm for joint diagonalization

The joint diagonalization algorithm we use [95, 96, 105] is a generalization of Jacobi's procedure to find the eigenvalues of a single matrix. Formally we set out to solve the optimization problem

$$\min_{V} \quad \frac{1}{2}\sum_{q=1}^{N_g}\sum_{i\neq j}([VA(t_q)V^T]_{ij})^2$$
$$\text{s.t.} \qquad V^TV = I,$$

(40)

which we accomplish by making repeated Givens-Jacobi similarity transformations designed to gradually accumulate the "content" of the matrices on their diagonals until a certain tolerance level is reached. The transformations are of the form $A(t_q) \rightarrow A'(t_q) = V_{rs}A(t_q)V_{rs}^T$, with the matrix V_{rs} being the identity but with the four elements V_{rr}, V_{rs}, V_{sr}, and V_{ss} replaced by the two-dimensional rotation array

$$\begin{bmatrix} \cos\phi_{rs} & \sin\phi_{rs} \\ -\sin\phi_{rs} & \cos\phi_{rs} \end{bmatrix}, \quad \text{with} \quad \tan 2\phi_{rs} = \frac{f_{rs}}{n_{rs} + \sqrt{f_{rs}^2 + n_{rs}^2}},$$

(41)

Where

$$n_{rs} = \sum_q \left\{[a_{rr}(t_q) - a_{ss}(t_q)]^2 - [a_{rs}(t_q) + a_{sr}(t_q)]^2\right\},$$

(42)

$$f_{rs} = 2\sum_q [a_{rr}(t_q) - a_{ss}(t_q)][a_{rs}(t_q) + a_{sr}(t_q)].$$

(43)

The indices are swept systematically, and the procedure is repeated until convergence is reached. The computational burden is equivalent to that of diagonalizing the matrices one by one. The resulting eigenvalues and eigenvectors are all real because all the MSR matrices are symmetry.

1.12   The multi-static response matrix

JD estimates the eigenvalues and eigenvectors of a square time- or frequency-dependent multi-static response (MSR) matrix synthesized directly from measured values. To construct the MSR matrices one just has to stack the 625 readings at each time gate in a 25×25 array so that each column stands for one of N_t transmitters and each row represents one of N_r receivers:

$$\mathbf{S}(t_k) = \begin{bmatrix} H_{11} & H_{12} & \cdots & H_{1N_t} \\ H_{21} & H_{22} & \cdots & H_{2N_t} \\ \mathsf{M} & \mathsf{M} & \mathsf{O} & \mathsf{M} \\ H_{N_r 1} & H_{N_r 2} & \mathsf{L} & H_{N_r N_t} \end{bmatrix}, \quad k = 1, \mathsf{K}, N_g \tag{44}$$

where the element H_{ij} is the field measured by the i-th receiver when the j-th transmitter is fired. The second step of the procedure is to diagonalize the 123 matrices at one stroke so they all share a single set of orthonormal eigenvectors. In other words, given the MSR matrix $\mathbf{S}(t_k)$ at the k-th time gate, we look for a unitary matrix $\mathbf{V}$ such that the products

$$\mathbf{D}_k = \mathbf{V}^T \mathbf{S}(t_k) \mathbf{V} \tag{45}$$

are "as diagonal as possible" (i.e., their off-diagonal elements vanish within a preset tolerance). By diagonalizing all the matrices simultaneously we separate the time-dependent intrinsic features of the responding sources (and hence the interred objects), which get encapsulated in the eigenvalues, from the other factors—notably the location and orientation of the target with respect to the sensor—that influence the signal but do not change as the data are being taken; these get bundled into the eigenvectors. (The fact that the locations and orientations can be dissociated in this way from the electromagnetic signatures is an upside of the low frequencies of the quasistatic EMI range, because the relevant Green functions are time-independent.) Thus the measured data can be resolved as a superposition of "elemental" sub-signals, each corresponding to an elementary dipolar source, whose combination corresponds to the buried objects. Each source—and the corresponding field singularity—can moreover be localized numerically: the TEMTADS geometry is such that the diagonal of the unprocessed MSR matrix mimics a set of monostatic measurements, akin to those taken with a handheld sensor, which peak sharply when there is a target directly underneath. The maxima in the diagonal thus point to the transmitter/receiver pairs closest to any responding sources. These location estimates can be grouped and correlated to the eigenvalue distributions to estimate target locations.

1.13   Interpretation and diagonalization of the MSR matrix

We now proceed to express our above considerations quantitatively. Initially we consider the transmitter assembly, which in TEMTADS consists of a set of coplanar square loops forming a regular grid. The Biot-Savart law gives the primary magnetic induction

established at the location $\mathbf{r}_i$ of the l-th source when the j-th transmitter antenna (whose area is σ_{Tx_j}) is excited immediately before shutoff by a current I_j:

$$\mathbf{B}_{jl}^{\mathrm{pr}} = \frac{\mu_0 I_j}{4\pi} \sigma_{\mathrm{Tx}_j} \frac{1}{\sigma_{\mathrm{Tx}_j}} \oiint_{\mathrm{Tx}_j} \frac{d\mathbf{l}' \times (\mathbf{r}_l - \mathbf{r}')}{|\mathbf{r}_l - \mathbf{r}'|^3} = \mathbf{g}_{jl}^{\mathrm{pr}} \sigma_{\mathrm{Tx}_j} I_j$$

. (46)

This primary field induces in the l-th source a dipole moment given by

$$\mathbf{m}_{jl} = \mathbf{U}_l \mathbf{\Lambda}_l \mathbf{U}_l^T \mathbf{B}_{jl}^{\mathrm{pr}},$$

(47)

where the Euler rotation matrix $\mathbf{U}$ relates the instrument's coordinate axes to the principal axes of the source, and the diagonal polarizability matrix $\mathbf{\Lambda}_i$, the only quantity intrinsic to the source, measures the strength with which the primary field induces a moment along each of those axes.

According to Faraday's law, the signal measured by a receiver coil is the electromotive force given by the negative of the time derivative of the secondary magnetic flux through the coil. Since the field at point $\mathbf{r}$ of a dipole of moment $\mathbf{m}$ placed at $\mathbf{r}_0$ is given by

$$\mathbf{B} = \frac{\mu_0}{4\pi} \nabla \times \left(\mathbf{m} \times \frac{\mathbf{r} - \mathbf{r}_0}{|\mathbf{r} - \mathbf{r}_0|^3} \right), \quad \text{and thus} \quad \int \mathbf{B} \cdot d\mathbf{s} = -\mathbf{m} \cdot \frac{\mu_0}{4\pi} \oint d\mathbf{l} \times \frac{\mathbf{r} - \mathbf{r}_0}{|\mathbf{r} - \mathbf{r}_0|^3}$$

(48)

by straightforward application of Stokes's theorem, one obtains that the signal sampled at time t_k by the i-th receiver (of area σ_{Rx_i}) when the l-th source is excited by the j-th transmitter is

$$H_{ij}^l(t_k)\sigma_{\mathrm{Rx}_i}\sigma_{\mathrm{Tx}_j} I_j = \frac{\mu_0}{4\pi} \sigma_{\mathrm{Rx}_i} \frac{1}{\sigma_{\mathrm{Rx}_i}} \oiint_{\mathrm{Rx}_i} \frac{d\mathbf{l}_i' \times (\mathbf{r}' - \mathbf{r}_l)}{|\mathbf{r}' - \mathbf{r}_l|^3} \cdot \dot{\mathbf{m}}_{jl}(t_k) = \mathbf{g}_{li}^{\mathrm{sc}}\sigma_{\mathrm{Rx}_i} \cdot \dot{\mathbf{m}}_{jl}(t_k)$$

$$= \mathbf{g}_{li}^{\mathrm{sc}}\sigma_{\mathrm{Rx}_i} \cdot [\mathbf{U}\dot{\mathbf{\Lambda}}_l(t_k)\mathbf{U}^T] \cdot \mathbf{g}_{jl}^{\mathrm{pr}}\sigma_{\mathrm{Tx}_j} I_j,$$

(49)

where a dot over a variable indicates its time derivative. In equations (46) and (49) the line element $d\mathbf{l}'$ lies on the x-y plane, and as a consequence the Green functions are similar in structure to those of the simple model presented in Section 2.2. Note that we have included the exciting current I_j and the transmitter and receiver areas in the definition of the signal; we have explicit knowledge of these quantities and can factor them out. If only the l-th source is illuminated, we construct the MSR matrix for the complete transmitter/receiver array by tiling $N_r \times N_t$ instances of the expression (49):

$$\mathbf{S} = \mathbf{G}^{\mathrm{sc}}\mathbf{U}_l\mathbf{\Lambda}_l\mathbf{U}_l^T(\mathbf{G}^{\mathrm{pr}})^T$$

(50)

where the primary (or transmitter) dyad $\mathbf{G}^{\mathrm{pr}}$ is of size $N_t \times 3$, the secondary (or receiver) dyad $\mathbf{G}^{\mathrm{sc}}$ is of size $N_r \times 3$, and the response matrix $\mathbf{U}\mathbf{\Lambda}_l\mathbf{U}^T$ is 3×3. When there is more than one source present, the MSR matrix of equation (50) is readily generalized:

$$\mathbf{S} = \begin{bmatrix} \mathbf{G}_1^{\mathrm{sc}} & \mathbf{G}_2^{\mathrm{sc}} & \cdots \end{bmatrix} \begin{bmatrix} \mathbf{U}_1\dot{\mathbf{\Lambda}}_1\mathbf{U}_1^T & 0 & \cdots \\ 0 & \mathbf{U}_2\dot{\mathbf{\Lambda}}_2\mathbf{U}_2^T & \cdots \\ \vdots & \vdots & \ddots \end{bmatrix} \begin{bmatrix} (\mathbf{G}_1^{\mathrm{pr}})^T \\ (\mathbf{G}_2^{\mathrm{pr}})^T \\ \vdots \end{bmatrix}$$

$$= \begin{bmatrix} \mathbf{G}_1^{\mathrm{sc}}\mathbf{U}_1 & \mathbf{G}_2^{\mathrm{sc}}\mathbf{U}_2 & \cdots \end{bmatrix} \begin{bmatrix} \dot{\mathbf{\Lambda}}_1 & 0 & \cdots \\ 0 & \dot{\mathbf{\Lambda}}_2 & \cdots \\ \vdots & \vdots & \ddots \end{bmatrix} \begin{bmatrix} (\mathbf{G}_1^{\mathrm{pr}}\mathbf{U}_1)^T \\ (\mathbf{G}_2^{\mathrm{pr}}\mathbf{U}_2)^T \\ \vdots \end{bmatrix},$$

(51)

where we see that the features intrinsic to the targets can be separated formally from the particulars of the measurement—that is, from the geometry and dimensions of the sensor and the sensor-target attitude. The array $\mathbf{S}$ has size $N_r \times N_t$ and is square if $N_r = N_t$, as is the case with TEMTADS. This allows us to diagonalize the matrix but does not suffice to guarantee that the extracted information is useful—i.e., that the eigenvalues and eigenvectors are real, and that the latter are orthonormal. For that to hold we must have a real, symmetric matrix, which requires $\mathbf{G}_l^{\mathrm{sc}} = \mathbf{G}_l^{\mathrm{pr}} \equiv \mathbf{G}_l$. This cannot be rigorously true, because the receivers cannot coincide exactly with the transmitters, but holds approximately for TEMTADS if we factor the exciting current and the coil areas out of $\mathbf{S}$, as we did in equation (49). The diagonalization we perform is thus a particular case of a singular value decomposition (SVD), and in what follows we use "diagonalization" as shorthand for "SVD of a symmetric matrix."

The decomposition (51) exhibits the actual polarizability elements but is not directly available to us because the Green tensors are not orthogonal. To see what we do get when we diagonalize $\mathbf{S}$ we can perform the SVD on $\mathbf{G}$:

$$\mathbf{S} = \mathbf{G}\mathbf{U}\dot{\mathbf{\Lambda}}\mathbf{U}^T\mathbf{G}^T = \mathbf{W}\left[\mathbf{\Sigma}\mathbf{V}^T\mathbf{U}\dot{\mathbf{\Lambda}}\mathbf{U}^T\mathbf{V}\mathbf{\Sigma}\right]\mathbf{W}^T = \mathbf{W}\mathbf{Z}\mathbf{\Delta}\mathbf{Z}^T\mathbf{W}^T = \mathbf{Y}\mathbf{\Delta}\mathbf{Y}^T$$

(52)

In the intermediate step we have used the fact that the matrix within the brackets is real and symmetric and thus has a purely real eigendecomposition. Result (52) shows that the eigenvalue matrix $\mathbf{\Delta}$, though time-dependent, is not solely composed of source responses, but also contains location and orientation information extracted from the Green tensors. The eigenvectors, likewise, include information from both the polarizabilities and the measurement particulars.

We also see in the decomposition (52) that $\mathbf{S}$ contains an unknown "hidden dimension"— $3N$, where N is the number of sources—in the size of the block-diagonal response matrix. Numerical diagonalization (or, in general, the SVD) of $\mathbf{S}$ will impose this middle dimension to be $N_r = N_t$. Ideally, the method should be able to resolve up to $\lfloor N_r / 3 \rfloor$ responding sources, or eight for TEMTADS, but the actual number is lower. For one, the procedure will resolve targets only when they are spatially separated: two distinct dipoles sharing one location decrease the rank of the $\mathbf{G}$ matrices, and hence of $\mathbf{S}$, by 3. In any case, diagonalization of $\mathbf{S}$ can again let us estimate the number of targets illuminated by the sensor; since the only time-dependent quantities are the intrinsic polarizabilities of the

sources, we expect the additional information provided by the time decay of the eigenvalues to be useful for classification.

The development outlined above corresponds to each time gate taken separately. To make sense of the time-dependent information we have to find a way to "follow" each of the eigenvalues as the signal decays. (A similar process must be carried out when using the dipole model for inversion.) One could in principle diagonalize the MSR matrix at each time channel, and the eigenvectors, which depend only on geometry and pose, should stay constant; however, it is not possible to know a priori the order in which the eigenvalues will be given by the diagonalization; this fact—not to mention noise and experimental uncertainty—makes it inevitable to have to disentangle the tensor elements by hand, which is easily done wrong. Instead, we explicitly look for an orthogonal matrix of eigenvectors that diagonalizes all the MSR matrices simultaneously. The procedure we employ is a generalization of the method for single matrices, and is well-known; it is sketched in next Section.

Chapter 2. Inverse Problems

2.1   Introduction

Several EMI sensing and data-processing techniques [2-5, 60,64,65] have been recently developed for detecting and discriminating between UXO and non-UXO items. Typically the first step of these methods is the recovery of a set of parameters that specify a physics-based model representing the object under interrogation. For example, in EMI sensing, the recovered parameters consist of the object's location and spatial orientation in addition to "intrinsic" parameters such as the polarizability tensor (along with some parameterization of its time-decay curve) in dipole models or the amplitudes of responding magnetic sources in the NSMS and ONVMS models. EMI responses depend nonlinearly on the subsurface object's location and orientation, therefore determining the buried object's orientation and location is a non-linear problem. In this section several inverse scattering approaches are described for EMI data inversion.

Most EMI sensors are composed of separate transmitting and receiving coils. When the operator activates the sensor, a current runs through the transmitter coils, resulting in the establishment of a ("primary" or "principal") magnetic field in the surrounding space. By Faraday's law, this time-varying magnetic field induces eddy currents in highly conducting bodies (ferromagnetic bodies also have their magnetization affected by the impinging field). These currents and magnetization in turn generate a ("secondary" or "scattered") magnetic field that also varies with time and induces measurable currents in the receiving coils. At the end, the electromagnetic data are inverted using different forward models. The procedure for estimating the location, orientation, and electromagnetic parameters of a buried object (linked in a "model vector" $\mathbf{v}$) is carried out by defining an objective function that quantifies the goodness-of-fit between the measured data and the predictions of the forward model. Routinely, a least-squares (LS) approach is taken to recover $\mathbf{v}$: formally, if $\mathbf{d}^{\text{obs}}$ is the vector of the measured scattered field and $\mathbf{F}(\mathbf{v})$ is the solution to the forward problem, the least-squares criterion assumes the form

$$\text{minimize } \phi(\mathbf{v}) = \left\| \mathbf{d}^{\text{obs}} - \mathbf{F}(\mathbf{v}) \right\|^2$$

(53)

A simple way to determine the model vector $\mathbf{v}$ is to use the Gauss-Newton method, which starts with an initial guess $\mathbf{v}_0$ and updates it iteratively through

$$\mathbf{v}_{k+1} = \mathbf{v}_k + \mathbf{s}_k \quad (54)$$

where k denotes the iteration number and $\mathbf{s}_k$ is a perturbation direction; we solve for the $\mathbf{s}_k$ that minimizes ϕ. In many cases the LS approaches suffer from an abundance of local minima that often leads them to make incorrect predictions of location and orientation. Global search procedures, such as differential evolution (DE) [97,98] and genetic

algorithms[37], have been recently developed to avoid this problem. We have combined the DE algorithm with the NSMS model [3] (or with the dipole model [37]) to recover locations and orientations of buried objects. Once these extrinsic properties are found we perform classification using Mixed Models (MM) and standard Matlab built-in classifiers based on maxmum likelihood methods or on linear, quadratic, or Mahalanobis distances. Both gradient and global search approaches are computationally intensive because they require a massive number of forward-model evaluations and because the determination of the nonlinear elements of $\mathbf{v}$—the location and orientation of the object—is a nontrivial and time-consuming problem in itself. To avoid non-linear, time-consuming inversions, and by so doing streamline the inversion process, we recently developed a new physics-based approach called the HAP method and applied it to various UXO discrimination problems. The HAP method exploits an analytic relationship between the magnetic field vector $\mathbf{H}$, the vector potential $\mathbf{A}$, and the scalar magnetic potential ψ (Psi) of a hypothetical point dipole to determine the location of a visually obscured object. Of these quantities only the magnetic field (and often only one of its components) is available, and as part of this project we developed a numerical procedure based on the 2D NSMS model that replaces the measurement surface around the scatterer with a flat plane of dipoles at a (known) location intermediate between the instrument and the target. The amplitudes of these responding sources can be computed starting from high-spatial-coverage geophysical data by solving a linear system of equations and can then be used to reconstruct $\mathbf{H}$, $\mathbf{A}$, and ψ at any point on or above the measurement surface and thus to solve for the relative location $\mathbf{R}$ and the polarizability $\bar{\bar{\mathbf{M}}}$ of the hypothetical dipole.

This chapter briefly overviews gradient-based optimization, differential evolution, and the HAP method [6].

2.2   Gradient-based methods of optimization

One of the most popular approaches for solving inverse problems is the gradient method [39-41, 100, 101]. The gradient method requires the system's Jacobian, which contains the gradients of the scattered field with respect to the unknown parameters of interest. In many cases it is impossible to determine the scattered EM field's derivatives analytically; this, however, is not a problem with either the dipole model or the NSMS model. Further, the NSMS-based inverse approach always results in an over-determined system and thus does not suffer from the ill-conditioning that usually afflicts finite-element or finite-difference time-domain methods. The EM scattering problem can be written in compact matrix form as:

$$[Z]\{\Omega\} = \{H^d\} \quad (55)$$

where $[Z]$ is the scattering matrix, $\{\Omega\}$ is a vector containing the amplitudes of responding dipoles (normalized by the primary field), and $\{H^d\}$ is a vector containing the measured data over a set of points. The important point to note is that $[Z]$ in the NSMS contains explicit expressions for the responding source amplitudes $\{\Omega\}$ in terms of the object's

location and orientation that can be differentiated analytically and that contain no singularities in the regions where they must be evaluated. Let us assume that α is a set of parameters (orientation, depth, etc.) that must be determined from a set of measured data [42]. A convenient way to view the problem is to define a forward map as one that associates a given α with an initial value α_0 (which serves to kick-start the inversion process). A least-squares formulation of the problem identifies a minimum of the error function by solution of the equation

$$\left[\frac{\partial H^{\text{mod}}}{\partial \alpha}\right]_{\alpha_{\beta-1}} \{\delta\alpha_\beta\} = \left[J\right]_{\alpha_{\beta-1}} \{\delta\alpha_\beta\} = \min\left(\{H^{\text{meas}}\} - \{H^{\text{mod}}(\{\alpha_{\beta-1}\})\}\right) ,$$ (55)

where $[J]_{\alpha-1}$ is a Jacobian matrix based on $\{\alpha_{\beta-1}\}$, β is the iteration number, the modeled values $\{H^{\text{mod}}\{\alpha_{\beta-1}\}\}$ are predicted based on $\{\alpha_{\beta-1}\}$, and the solution $\{\delta\alpha_\beta\}$ is a vector of incremental steps in the unknown parameters, which are updated via

$$\{\alpha_\beta\} = \{\alpha_{\beta-1}\} + \{\delta\alpha_\beta\}$$ (56)

2.3   Differential evolution

Differential evolution (DE) [3, 3, 97,98], one of the global-search algorithms recently developed to bypass the local-minima problem that often leads standard gradient-search approaches to make incorrect predictions for location and orientation, is a heuristic, parallel, direct-search method for minimizing nonlinear functions of continuous variables. Similar in concept to the genetic algorithms that have been used with much success on problems with discrete variables, DE is easy to implement and has good convergence properties.

We have combined the DE algorithm with the above-discussed dipole, NSMS, and ONVMS techniques to invert digital geophysical EMI data following a procedure reminiscent of the stepwise optimization described in the previous section. The scattered field from any object whose location and orientation are known depends linearly on the magnitudes of its responding sources, and the procedure starts by giving initial values of the attitude parameters and using these estimates, along with the measured data, to determine the source amplitudes by solving a linear system of equations. The amplitudes thus found are fed into a nonlinear objective function that quantifies the mismatch between measured data and model predictions and whose (DE-determined) minimum serves to refine the estimates for location and orientation. The procedure continues to alternate between these linear and nonlinear stages until it reaches convergence (or a preset maximum number of iterations). The responding amplitudes are then stored and used in a later classification step, while the location and orientation parameters are used during target excavation.

Differential evolution uses N_p-dimensional parameter vectors **v**,

$$\mathbf{v}_{p,G}, \ p = 1, 2, \ ..., \ N_p \tag{57}$$

where G is a generation/iteration index. In our case $\mathbf{v} = \{x_0, y_0, z_0, \theta, \phi\}$; the first three are the object's location and the other two are the polar (θ) and azimuthal (ϕ) Euler angles that define its orientation (by using only two angles we are assuming that UXO are effectively BOR). The objective function to be minimized is defined as

$$F(\mathbf{v}) = \frac{1}{(MN_f)^2} \sum_{m=1}^{M} \sum_{f=1}^{N_f} |H_{m,f}^{\text{sc}}(\mathbf{v}) - H_{m,f}^{\text{data}}(\mathbf{v})|^2 \tag{58}$$

where $H_{m,f}^{\text{sc}}(\mathbf{v})$ and $H_{m,f}^{\text{data}}$ are respectively the theoretical prediction (for vector $\mathbf{v}$) and the measured magnetic field data at the m-th measurement point (of M) and the f-th frequency or time point (of N_f). The DE optimization process itself can be subdivided into three steps:

1) The first step creates random initial populations $\mathbf{v}_{p,G}, \ p = 1, 2, \ ..., \ N_p$, that span the entire parameter space. For a given $\mathbf{v}_{p,G}$ in the generation, a linear system of equations is constructed by matching measured data to the secondary magnetic field . This system is linear in Ω_i and is solved directly for those parameters.

2) The second step, which requires the most execution time, is the calculation of the secondary magnetic field each of the $\mathbf{v}_{p,G}$. When the NSMS (or ONVMS) model is used, the calculation for each $\mathbf{v}_{p,G}$ requires a fraction of the time required to execute any other proposed 3D forward model; this relative computational efficiency makes NSMS (or ONVMS) an attractive alternative for performing real-time inversion.

3) Next comes the evaluation of the cost function for each population member and the storage of the best sets of parameters. At each step, the DE algorithm produces an estimate of position and orientation. By examining and sorting the cost function at each step, the best-half of the population is chosen as the next generation's parameters, whereas the bottom half is discarded. Thereafter the next generation is created by taking the parameters in the previous generation and applying crossover and mutation operations on them. The three steps are repeated until the maximum number of generations has been reached or until the objective function reaches a desired value. Rules for using DE are discussed in more detail elsewhere [97,98].
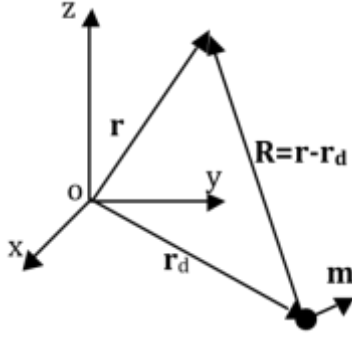
Figure 2.1: The HAP approach for a dipole.

2.4   The HAP method

2.4.1   Estimating the location and orientation of buried objects

In the EMI regime, the secondary magnetic fields measured by the EMI receivers are induced by eddy currents magnetic dipoles which are distributed non-uniformly inside the scatterer. There are some particular points, named "scattered field singularities" (SFS), where most of these sources are concentrated. Recent studies show that under certain conditions the entire scatterer can be replaced with several responding elementary sources by putting them at SFS points [85, 87, 102]. The mathematical and physical properties of SFS and its applications to EM scattering problems are very well documented, and their study is known in the literature as "*Catastrophe Theory*" [102-103]. Our objective has been to determine the locations of the SFS from data without solving traditional ill-posed inverse-scattering problems. We have found a new analytic expression for estimating the location, orientation, and polarizability elements of a buried object starting from measured EMI data. The algorithm (dubbed "HAP" [6]) is based on the fact that a target's response can be approximated by dipole sources concentrated at SFS points. It utilizes three global values at a single location in space: (1) the magnetic field vector $\mathbf{H}$, (2) the vector potential $\mathbf{A}$, and (3) the scalar magnetic potential ψ. Since among these quantities only the $\mathbf{H}$ field (and sometimes only one of its components) is measurable, we employ a variation of the NSMS model to obtain $\mathbf{A}$ and ψ we distribute elementary sources on an auxiliary planar layer, located between the sensor and the object, and find their amplitudes by fitting measured data.

The magnetic field $\mathbf{H}$ and the scalar (ψ) and vector ($\mathbf{A}$) potentials of a magnetic dipole are

$$\mathbf{H} = \frac{e^{jkR}}{4\pi R^3}\left[\left(\frac{3\mathbf{R}(\mathbf{R}\cdot\mathbf{m})}{R^2} - \mathbf{m}\right)\left(1 - jkR\right) - k^2\left(\mathbf{R}\times(\mathbf{R}\times\mathbf{m})\right)\right]$$

(59)

$$\psi = \frac{(\mathbf{R} \cdot \mathbf{m})}{4\pi R^3}\left(1 - jkR\right)e^{jkR},$$

(60)

$$\mathbf{A} = -\mu_0 \frac{\mathbf{m} \times \mathbf{R}}{4\pi R^3}\left(1 - jkR\right)e^{jkR} \equiv -\mu_0 \frac{\mathbf{m} \times \mathbf{R}}{R^3}G(R),$$

(61)

where $G(R) = \frac{e^{jkR}}{4\pi}(1 - jkR)$

where k is the wave number in the surrounding medium, $\mathbf{R} = \mathbf{r} - \mathbf{r}_d$, $\mathbf{r}$ is an observation point, and $\mathbf{r}_d$ is the location of the dipole [104] (**Error! Reference source not found.**). Note that the magnetic field (59) has terms that decay as R^{-1}, R^{-2}, and R^{-3}. The range $kR \gg 1$ is referred to as the far zone, and fields in this range are referred to as being in the far field. Similarly, fields in the near zone $kR \Box 1$ are referred to as being in the near field, and the zone $kR \approx 1$ is called intermediate zone. Typically, UXO detection and discrimination are conducted in the near zone. In addition, in the EMI regime displacement currents are considered irrelevant, which means that the contribution of the k^2 term in equation (59) can be set to zero. Making this assumption, taking the dot product of (59) with $\mathbf{R}$, and using (60) we get that

$$\mathbf{H} \cdot \mathbf{R} = \mathbf{H} \cdot (\mathbf{r} - \mathbf{r}_d) = \frac{1}{R^3}\left(\frac{3\mathbf{R}(\mathbf{R} \cdot \mathbf{m})}{R^2} - \mathbf{m}\right) \cdot \mathbf{R}\, G(R) = 2\frac{\mathbf{R} \cdot \mathbf{m}}{R^3}G(R) = 2\psi$$

(62)

Similarly, taking the cross product of (59) and $\mathbf{R}$ and using (61) we obtain

$$\mathbf{H} \times \mathbf{R} = G(R)\frac{1}{R^3}\left(\frac{3\mathbf{R}(\mathbf{R} \cdot \mathbf{m})}{R^2} - \mathbf{m}\right) \times \mathbf{R} = -G(R)\frac{\mathbf{m} \times \mathbf{R}}{R^3} = \frac{\mathbf{A}}{\mu_0}$$

(63)

Now, the cross product of $\mathbf{H}$ and (63) gives

$$\left[\mathbf{H} \times \frac{\mathbf{A}}{\mu_0}\right] = \mathbf{H} \times \left[\mathbf{H} \times \mathbf{R}\right] = \mathbf{H}\left(\mathbf{H} \cdot \mathbf{R}\right) - \mathbf{R}\left|\mathbf{H}\right|^2 = 2\mathbf{H}\,\psi - \mathbf{R}\left|\mathbf{H}\right|^2$$

(64)

which allows us to solve for $\mathbf{R}$:

$$\mathbf{R} = \frac{2\mathbf{H}\,\psi - \left[\mathbf{H} \times \mathbf{A}/\mu_0\right]}{\left|\mathbf{H}\right|^2}$$

(65)

The location $\mathbf{R}$ of the responding dipole is seen to be independent of the frequency. In other words, as long as MQS assumptions hold, equation (65) is valid when the dipole is in free space and equally well when it is embedded in a conducting medium such as seawater. Also note that $\mathbf{R}$ is determined as a ratio, which makes the expression (65)

partially tolerant to noise due to scaling arguments, since $\mathbf{A}$ and ψ are dependent on the $\mathbf{H}$ field (see equations (62) and (63)). Taking the cross product of $\mathbf{R}$ and (63) from the left side and using equation (62) we obtain an expression for the dipole moment $\mathbf{m}$:

$$\mathbf{m} = \frac{R}{G(\mathrm{R})}\left(\mathbf{R}\psi + \left[\mathbf{A}/\mu_o \times \mathbf{R}\right]\right)$$

(66)

with $\mathbf{R}$ previously determined from equation(65)

2.4.2   A simplified HAP method

It is possible to simplify the HAP method by eliminating the need for the vector potential. We rewrite equation (62) as

$$\mathbf{H}\cdot\mathbf{r}_d = -2\psi + \mathbf{H}\cdot\mathbf{r},$$

(67)

Which provides a least-squares estimate of $\mathbf{r}_d$ when evaluated at N distinct observation points:

$$\begin{bmatrix} H_x(\mathbf{r}_1) & H_y(\mathbf{r}_1) & H_z(\mathbf{r}_1) \\ H_x(\mathbf{r}_2) & H_y(\mathbf{r}_2) & H_z(\mathbf{r}_2) \\ & \vdots & \\ H_x(\mathbf{r}_N) & H_y(\mathbf{r}_N) & H_z(\mathbf{r}_N) \end{bmatrix} \begin{bmatrix} x_d \\ y_d \\ z_d \end{bmatrix} = \begin{bmatrix} -2\psi(\mathbf{r}_1) + \mathbf{H}(\mathbf{r}_1)\cdot\mathbf{r}_1 \\ -2\psi(\mathbf{r}_2) + \mathbf{H}(\mathbf{r}_2)\cdot\mathbf{r}_2 \\ \mathsf{M} \\ -2\psi(\mathbf{r}_N) + \mathbf{H}(\mathbf{r}_N)\cdot\mathbf{r}_N \end{bmatrix}.$$

(68)

2.4.3   Determining the HAP amplitudes

To construct the potentials (and the other field components, if unavailable) we assume that the field is produced by a surface distribution of magnetic charge $q(s')$ spread on a fictitious plane located just below the ground (**Error! Reference source not found.**). The positions $\mathbf{r}_{s'}$ of the sources are fixed and known by construction, and the field can be expressed as the matrix-vector product

$$H_z(\mathbf{r}) = \int \frac{q(s')}{4\pi} \frac{z - z_{s'}}{|\mathbf{r} - \mathbf{r}_{s'}|^3} ds' \equiv \ddot{\mathbf{Z}}_z \cdot \mathbf{q}$$

(69)

by employing a quadrature scheme. To determine the array q of charges we minimize the difference between model predictions and collected data $\mathbf{H}^{\mathrm{meas}}$ at a set of known points:

$$\mathbf{q} = \arg\min \tfrac{1}{2}\left(\ddot{\mathbf{Z}}_z \cdot \mathbf{q} - \mathbf{H}_z^{\mathrm{meas}}\right)^2 = \left[\ddot{\mathbf{Z}}_z^{\mathrm{T}} \cdot \ddot{\mathbf{Z}}_z\right]^{-1}\left[\ddot{\mathbf{Z}}_z^{\mathrm{T}} \cdot \mathbf{H}_z^{\mathrm{meas}}\right],$$

(70)

where each matrix row corresponds to a different measurement point and each column to a subsurface of the underground virtual source layer. The potential is then found from

$$\psi(\mathbf{r}) = \int \frac{q(s')}{4\pi|\mathbf{r} - \mathbf{r}_{s'}|} ds' \equiv \ddot{\mathbf{Z}}_{\psi} \cdot \mathbf{q}.$$

(71)

Current EMI sensors operate in both monostatic and multistatic modes. Monostatic sensors, such as the Geophex frequency-domain GEM-3 instrument [106] and the Geonics EM-61 and EM-63 time-domain instruments [70] have collocated transmitter and receiver coils, whereas multistatic sensors like the MPV time-domain instrument [19] and the Berkeley UXO Discriminator (BUD) [46] have multiple transmitters or multiple receiver coils or both. We have implemented numerical procedures to estimate the vector and scalar magnetic potentials starting from multi-static or mono-static EMI data. For bistatic data we determine the potentials as described above; for the monostatic case we normalize the amplitudes of the responding auxiliary sources by the primary magnetic field. The procedure is discussed in further detail in [6].

It is worth reiterating that the HAP method replaces the scatterer with a point dipole, and is thus based on a rather drastic simplification; yet it provides acceptable location estimates because the sources within the target that produce the scattered field tend to concentrate at a set of "scattered field singularities" [85, 87]. The locations of these singularities change at every measurement point, since the primary field of the sensor also changes; the HAP method takes these variations into count and outputs an average location as a result.
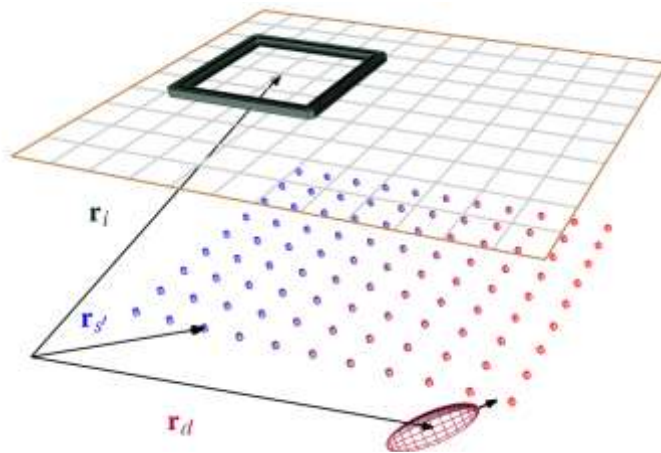

Figure 2.2: Determining the location and orientation of a buried target.

The method assumes the object is a point dipole and exploits an analytic relation between the field measured at $\mathbf{r}_i$ and the scalar potential at the same point to find the location $\mathbf{r}_d$.

The potential is constructed using a layer of equivalent magnetic sources placed between the sensor and the object; $\mathbf{r}_{s'}$ is a typical location on the layer.

2.4.4 The HAP method with gradient information

The HAP technique can be simplified further by reducing the formulation such that it only requires the magnetic field and its gradient, both of which are measurable by current sensors. After taking the gradient of equation (62) with respect to the x-, y-, and z-coordinates, we obtain

$$\begin{cases} x_d \dfrac{\partial H_x}{\partial x} + y_d \dfrac{\partial H_y}{\partial x} + z_d \dfrac{\partial H_z}{\partial x} = 3H_x + x\dfrac{\partial H_x}{\partial x} + y\dfrac{\partial H_y}{\partial x} + z\dfrac{\partial H_z}{\partial x} \\[2mm] x_d \dfrac{\partial H_x}{\partial y} + y_d \dfrac{\partial H_y}{\partial y} + z_d \dfrac{\partial H_z}{\partial y} = 3H_y + x\dfrac{\partial H_x}{\partial y} + y\dfrac{\partial H_y}{\partial y} + z\dfrac{\partial H_z}{\partial y} \\[2mm] x_d \dfrac{\partial H_x}{\partial z} + y_d \dfrac{\partial H_y}{\partial z} + z_d \dfrac{\partial H_z}{\partial z} = 3H_z + x\dfrac{\partial H_x}{\partial z} + y\dfrac{\partial H_y}{\partial z} + z\dfrac{\partial H_z}{\partial z} \end{cases}$$

.

(72)

Thus, in order to determine the target's location we need only the magnetic field $\mathbf{H}$ and its gradient at a given point in space.

Chapter 3. Next-generation sensors: modeling and validation

3.1 Introduction

A wide range of different electromagnetic induction sensing technologies, with novel waveforms, multi-axis transmitters, and scalar/vector receivers have been recently developed under SERDP-ESTCP programs. These advanced EMI sensors—including the MetalMapper, the TEMTADS array, the Berkeley UXO discriminator (BUD), and the man-portable vector (MPV) sensor—provide measurements that feature a combination of high spatial diversity, different viewpoints, and a very wide dynamic range and which do full justice to the vector character of the electromagnetic field. Current state-of-the-art EMI systems thus offer data of unprecedented richness for use by discrimination processing algorithms. We have adapted our advanced EMI models and data-interpretation and -processing schemes to all these innovative EMI systems in order to take advantage of the quality of the data they provide.

This chapter overviews these advanced EMI sensors, their geometries and sensing modalities, and the procedures we have in place to model the way they establish primary fields and measure subsurface responses. We validate our methods by making comparisons between measured and modeled data for single- and multi-target scenarios. We initially describe the MetalMapper, continue with TEMTADS and BUD, and finish with a look at the MPV.

3.2 MetalMapper

The MetalMapper (MM) is an advanced EMI system for UXO detection and discrimination developed primarily by G&G Sciences and commercialized by Geometrics. The system has three mutually orthogonal transmitter rectangular loops. It is able to illuminate a target with primary fields from three independent directions from a single spatial field point. The 1 m × 1 m Z transmitter loop is located at ground level. The Y transmitter loop, also 1 m × 1 m, is centered 56 cm above the Z loop, as is the 0.98 m × 0.98 m X transmitter (Figure 3.1). The targets are illuminated from different directions depending on the geometry between a particular transmitting loop and the target. The system has seven 10-cm-side receiver cubes placed at seven unique spatial points on the plane of the Z transmitter loop. The receivers measure the vector $d\mathbf{B}/dt$ at each of the seven points, thus providing 63 independent readings of the transient secondary magnetic field for each instrument location. The positions of the receiver cubes' centers with respect to the Z transmitter loop (whose center we consider as the local origin of coordinates for the system) are given in **Error! Reference source not found.**.

Figure 3.1: The MetalMapper during SLO site deployment (left) and its
schematic diagram (right).

Table 1.   MetalMapper receiver locations with respect to the center of the Z transmitter
loop

Rx #	X [cm]	Y [cm]	Z [cm]
0	39	39	5
1	–26	26	5
2	13	13	5
3	0	0	5
4	–13	–13	5
5	26	–26	5
6	–39	–39	5

The MM transmitters are modeled as infinitely thin rectangular wires. The primary
magnetic induction produced at any observation point $\mathbf{r}$ by the T-th loop is determined
simply from the Biot-Savart law,

$$\mathbf{B}_T(\mathbf{r}) = \frac{\mu_0}{4\pi} \sum_{i=1}^{N_{Tx}} \frac{I_T[\Delta\boldsymbol{\ell}_{T,i} \times \mathbf{R}_{T,i}]}{R_{T,i}^3}, \quad T = 1,2,3$$

,   (73)

where, $\mathbf{R}_{T,i} = |\mathbf{r} - \mathbf{r}'_{T,i}|$, $\mathbf{r}'_{T,i}$ is the location of the i-th current element, and $\Delta\boldsymbol{\ell}_{j,i}$ is the
tangential length vector for the i-th subsection of the loop. In what follows, and unless we
note otherwise, we divide each transmitter coil into $N_{Tx} = 40$ subsections whenever we
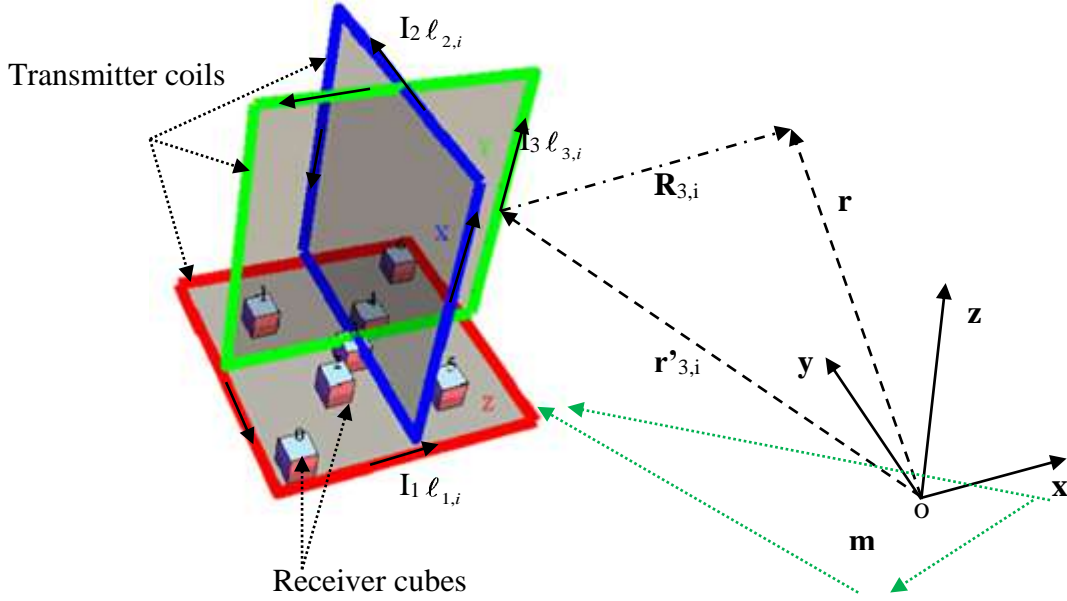calculate the primary magnetic induction using Eq. (73).

Figure 3.2: The Metal Mapper geometry.

The observation point $\mathbf{r}$ is defined with respect to the global Cartesian coordinate system XYZO; $\mathbf{r}'_{3,i}$ is the location of the i-th current element on (in this case) the $T = 3$ transmitter, which carries a current I_3 in the direction $\ell_{3,i}$.

The MM receiver assembly consists of seven cube sensors. Each of these measures along three orthogonal directions the induced voltages that, from Faraday's law, correspond to the negative of the time derivative of the secondary magnetic flux through the area spanned by the different coils. The induced voltage in the R-th sensor along the α-th direction, where $R = 0,\dots,6$ and $\alpha = z, y, x$, is computed using

$$V_R^\alpha = -\int_{S_R^\alpha} \frac{\partial \mathbf{B}}{\partial t} \cdot d\mathbf{s}_R^\alpha = \sum_{i=1}^{N_{Rx}} \frac{\partial \mathbf{B}_i(\mathbf{r}_{i,R}^\alpha - \mathbf{r}_o)}{\partial t} \cdot \hat{\mathbf{n}}_\alpha \, \Delta s_{i,R}^\alpha$$

(74)

where s_R^α is the area of the relevant coil (all of which are $10\,\text{cm} \times 10\,\text{cm}$ squares in MetalMapper) and $\hat{\mathbf{n}}_\alpha$ is the unit vector perpendicular to it, $\Delta s_{i,R}^\alpha$ and $\mathbf{r}_{i,R}^\alpha$ are respectively the i-th sub-area and vector location point on s_R^α, $\mathbf{B}_i(\mathbf{r}_{i,R}^\alpha) = \mu_o \mathbf{H}_i(\mathbf{r}_{i,R}^\alpha)$ is the magnetic induction (proportional to the magnetic field $\mathbf{H}_i(\mathbf{r}_{i,R}^\alpha)$) produced at $\mathbf{r}_{i,R}^\alpha$ by a source placed at $\mathbf{r}_o$. Within the ONVMS model, $\mathbf{H}_i(\mathbf{r}_{i,R}^\alpha)$ is calculated using equation (74). In what follows we always divide s_R^α into $N_{Rx} = 4$ sub-areas.
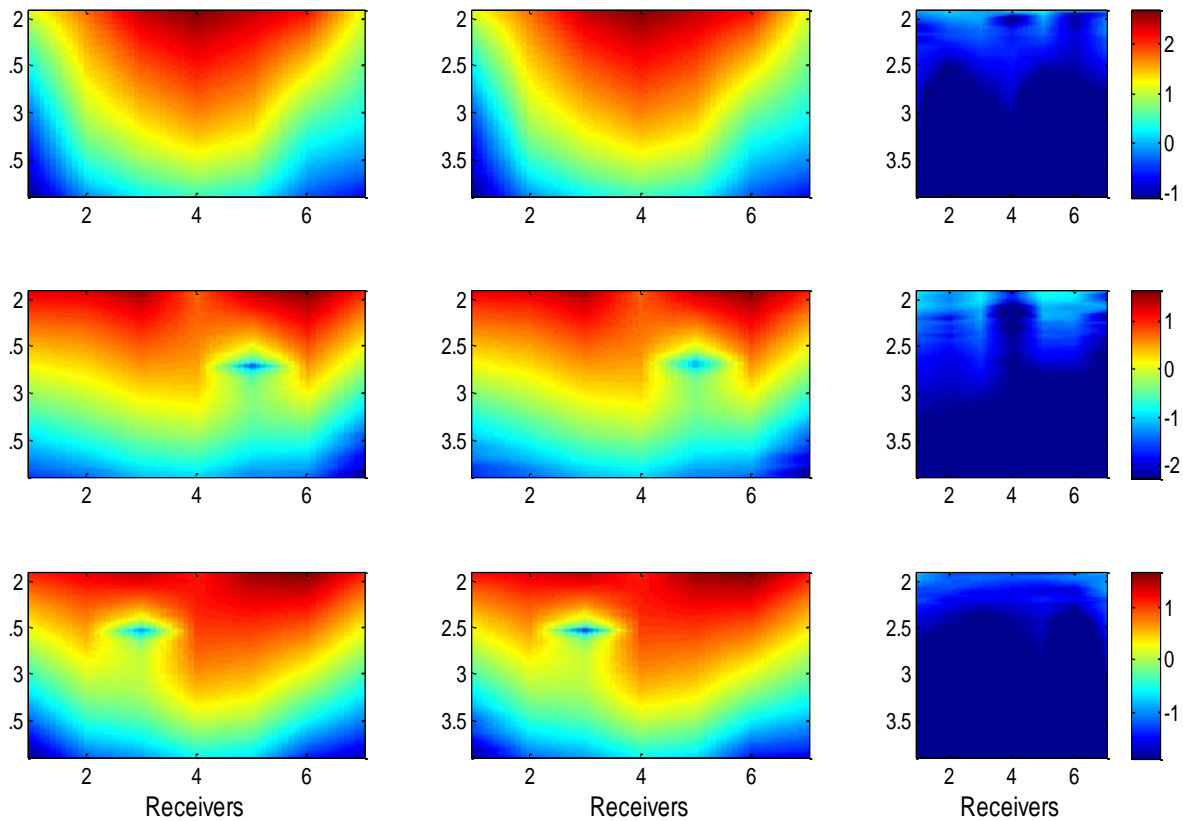
Figure 3.3: Response of an 81-mm mortar illuminated by the MM
Z-transmitter: measured (left), ONVMS prediction (center), and
mismatch between modeled and actual data (right). The mortar is
placed 35 cm below the sensor center and oriented 45 degrees
nose down. The data are plotted in log10 scale.

To validate the MetalMapper versions of our advanced EMI codes we conducted
comparisons between actual and measured data for different targets. Figure 3.4 through
Figure 3.6 compare measured and ONVMS-modeled data for an 81-mm mortar placed 35
cm below the sensor center, oriented 45 degrees nose-down and illuminated in turn by the
Z, Y, and X transmitters. We use three responding ONVMS sources whose locations are
determined with the combined ONVMS-DE algorithm. The inverted location matches the
actual target location very well. The model is seen to predict target EMI responses very
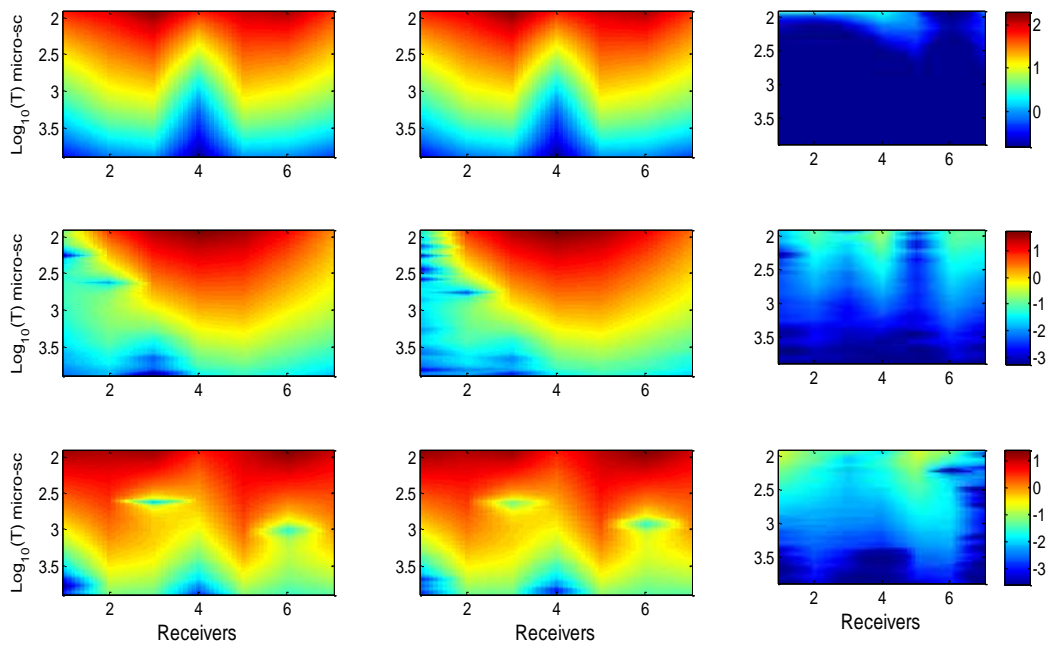accurately.

Figure 3.4: Response of an 81-mm mortar illuminated by the
MM Y-transmitter: measured (left), ONVMS prediction
(center), and mismatch between modeled and actual data (right).
The mortar is placed 35 cm below the sensor center and
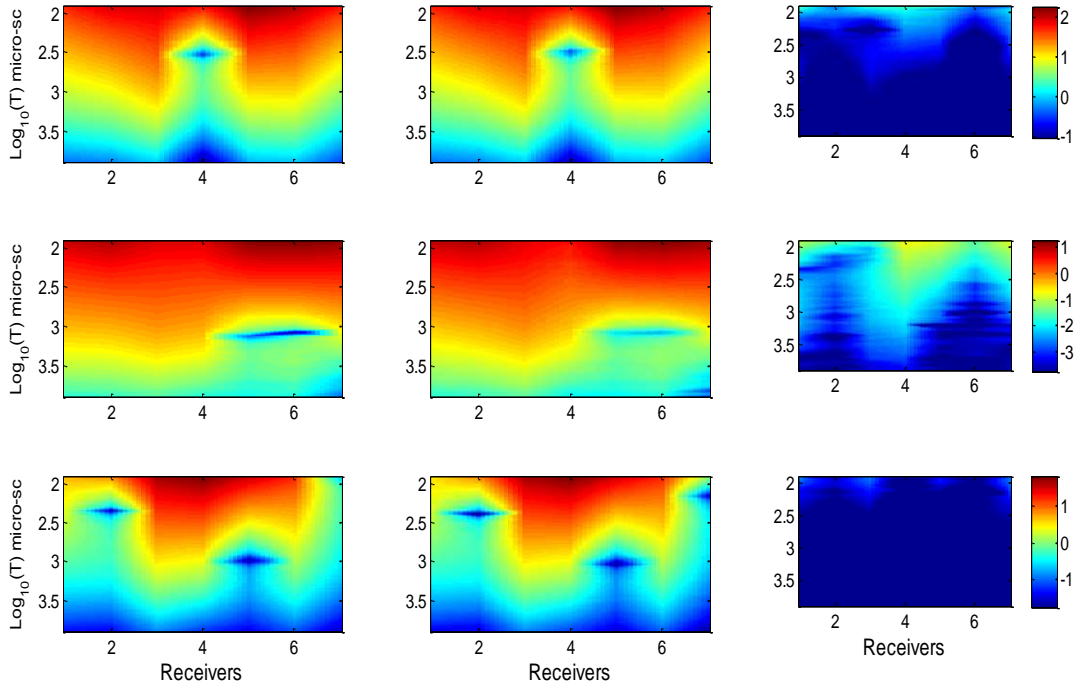oriented 45 degrees nose down. The data are plotted n log10
scale.

Figure 3.5: Response of an 81-mm mortar illuminated by the MM X-transmitter: measured (left), ONVMS prediction (center), and mismatch between modeled and actual data (right). The mortar is placed 35 cm below the sensor center and oriented 45 degrees nose down. The data are plotted in log10 scale.
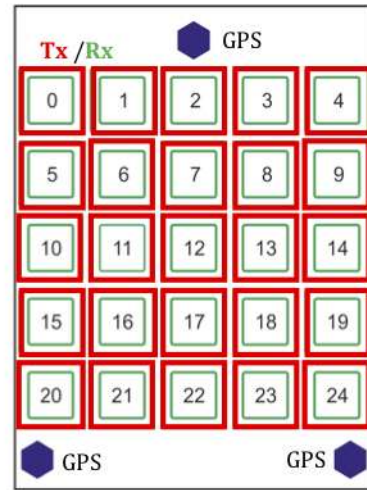
Figure 3.6: Photo of the TEMTADS in deployment at Blossom Point Test Site (left) and a schematic diagram of its Tx/Rx sensors (right).

3.3   TEMTADS

3.3.1   TEMTADS modeling

The NRL time-domain EMI sensor array TEMTADS is a next-generation system designed for subsurface target discrimination. The sensor consists of 25 transmit/receive pairs, each composed of a 35-cm square transmitter loop surrounding a 25-cm square receiver loop, arranged in a rectangular 5×5 grid with 40-cm neighbor-to-neighbor separation [56] (Figure 3.13). The sensor activates the transmitter loops in sequence, one at a time, and for each transmitter all receivers receive, measuring the complete transient response over a wide dynamic range of time going approximately from 100 microseconds (μs) to 25 milliseconds (ms) and distributed in 123 time gates. The sensor thus provides 625 spatial data points at each location, with unprecedented positional accuracy.

In modeling for TEMTADS, the transmitter loops are idealized as infinitesimally thin 35 cm $\times$ 35 cm square loops. The primary field produced at any observation point by a given transmitter loop is determined from equation (73). We use $N_{Tx} = 20$ for TEMTADS unless we note otherwise. The TEMATDS measured signal is modeled using equation (74), assuming $\alpha = z$ throughout and receiver sizes of 25 cm $\times$ 25 cm and dividing each receiver into $N_{Rx} = 9$ sub-areas. We compare actual and ONVMS modeled data for a 105-mm projectile in figure 13. and find very good agreement
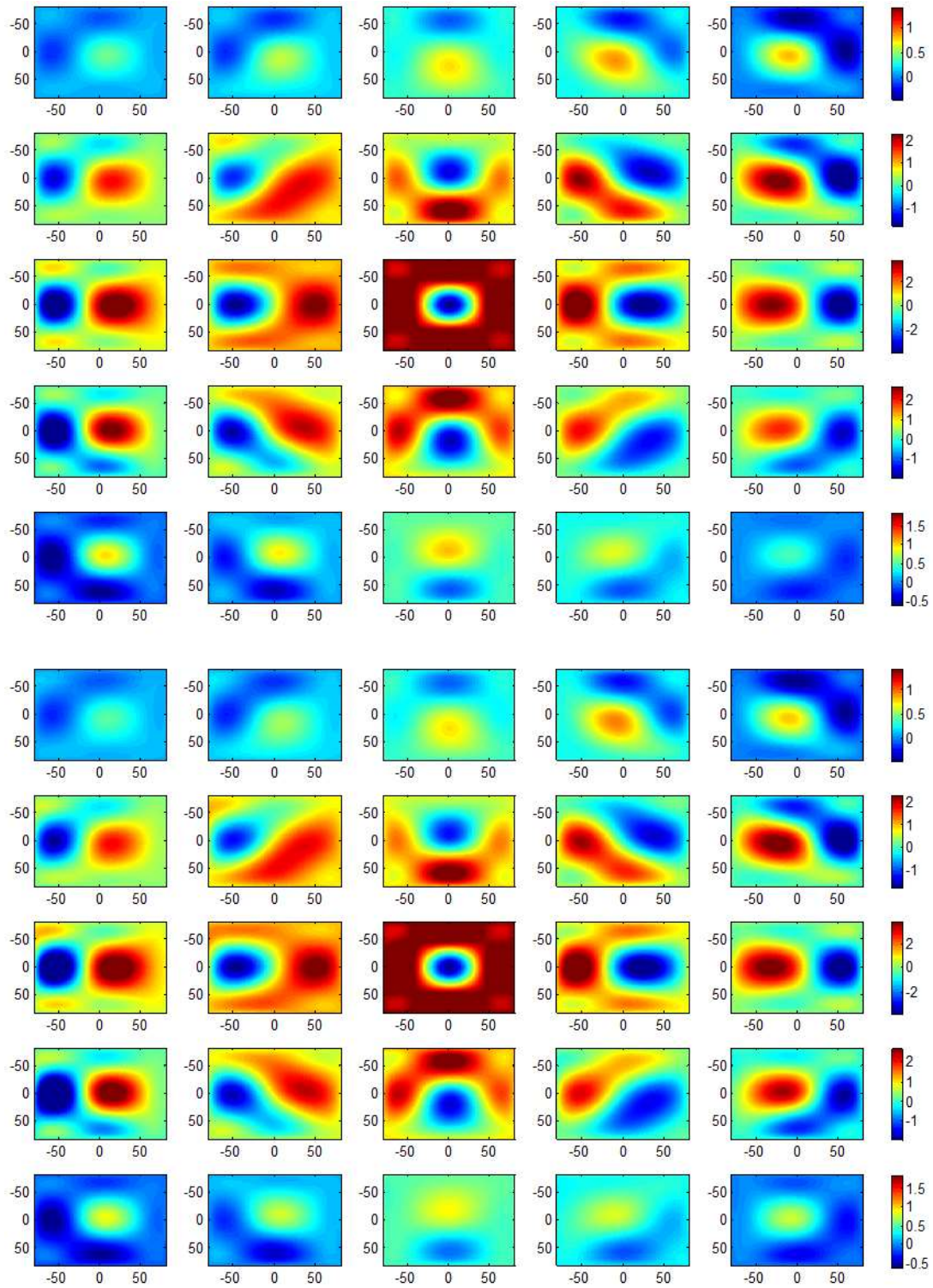
Figure 3.7: Measured (top five rows) and ONVMS-modeled

(bottom five) TEMTADS data for a 105-mm projectile at the

25th time channel. The target is buried at a depth of 30 cm and oriented horizontally relative to the TEMATDS system.

Figure 3.8: The APG TOI.

Table 2.   Inverted location and orientation for TEMTADS data

Case #	Ground truth /estimated for a 37 mm UXO				
1	Xo [m]	Yo [m]	Zo [m]	Azimuth [Degree]	Dip [Degree]
2	0.0/(0.03)	0.0/(0.02)	-0.35/(-0.39)	0/(3)	0/(5)
3	0.0/(0.013)	0.0/(0.007)	-0.34/(-0.369)	0/(3)	90/(88)
4	0.0/(0.001)	0.0/(0.02)	-0.38/(-0.41)	0/(5)	-90/(85)
5	0.0/(0.04)	0.0/(0.05)	-0.37/(-0.405)	0/(5)	45/(35)

a) APG test-site classification

To demonstrate the classification performance of the advanced EMI models we conducted discrimination studies at the APG test site. We applied a combined HAP/NSMS approach to TEMTADS data sets. The main objective of the study was to discriminate TOI from non-TOI targets and further to indicate the type and caliber of each TOI. The TOI at APG varied in size from 25 mm up to 155 mm and are depicted in Figure 3.8.

There were three types of data sets: 1) Test stand data set collected for 14 UXO items placed in air for different depths and orientations; 2) Calibration grid data sets collected

over the same targets and over some clutter items; 3) Blind grid data sets collected over 214 buried items. According to a preliminary data a Figure 3.8 analysis by ESTCP, soil responses were insignificant at this site, and they were thus subsequently neglected. The test-stand and calibration grid data sets were used to test data inversion and discrimination algorithms. Object depths were inverted for each grid using the HAP method. The results are tabulated in Figure 3.9. Since, TEMTADS half thickness is 5cm, the inverted depths were in very good agreement (between 1=(-4+5) and 2=(-3+5) cm) with the actual depths for test-stand UXO items.
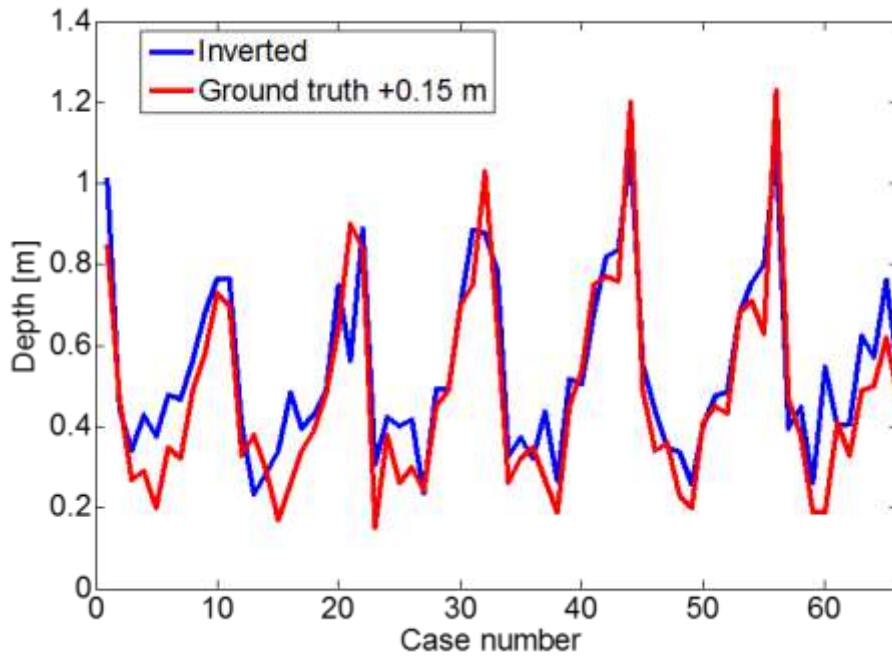

Figure 3.9: Comparison between the inverted and actual depth

for all 65 APG calibration targets.

We also used the HAP method to invert for the depths of all 65 calibration targets. The results are depicted in Figure 3.9. The inverted depth differed by up to 15 cm from the ground truth, a difference due to the fact that HAP estimates the distance from the sensor center to the target center, as was recorded for test-stand cases, while for calibration items the depths were measured from the ground surface. The sensor is 4″ (10.1 cm) above the ground and the transmitters are about 10 cm thick, and therefore the method provides reasonably accurate depth estimates.

Once we established that the HAP method estimates depths accurately for test-stand and calibration items we proceeded to estimate the total NSMS for all items and used it for discrimination. Figure 3.17 shows the inverted total NSMS as a function of time from test-stand TEMTADS data sets with the 105-mm projectile and the 81-mortar as targets. Each set of test-stand measurements comprised six different depths and target

orientations. The total NSMS is seen to be unique for all cases and, for both test-stand and calibration data. We then determined the best NSMS classification features. We fit the total M_{zz} NSMS curves with the Pasion-Oldenburg expression $M_{zz}(t) = kt^{-\beta}e^{-\gamma t}$, where t is time, and k, β and γ are the fitting parameters for each anomaly. We studied different combinations of $\ln k$, β, and γ using test-stand data. The results for β vs. $\ln k$ appear In Figure 3.11, and those for γ vs. $\ln k$ and γ vs. β appear in Figure 3.12 and Figure 3.13. We see that the best classification performance is achieved using $\ln k$ and β.
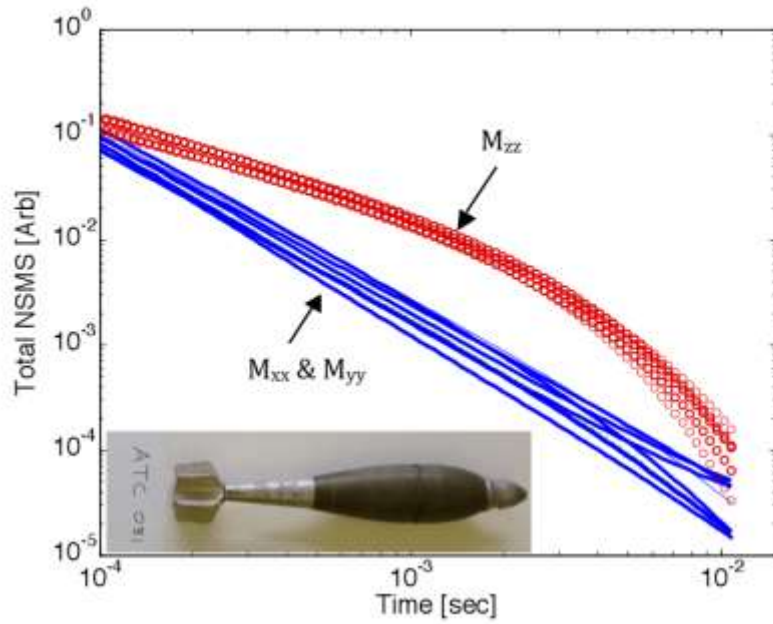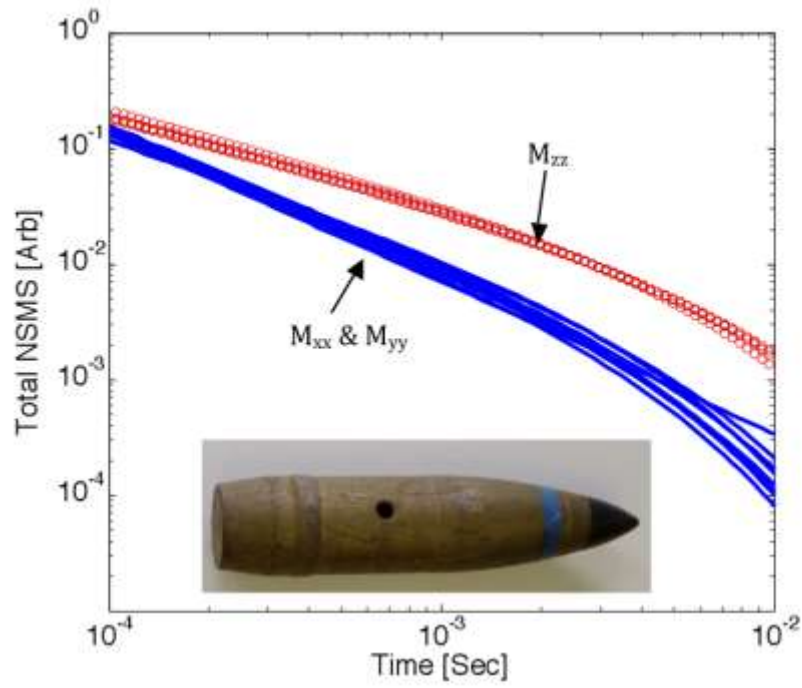
Figure 3.10: Inverted total NSMS for APG test-stand 105 mm projectile and 81 mm mortar.
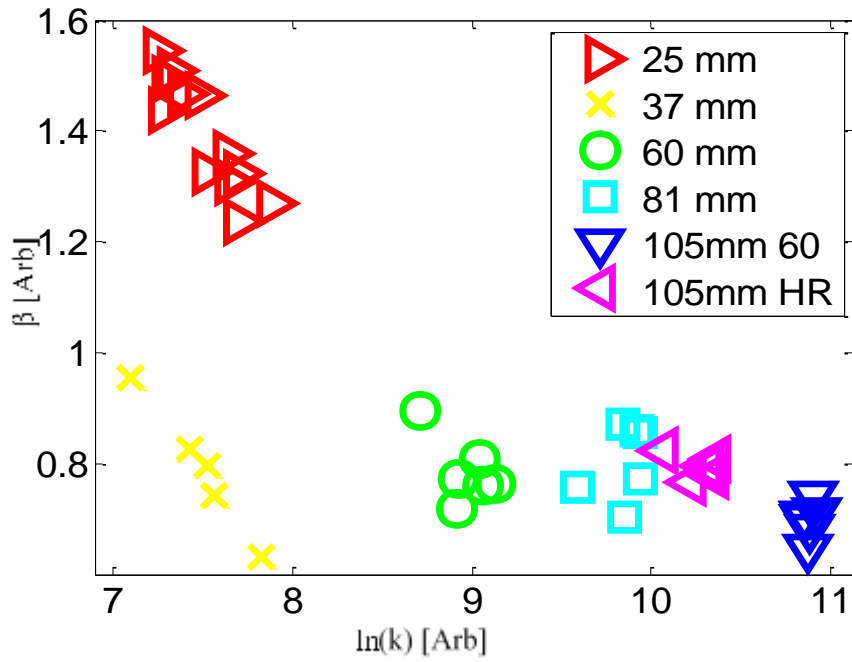
Figure 3.11: Scatter plot of inverted vs. classification features for APG test-stand TOI.
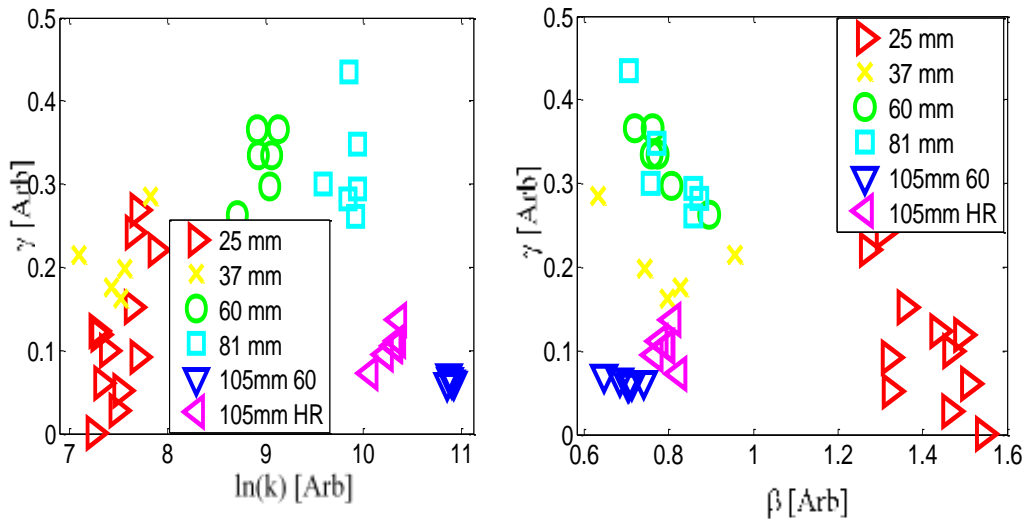

Figure 3.12: Scatter plot of inverted vs (left) and (right) parameters for APG test-stand TOI.
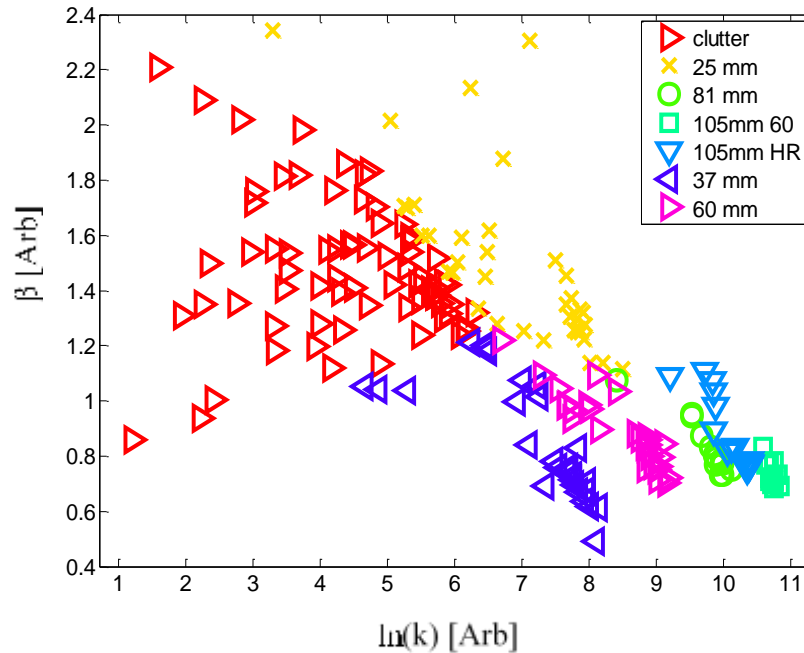
Figure 3.13: Scatter plot of inverted vs. classification features

for all 214 APG blind-test anomalies.

Finally, the described data inversion and classification schemes were applied to the 214 blind grid-data cells. These were also first inverted to determine the total NSMS, from which time-decay-history curves were synthesized, discrimination features were extracted, and classification was performed vis-à-vis test-stand UXO items. A scatter plot of in d classified $\ln k$ and β features for all 214 APG test anomalies is shown verted an in Figure 3.13. The result illustrates that the inverted features for 60-mm, 81-mm, and 105-mm TOI are clustered tightly, while those for 37-mm and 25-mm TOI s are scattered and mixed with those of clutter items. This complicates classification.

To overcome this problem, in addition classification/clustering approach, the entire time decay history of the total NSMS were also examined and compared to the total NSMS of the test-stand TOI case-by-case as a check on the classification. The comparisons are summarized in Figure 3.14 andFigure 3.15 .For all APG test anomalies a ranked list was created in which the anomalies were ranked as clutter or TOI and TOI were further ranked by caliber and type. This list was submitted to the Institute for Defense Analyses (IDA) for independent scoring. The scores showed that the advanced model was able to identify all UXO as TOI and classified all UXO correctly by type and caliber. The false-positive rate was 5%.
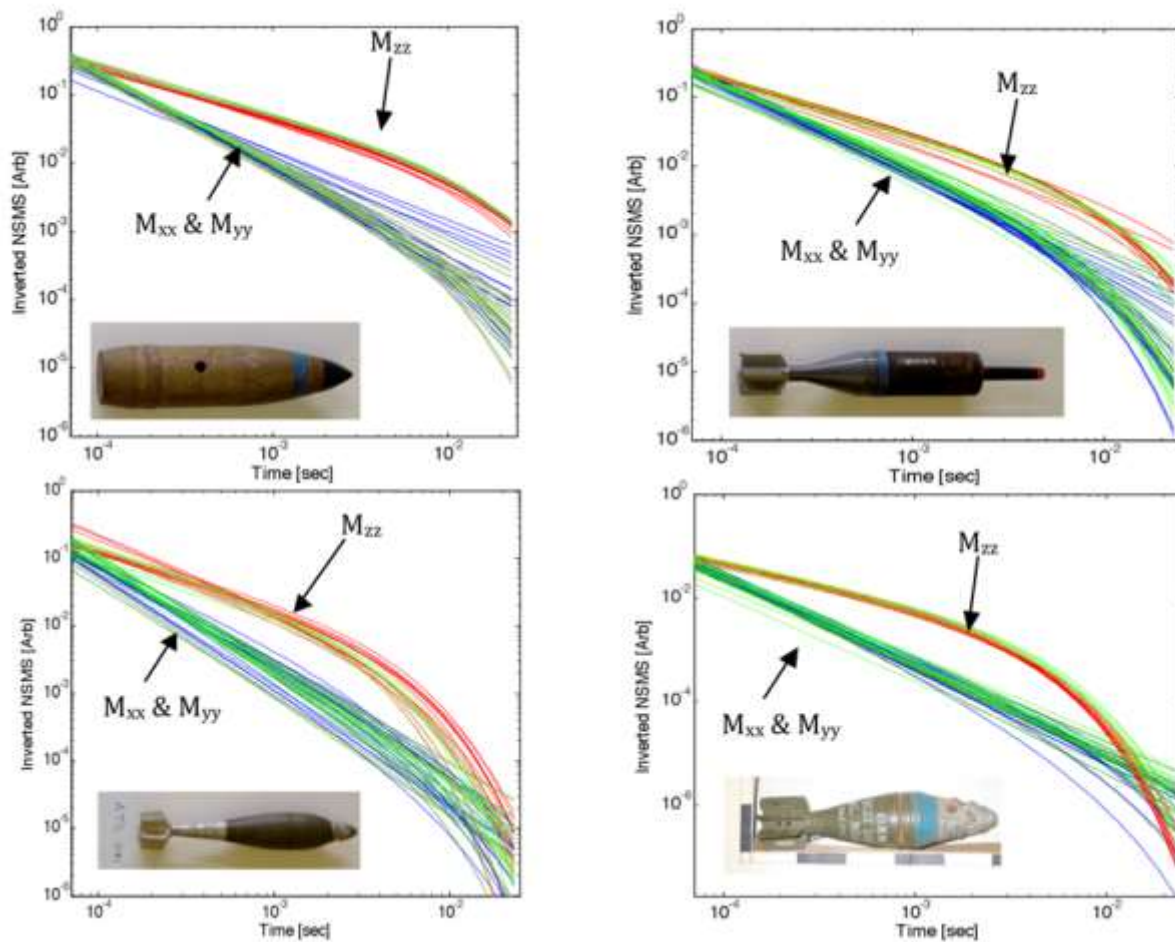
Figure 3.14: Comparison between library (green lines) and inverted (red and blue lines) blind-test total NSMS for 105 mm projectiles, 81-mm munitions, and 60-mm mortars.
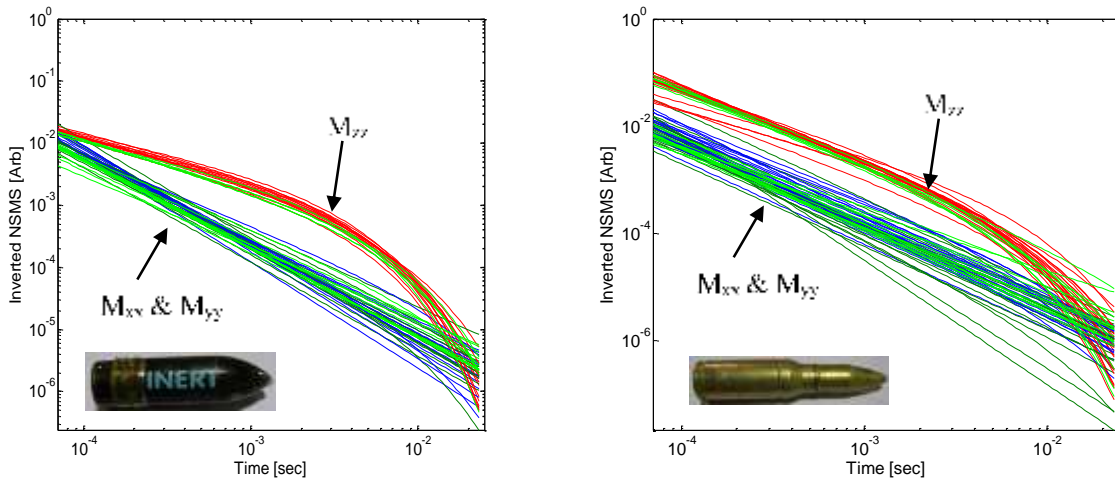
Figure 3.15: Comparisons between library (green lines) and inverted (red and blue lines) blind-test total NSMS for 37 mm and 25-mm mortars.
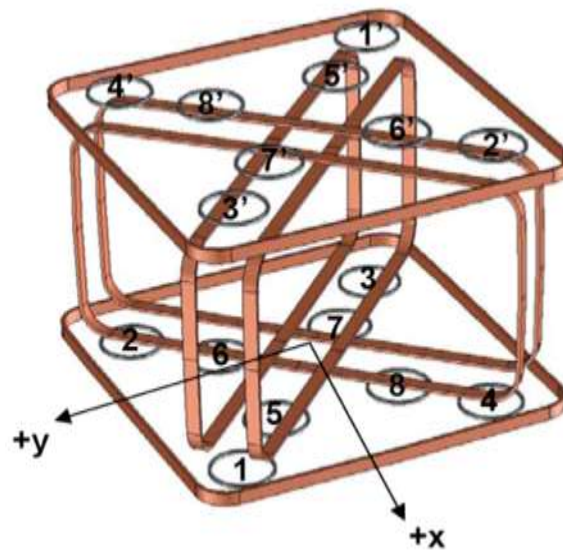
Figure 3.16: Schematic diagram of the BUD system.

b) BUD

The Berkeley UXO discriminator (BUD) is an advanced standalone time-domain system developed at the University of California to detect and discriminate UXO in the 20-mm to 155-mm size range, and consists of three orthogonal coil transmitters. The horizontal Z-coils are vertically separated by 26″ and have a 39″ × 39″ footprint. The Y- and X-vertical coils are mounted on the diagonals between the Z-coils (see Figure 3.16): the X-coils are 45.5″ × 23.5″ while the Y-coils are 45.5″ × 22.5″ in size, and both are separated

by 6″. The BUD illuminates targets in three independent directions, which induce eddy currents in all three modes. BUD has eight pairs of differenced receiver coils placed horizontally along the two diagonals of the upper and lower planes of the Z-transmitter loops. The pairs are located on symmetry lines trough the center and are wired in opposition so as to cancel the primary magnetic field during transmission Figure 3.23 shows the BUD system in operation.

The BUD transmitter loops were modeled as idealized infinitely thin square loops. The primary fields produced at any observation point by the transmitters are determined using a suitable modification of equation. (73), again with $N_{Tx} = 40$. The BUD measured signals are modeled using equation (74) as

$$V_R = -\sum_{i=1}^{N_{Rx}} \frac{\partial \mathbf{B}_i(\mathbf{r}_{i,R} - \mathbf{r}_0)}{\partial t} \cdot \Delta \mathbf{s}_{i,R} + \sum_{i=1}^{N_{Rx}} \frac{\partial \mathbf{B}_i(\mathbf{r}'_{i,R} - \mathbf{r}_0)}{\partial t} \cdot \Delta \mathbf{s}_{i,R}, \quad \Delta \mathbf{s}_{i,R} = \Delta s_{i,R} \hat{\mathbf{z}}$$

(75)

where $\mathbf{r}_{i,R}$ and $\mathbf{r}'_{i,R}$ are the locations of the Rx and Rx′ receivers, given in. For the case of BUD we divide the receivers into $N_{Rx} = 9$ sub-areas.

Figure 3.17: The BUD system in operation.

Table 3.   BUD receiver locations with respect to the origin.

Rx #	X [cm]	Y [cm]	Z [cm]	Rx' #	X' [cm]	Y' [cm]	Z' [cm]
1	35.48	35.48	0	1'	−35.48	−35.48	66

2	−35.48	35.48	0	2’	35.48	−35.48		66	
3	−35.48	−35.48		0	3’	35.48	−35.48		66
4	35.48	−35.48		0	4’	−35.48		35.48	66
5	19.29	19.29	0	5’	−19.29	−19.29		66	
6	−19.29	19.29	0	6’	19.29	−19.29		66	
7	−19.29	−19.29		0	7’	19.29	19.29	66	
8	19.29	−19.29		0	8’	−19.29	19.29	66	

All data presented here were collected by personnel from the Berkeley UXO team at Yuma Proving Ground in Arizona over objects at different orientations and depths. The response of each object was represented with only five NSMS. Figure 3.18, Figure 3.19, and Figure 3.20 show comparisons between modeled and actual data for all transmitters and receivers and for all time channels. The results clearly show that the NSMS very well predicts the EMI response of a M-75 mm UXO. Total NSMS amplitudes were determined for three samples each of M-75, 60-mm, and M-37 UXO and are depicted in Figure 3.21. The result demonstrates that the NSMS is applicable to the BUD system and is a good discriminator.

Figure 3.18: Comparisons between actual and predicted data for

an M75 UXO illuminated by the BUD Z transmitter. Solid lines

are actual data, circles stand for NSMS predictions.

Figure 3.19: Comparisons between actual and predicted data for an M75 UXO illuminated by the BUD X transmitter. Solid lines are actual data, circles stand for NSMS predictions.
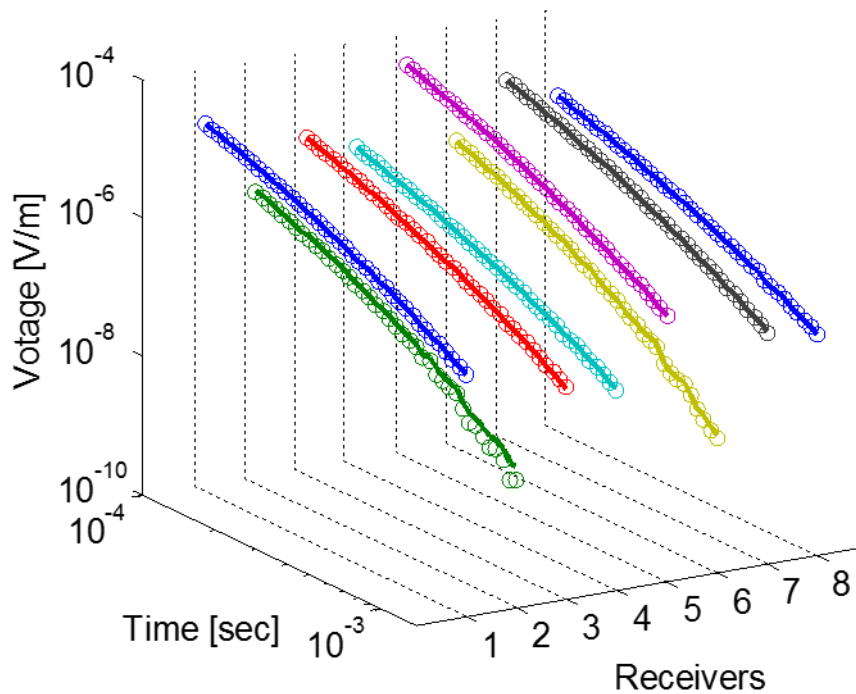
Figure 3.20: Comparisons between actual and predicted data for an M75 UXO illuminated by the BUD Y transmitter. Solid lines are actual data, circles stand for NSMS predictions.
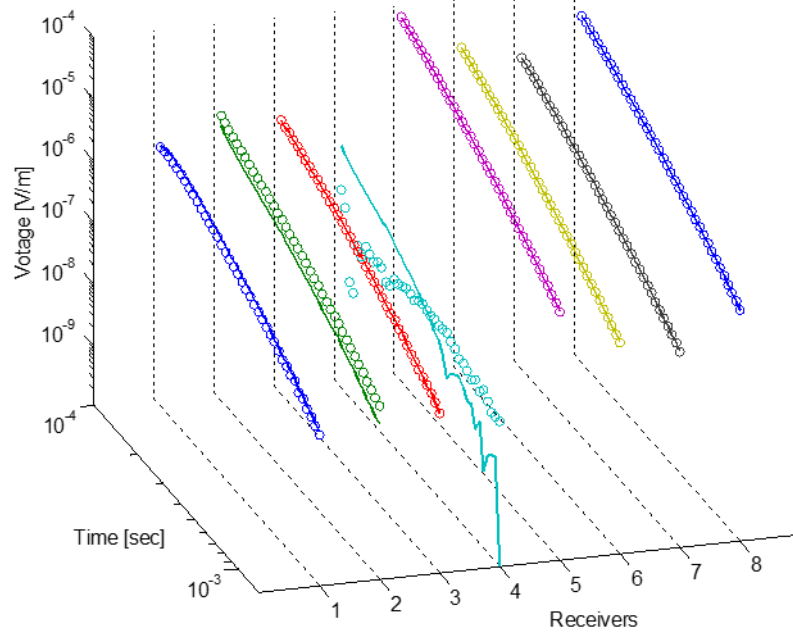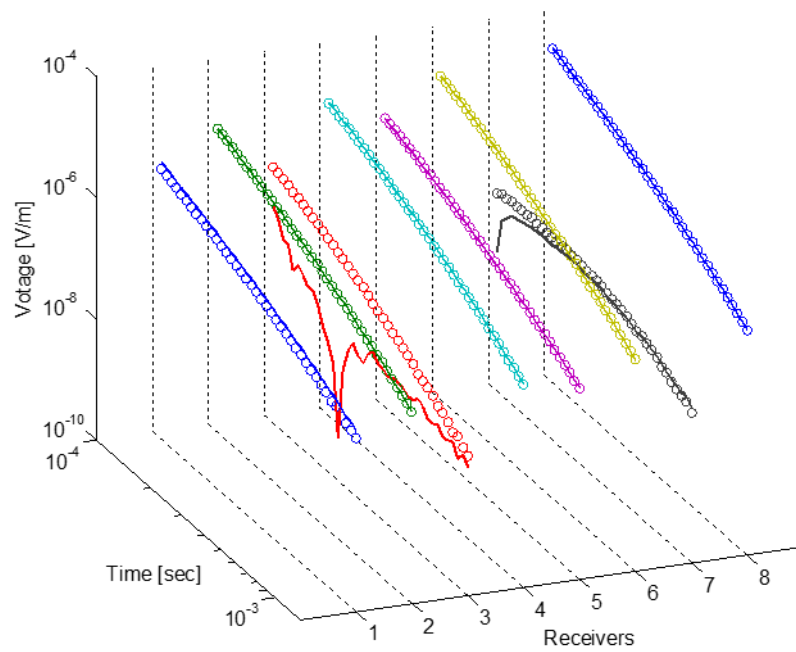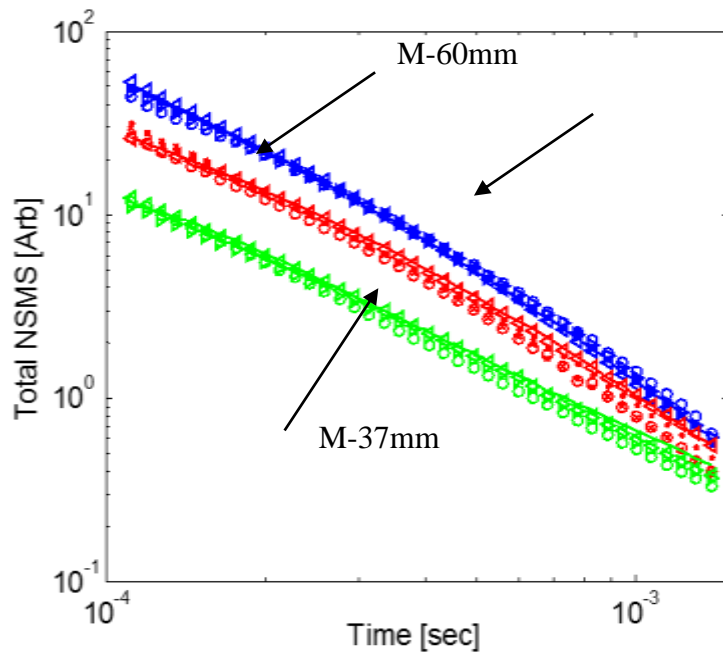
Figure 3.21. Recovered total NSMS from calibration BUD
measurements for M-75 (blue), 37-mm (green), and M 60 (red)
UXO.
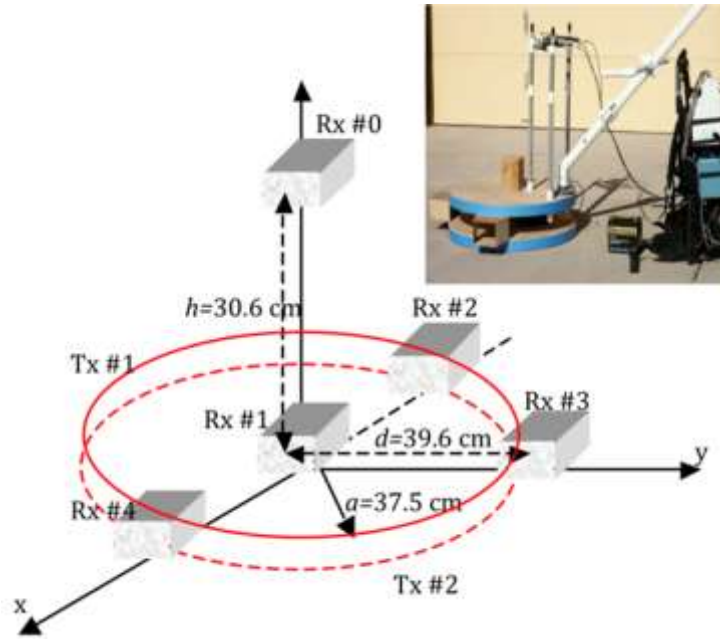
Figure 3.22: Photo and schematic diagram of the MPV sensor.

c) MPV

The MPV sensor, developed by G&G Sciences, Inc., consists of two transmitter loops and five triaxial receiver cubes. The receivers are located as follows: Cube #0 above center ($z = 30.6$ cm); Cube #1 at the origin; Cube #2 left of center ($x = -39.6$ cm); Cube #3 forward of center ($y = 39.6$ cm); and Cube #4 right of center ($x = 39.6$ cm). These receivers accurately measure the complete transient response over a wide dynamic range of time going from 100 μs to 25 ms. In numerical models we assume that the transmitter loops are idealized as infinitely thin circular loops with 37.5 cm radii, and separated by 12 cm. The complete primary field produced at any observation point by the transmitter loop is determined from equation (73) as

$$\mathbf{B}(\mathbf{r}) = \frac{\mu_0}{4\pi} \sum_{t=1}^{2} \sum_{i=1}^{N} \frac{I \Delta \ell_{t,i} \times \mathbf{R}_{t,i}}{R_{t,i}^3}$$

(76)

where, for the t-th transmitter loop, $t = 1, 2$, $\mathbf{R}_{t,i} = \left| \mathbf{r} - \mathbf{r}'_{t,i} \right|$, $\mathbf{r}'_{t,i}$ is the location of the i-th current element on t-transmitter, and $\Delta \ell_{t,i}$ is the tangential length vector for the i-th subsection. We use $N = 20$ unless we note otherwise. The MPV measured signal is

modeled using equation (74) with each loop having area 10×10 cm^2 and divided into 4 sub-areas.

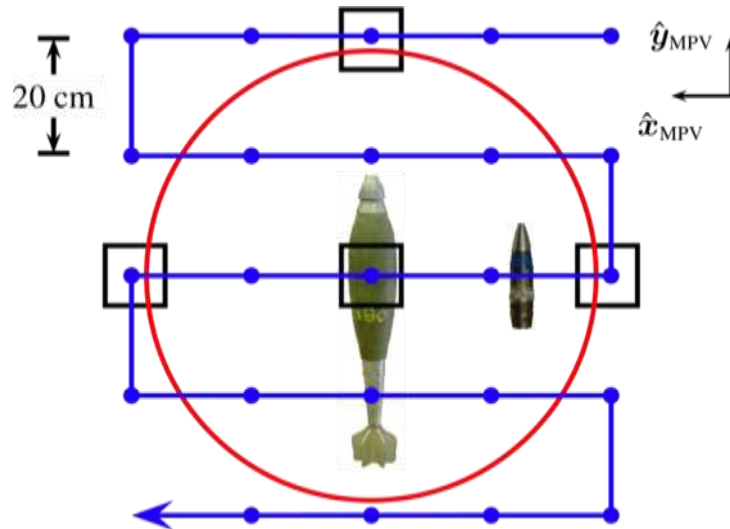Figure 3.23: Multi-object MPV data collection setup (right). The red circle corresponds to the MPV head, which was placed stationary; the targets were moved along the blue line. The center of the first target (the 81-mm) was placed at the blue points, and the distance between the first and second targets was kept fixed.

To illustrate the applicability of the ONVMS for MPV data we conducted studies in multi-target inversion and discrimination. The measurements reported here were conducted at the SKY Research office in Hanover, New Hampshire. The sensor was placed stationary, and data were collected for two objects with different separations and orientations placed on 5×5 grid points. The separation between the grids points was 20 cm. The targets were an 81-mm munition and a 40-mm round. The data were inverted using the simple dipole model with DE and the ortho-normalized volume magnetic source model (ONVMS). The number was assumed given in the simple dipole model, while in the ONVSMS four arbitrarily distributed interacting dipoles were used. The dipoles' positions were determined using DE. The inverted polarizability tensor principal elements for the projectiles are depicted in figure 30 for three different target-to-target separation vectors: (–25, 0, 0) cm (blue), (–40, 0, 0) cm (red), and (–25, 0, 25) (green). The single-dipole/DE algorithm accurately inverts the polarizability elements for the shallow 81-mm projectile but fails to identify the 40 mm projectile when the distance between the two is 25 cm (blue) and when the 40-mm is placed deeper (green). When the distance between the targets increases and they both have the same depth the algorithm identifies the 40-mm projectile correctly. The same data sets were inverted using the combined ONVMS-DE technique. The inverted locations showed the ONVMS dipoles

grouped around the locations of the projectiles, and for discrimination we summed the ONVMS amplitudes for each group. The results for the two targets, which appear in Figure 3.25, show that the inverted ONVMS is consistent for all cases and both munitions. The ONVMS technique is seen to be a robust algorithm for discriminating not only single well-isolated targets but also multi-target scenarios.
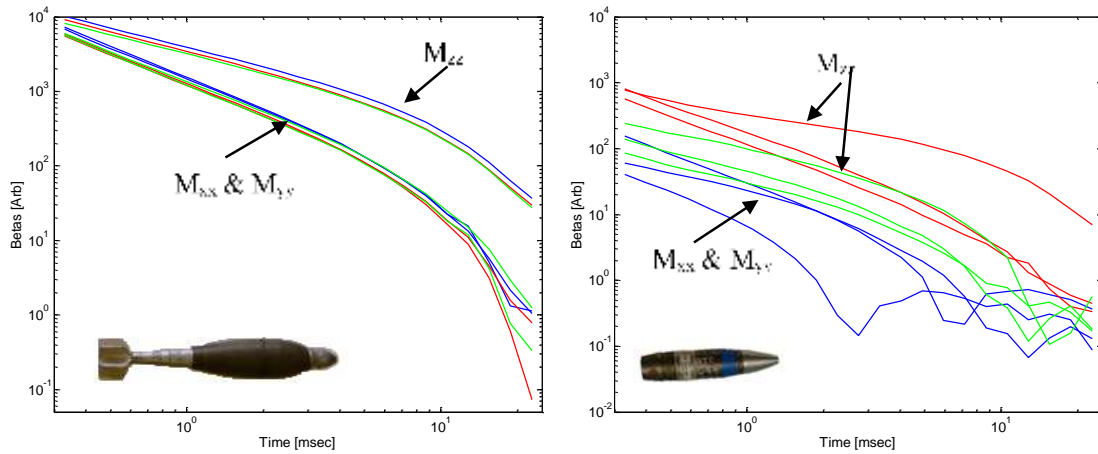
Figure 3.24: Inverted polarizability principal elements for two targets in three different setups; results for the 81-mm projectile at left and for the 40-mm munition at right. In all three cases the targets were horizontal, and the vertical distance between the MPV center and the 81-mm was 40 cm. The center to the center coordinate differences between the 81-mm and 40-mm projectiles are (–25, 0, 0) cm, (–40, 0, 0) cm, and (–25, 0, 25) cm.
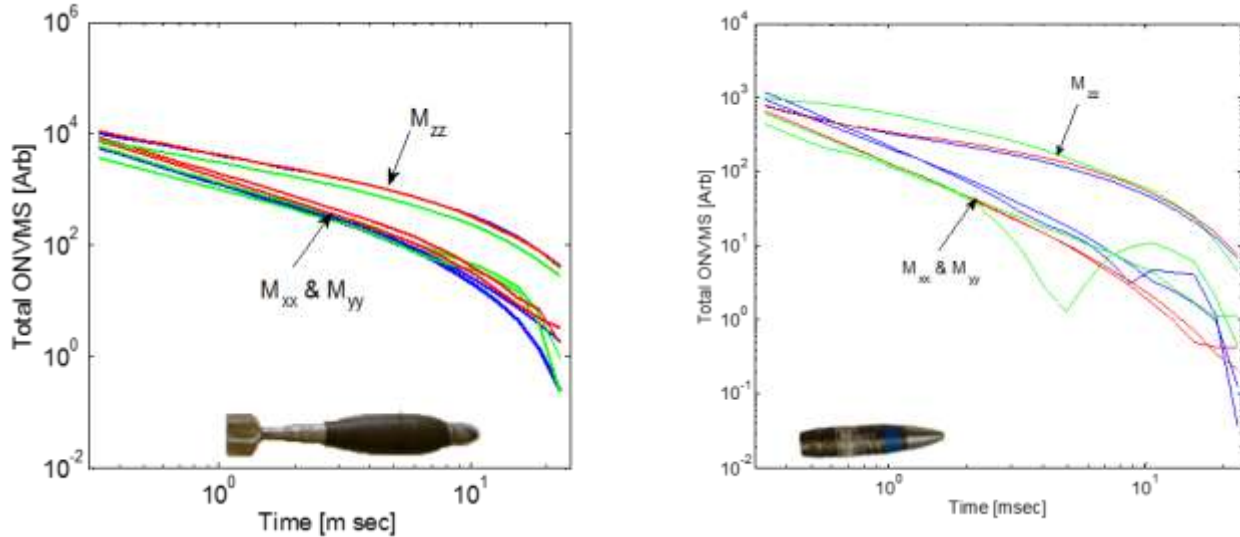
Figure 3.25: Inverted total ONMS for 81 mm (left) and 40 mm (right)

projectiles for three different cases.

We have just compared the single-dipole and ONVMS model for UXO discrimination. (We do note that in all cases we used DE to perform the crucial task of determining object locations). The dipole model is sufficient for inversion when the different targets are well separated but breaks down when they are placed close to each other or when the EMI response from one item dominates. In contrast, the physically complete model is able to predict target EMI responses accurately for these situations, making the ONVMS method our preferred tool for the live-site UXO classification studies we present next.

3.4   ESTCP live-site classification studies using advanced models

3.4.1   Introduction

The Environmental Security Technology Certification Program (ESTCP) recently launched a series of live-site UXO classification blind tests at increasingly challenging and complex sites [57-59] aiming to demonstrate the performance of advanced EMI detection technologies and UXO discrimination and classification algorithms. The first test was conducted in 2007 at the UXO live site at the former Camp Sibert in Alabama using first-generation EMI sensors (the commercially available EM61-MK2 and EM-63, both developed by Geonics Ltd.). The Sibert test was relatively simple: one had to discriminate well-isolated large intact 4.2″ mortars from smaller range scrap, shrapnel, and cultural debris. The second ESTCP discrimination study to demonstrate the applicability of EMI classification technologies was set up in 2009 at the live UXO site in San Luis Obispo (SLO) in California and featured a more challenging topography and a wider mix of TOI [57-58]. Magnetometers and first-generation EMI sensors were deployed on the site and used in survey mode. Two advanced EMI sensing systems—the Berkeley UXO Discriminator (BUD) of Section 0 and the Naval Research Laboratory's

TEMTADS EMI array, presented in Section 3.3—were used to perform cued interrogation of the anomalies detected. A third advanced system, the Geometrics MetalMapper of Section 3.2, was used in both survey and cued modes for identifying and classifying anomalies. Among the munitions buried at SLO were 60-mm and 81-mm projectiles, 4.2″ mortars, and 2.36″ rockets; three additional munition types were discovered during the course of the demonstration. The third site chosen was the former Camp Butner in North Carolina. That demonstration was designed to investigate evolving classification methodologies at a site contaminated with 37-mm projectiles, adding yet another layer of complexity into the process [87-89]. In this chapter we describe the work we performed when we participated in those studies and summarize the results we obtained.

a) Camp Sibert

In 2006, researchers affiliated with Sky Research, Inc. collected data at Camp Sibert using the EM-63, a cart-based step-off time-domain EMI sensor produced by Geonics Ltd.[70]. The targets buried in 216 cells—some of which were empty—included unexploded 4.2″ mortar shells, mortar explosion byproducts like base plates and partial mortars (i.e., stretched-out half-shells), smaller shrapnel, and unrelated metallic clutter; some examples appear in Figure 3.26. The different items were distributed as shown in (d).

(a) 4.2″ mortar shell

(b) Base plate

(c) Half-shell

Type	Training	Testing	Total
UXO	38	34	72
Partial	12	23	35
Base	5	40	45
Scrap	6	25	31
Clutter	4	22	26
Empty	1	6	7
Total	66	150	216

(d) Cell contents

Figure 3.26: Camp Sibert anomalies: 4.2 inch, base plates and partial mortars.

We analyzed the Sibert data using HAP and NSMS. By combining those two techniques we made sure our method of analysis [123,63] avoided the tendency of inversion algorithms to linger in local minima. We performed the localization step independently at the outset and then used its results to help in the characterization, allowing for fast and accurate determination of the total NSMS for each target. We classified these NSMS values using a heuristic pattern-matching method (Section 0), an open-source implementation [124] of SVM (Section 0), and mixed modeling (Section 0). The SVM-based classification improved upon template-matching [64,65] in that it required less human intervention and was thus faster to run and easier to adapt to other sets of observations. On the other hand, the semi-supervised Gaussian mixture model provided a classification performance exceeding that of SVM, which made it our preferred statistical classification procedure for use in all subsequent classification tasks.

i) Target location and characterization; preliminary pattern-matching classification

We started the procedure by applying HAP to determine the target location for each cell. Figure 3.27 compares actual and inverted data at the first and 20th time channels (top and

bottom rows respectively) for one cell. To find the target we take a fictitious 5 m × 5 m flat square surface concentric with the plot and located 30 cm below the sensor (i.e., at ground level) and divide it into 11 × 11 patches, each of which is assumed to contain a magnetic-charge distribution of uniform density. We take the measured field data (seen on the left column of figure 33) and use Eq. (69) to determine q, which in turn allows us to determine $\psi(\mathbf{r})$ using Eq. (71) and construct the matrices of Eq. (68) to find the location. We do this separately for every time channel and get consistent location estimates from gate to gate, which lends credence to their precision. The depths thus determined are also acceptably close to the ground truth.

After finding the locations we run a fully three-dimensional orientation-free NSMS code to determine the time-dependent total NSMS amplitude for all cells. To compute $Q(t)$ we surround the target with a prolate spheroid of semiminor axis $a = 5$ cm and elongation $e \equiv b/a = 4$. This spheroid is divided into seven azimuthal belts, each of which is assumed to contain a radial-magnetic-dipole distribution of constant density. The spheroid is placed at the location estimated by the HAP method and the orientation given by the dipole moment $\mathbf{m}$ obtained from Eqs. (66) and (59)-(61). With all the pieces in place, we extract $Q(t)$ for the target. The inverted total NSMS for all anomalies, and for 4.2″ mortars, base plates, and partial mortars are depicted in figure 34.

It is evident that there are distinguishable differences between the total NSMS for the 4.2″ mortars, the base plates, and the partial mortars. Particularly at late times, each target has different natural decay characteristics that depend on its geometry and material properties. It is also important to notice that the total NSMS for the 4.2″ mortars is very well grouped. To further simplify the classification task we used the Pasion-Oldenburg law to fit the time-dependent NSMS curves, obtaining as a result the amplitudes (k), the power-law exponents (β), and the exponential-decay inverse time constants (γ), all of which we tested as classification features. We obtained the parameters by direct nonlinear least-squares fit of (58) and by linear (pseudo)inversion of its logarithm (77); both procedures gave consistent results. In general we obtain good fits to the measured fields [94]; Figure 3.27 shows that the discrepancy between the actual data and the model prediction runs only to a few percent.
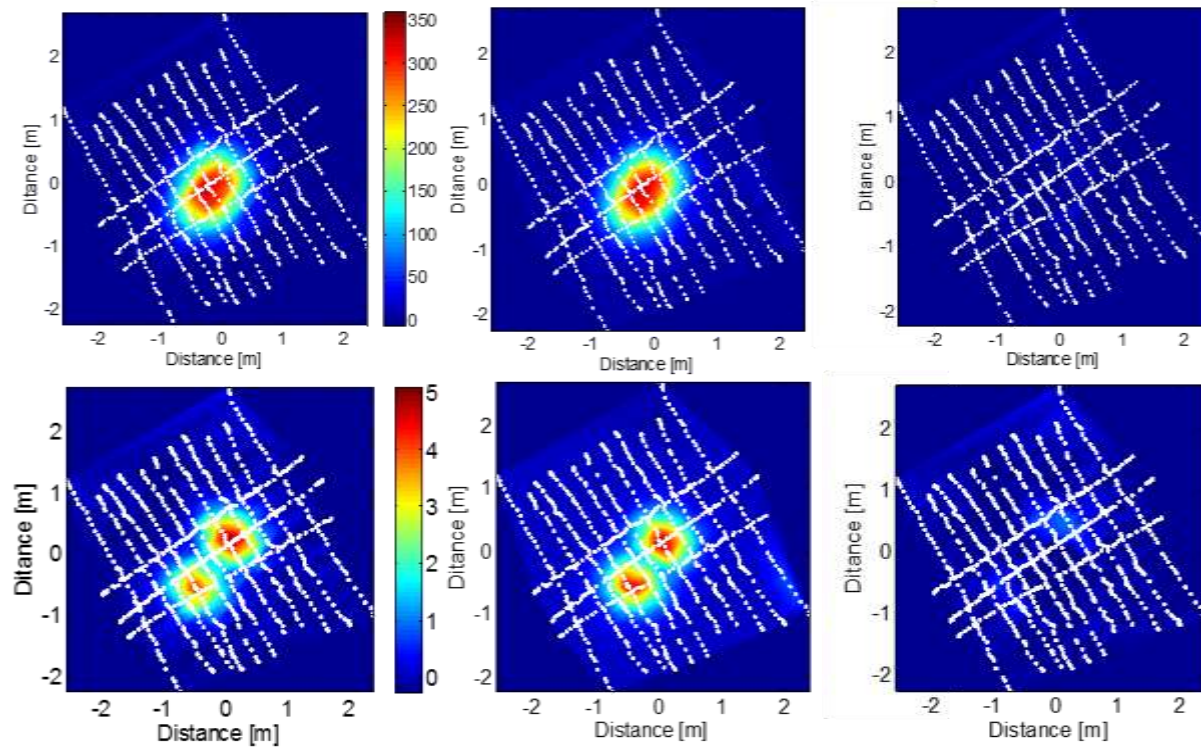
Figure 3.27: Camp Sibert EM-63 near field distributions: Left and middle columns: actual and modeled data respectively. Right column: misfits.

After investigating different combinations of these feature-space parameters we found that k in conjunction with the ratio $Q(t_{15})/Q(t_1)$ which involves a fixed superposition of β and γ, worked best: the left panel of Figure 3.27 depicts this winning combination for all items and clearly shows the tight clustering and generous cluster-to-cluster separation that generally lead to reliable classification. (The 15th time channel, centered at about 2.7 ms, was chosen because it takes place late enough to show the behavior described above but early enough that all targets still have an acceptable signal-to-noise ratio; nearby time channels produce similar results.) When we received the ground truth for all targets we proceeded to construct the ROC curve that appears in the right panel of Figure 3.36. We see that only one excavation out of 130 anomalies is necessary before all UXO are identified correctly.

We obtain similar results using the SVM algorithm.
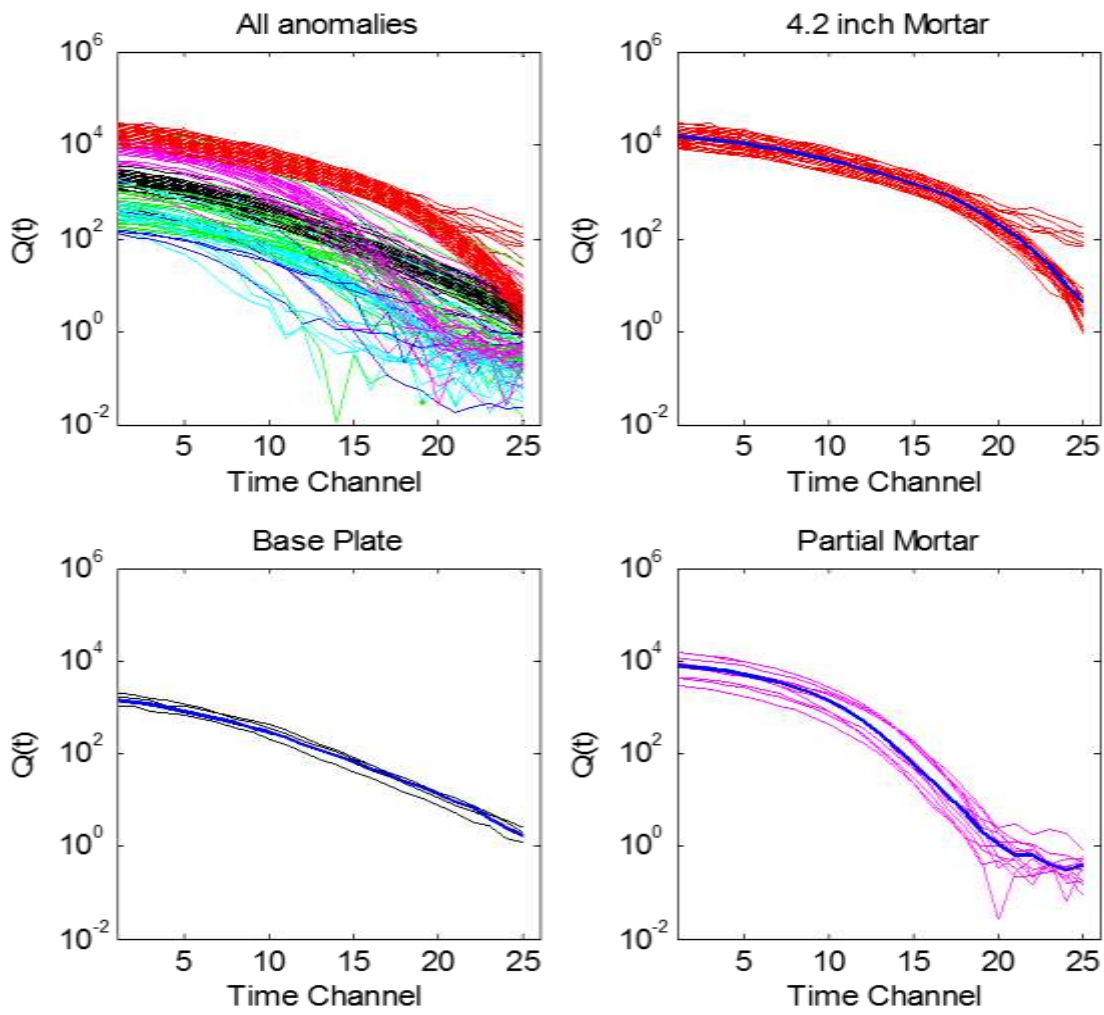
Figure 3.28: Inverted total NSMS for all anomalies: 4.2 mortars, base plates, and partial mortars.
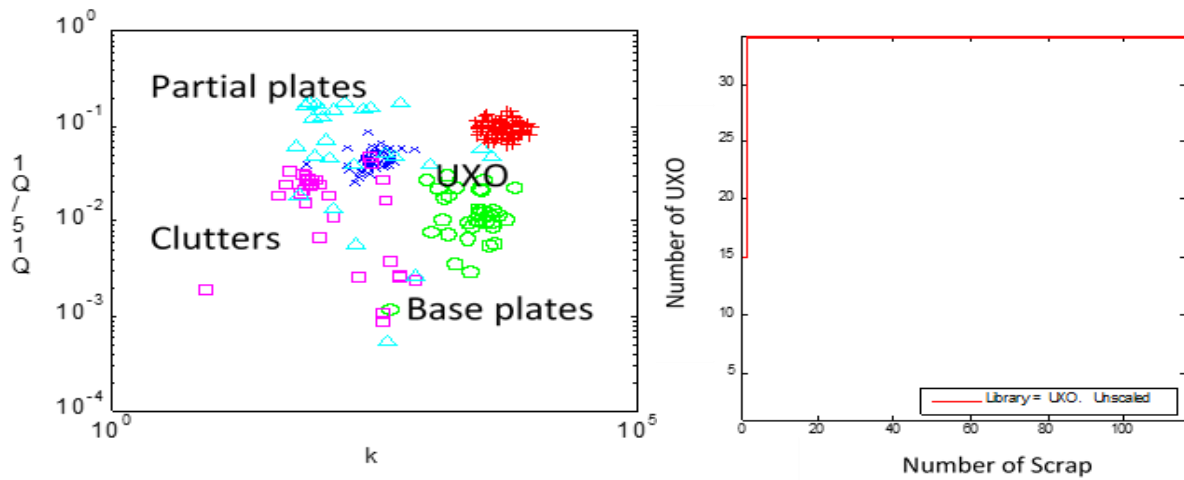
Figure 3.29: Left: Classification features. Right: ROC curve of NSMS performance.

(a) Shell at No. 7   (b) Twisted chain   (c) Crumpled debris

Figure 3.30: a) Unexploded shell from Cell No. 7 and (b,c) the two false alarms obtained by the SVM classifier using k and as discriminators.

ii) SVM classification

We use a Gaussian RBF kernel for the SVM analysis. The kernel width turns out not to have much influence on the outcome; we usually set it so that a unit in a typical x- or y-axis in a log plot (for example, Figure 3.31) comprises 100Δ Gaussian widths, where Δ is the dimensionality of the feature space. To find the capacity C we train the SVM with a subset of the training data and a given C, scramble the training set, and use a new subset of the data for testing. We then vary C, setting it to a high value initially and then lowering it, and keep the lowest capacity with which the machine identifies all dangerous

items in the test. The procedure is rather ad hoc but effective for the data at hand, given the small sample sizes, the low dimensionality of the feature spaces, and the speed of the SVM implementation. A more systematic search for C and γ using five-fold cross-validation [115-**Error! Reference source not found.**] recommends slightly higher capacities that result in identical predictions.

For R and k as features we find the best SVM performance using $C = 10$. The results are displayed (for testing data only) in SVM classification of Camp Sibert anomalies using k and R with C = 10and shown pictorially (for both training and testing) in Figure 3.31. The matrix element c_{ij} in the table denotes an item of category i that was identified by the SVM as belonging to category j; in other words, the rows of this contingency table correspond to the ground truth and the columns to predictions. The small markers in the plot show the ground truth (hollow for training data and filled for the tests), while the large markers point out the items for which the SVM makes wrong predictions. For example, a small yellow upright triangle surrounded by a large cyan square is a piece of scrap (clutter unrelated to UXO) incorrectly identified as a base plate. The UXO, with their high initial amplitudes and slow decay, are clustered at the top right corner. We see that there are only two false alarms (i.e., objects identified with UXO that were in fact something else) and that all potentially dangerous items have been identified correctly.
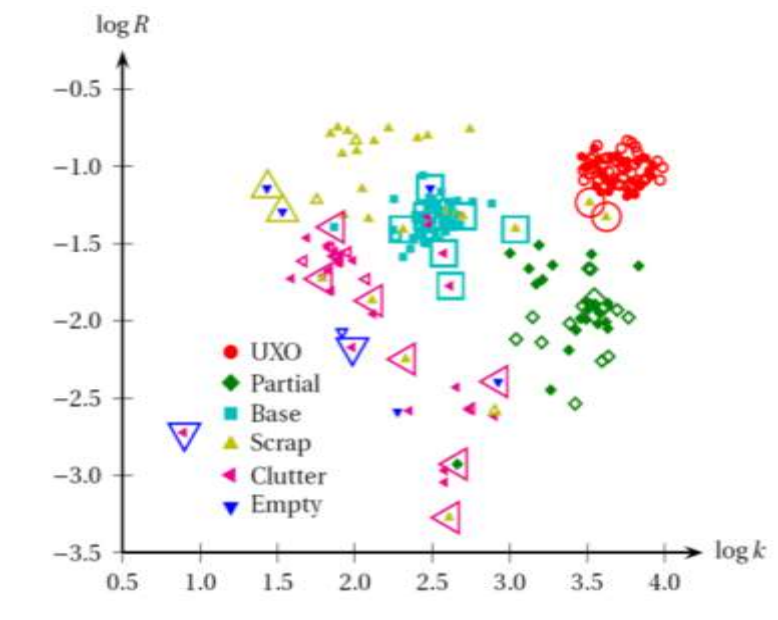

Figure 3.31: Result of the SVM classification for the Camp

Sibert anomalies using the logarithms of k and . The SVM has

been trained with capacity C = 10 and kernel width σ = 1/200.

The small markers denote the ground truth for both training

(hollow) and testing (solid) cells. The larger markers highlight

the cases where there is disagreement between the ground truth and the SVM prediction.

Table 4. SVM classification of Camp Sibert anomalies using k and R with C = 10

$k, R; C = 10$	SVM prediction					
Ground truth	UXO	Partial	Base	Clutter	Scrap	Empty
UXO	34	0	0	0	0	0
Partial	0	22	0	1	0	0
Base	0	0	39	1	0	0
Clutter	0	0	4	19	0	2
Scrap	2	0	3	4	13	0
Empty	0	1	1	1	2	1

The false alarms, two pieces of non-UXO clutter, appear in Figure 3.30: a) Unexploded shell from Cell No. 7 and (b,c) the two false alarms obtained by the SVM classifier using k and as discriminators(b) and Figure 3.30: a) Unexploded shell from Cell No. 7 and (b,c) the two false alarms obtained by the SVM classifier using k and as discriminators(c). They are seen to be similar to the 4.2″ mortars in size and metal content (cf. Figure 3.37: Five ROC curves that indicate the performance of the mixed model approach to Camp Sibert data(a)), which makes their k and R values lie closer to the tight UXO cluster than to any other anomaly. Here we note that, as can be seen in Figure 3.26 (d), the training data provided by the examiners was somewhat biased toward UXO, while clutter and scrap samples were underrepresented (this was not the case with the testing data and should not be expected in future tests). If we switch training and testing data in the SVM analysis we can achieve perfect discrimination without varying the capacity—though in this case we have more training data than tests. This highlights the importance of having a diverse collection of representative samples to use during the training stage.

Table 5. SVM classification of Camp Sibert anomalies using γ and k with C = 9

$\gamma, k; C = 9$	SVM prediction					
Ground truth	UXO	Partial	Base	Clutter	Scrap	Empty
UXO	34	0	0	0	0	0
Partial	5	17	0	1	0	0
Base	0	0	39	0	1	0
Clutter	0	0	4	15	5	1
Scrap	2	1	3	5	11	0
Empty	1	1	2	2	0	0

We can repeat the analysis using other two-dimensional combinations of the Pasion-Oldenburg parameters. Combining k and γ yields results similar to those of k and R, as Figure 3.32 and show. Figure 3.33 and **Error! Reference source not found.** show the classification resulting from the use of β and γ as discriminators. The table shows that we can obtain reasonable discrimination, with all the UXO once again correctly identified, but the increased number of false alarms and the very high capacity needed (four orders

of magnitude larger than the previous ones) indicate that this combination of parameters may not be optimal and that this machine is prone to overfitting. A glance at the figure shows the clustering is much less clear-cut than in the previous cases, partly because the range of β is rather small. In fact, combining k and β greatly reduces the performance, since the small β-range and the close similarity in k of the UXO and the partial mortars cause an overlap between the two categories that cannot be disentangled.

It is helpful and straightforward to increase the dimensionality of the feature space. Figure 3.33 shows the discrimination obtained by running the SVM using all three Pasion-Oldenburg features. The capacity $C = 9$ here, and increasing it changes the results only slightly. The number of false alarms increases: we get the same two pieces of scrap from before, and now a few of the partial mortars are identified as UXO by the algorithm, due in part to the small range of β and in part to the large gap between the UXO and the other anomalies, clearly visible in the figure, which again calls out for more and more-diverse training information.

Finally, it is possible to dispense with the Pasion-Oldenburg model altogether and run an SVM using the "raw" $Q(t)$ as input. The feature space has dimensionality $\Delta = 25$. We scale the values by $Q(t_1)$ and take the logarithm. We find $C = 20$ to be the optimal value. Table 4 shows the results. The performance is slightly inferior to that of R vs. k; the usual two false alarms are there, along with a few new ones. All the UXO are identified correctly. We can also use the logarithm of Q without any scaling (though the SVM internally rescales the feature space to $[0,1]^\Delta$). A capacity $C = 1$ suffices here. The results appear on **Error! Reference source not found.**. All dangerous items are once more identified as such.
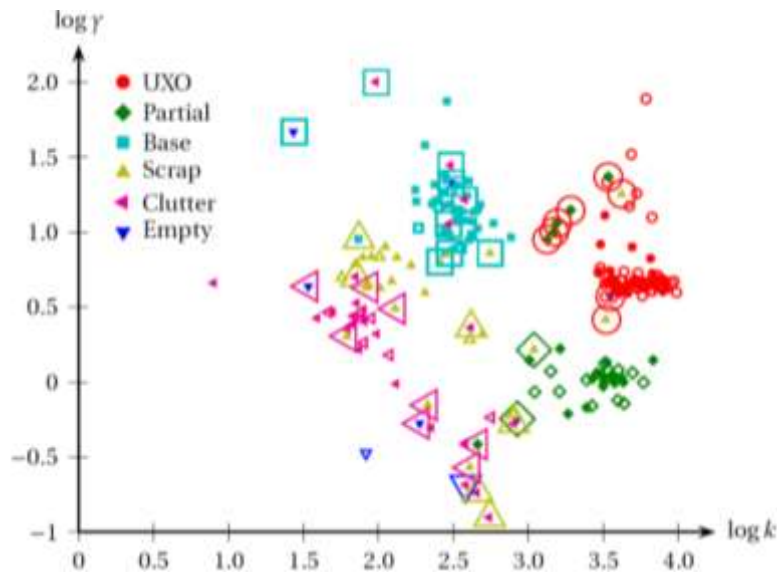

Figure 3.32: Result of the SVM classification for the Camp

Sibert anomalies using the logarithms of the Pasion-Oldenburg

parameters k and γ. The SVM here has a capacity C = 9. The small markers denote the ground truth for both training (hollow) and testing (solid) cells. The larger markers show the wrong SVM predictions.
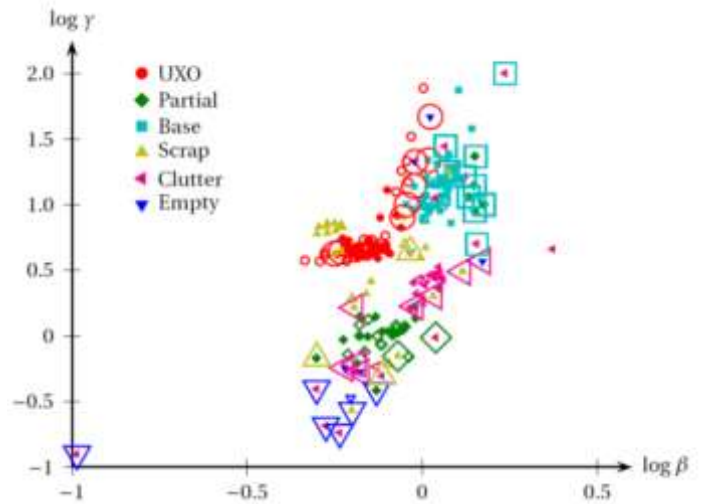

Figure 3.33: Result of the SVM classification for the Camp Sibert Anomalies using the logarithms of the Pasion- Oldenburg parameters β and γ. The SVM capacity C = 105. The small markers denote the ground truth for both training (hollow) and testing (solid) cells. The larger markers highlight the wrong predictions made by the SVM.
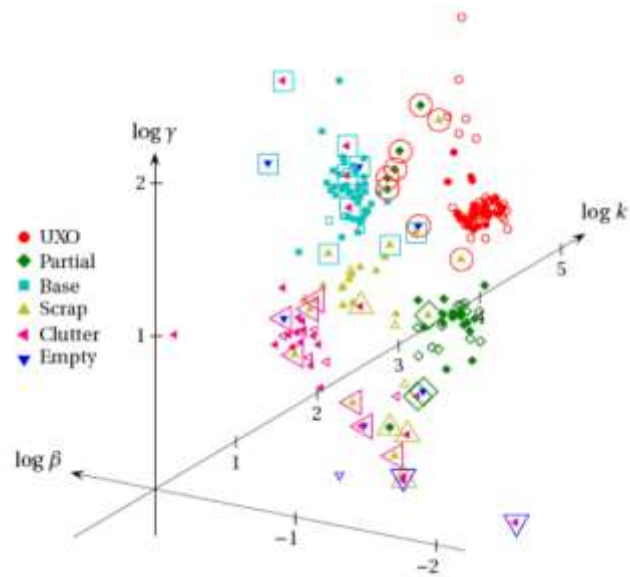
Figure 3.34: SVM classification of the Camp Sibert Anomalies using the logarithms of k, b, and g. The SVM has C = 9. The small markers denote the ground truth for both training and testing cells. The larger markers highlight the cases where there is disagreement between the ground truth and the SVM prediction.

Table 6. SVM classification of Camp Sibert anomalies using β and γ with C = 105

γ, β; C = 10^5	SVM prediction					
Ground truth	UXO	Partial	Base	Clutter	Scrap	Empty
UXO	34	0	0	0	0	0
Partial	0	14	5	2	1	1
Base	3	0	37	0	0	0
Clutter	0	1	5	14	1	4
Scrap	3	1	1	3	13	1
Empty	2	0	0	3	1	0

Table 7.   SVM classification of Camp Sibert anomalies using the complete NSMS time decay

$Q/Q(t_1)$; $C=20$		SVM prediction					
		UXO	Partial	Base	Clutter	Scrap	Empty
Ground truth	UXO	34	0	0	0	0	0
	Partial	0	15	0	7	1	0
	Base	3	0	34	3	0	0
	Clutter	0	2	3	14	4	2
	Scrap	3	1	3	3	12	0
	Empty	2	2	1	0	1	0

ii) SVM analysis of Camp Sibert data: summary

In this section we applied the NSMS model to EM-63 Camp Sibert discrimination data. First the locations of the objects were inverted for by the fast and accurate dipole-inspired HAP method. Subsequently each anomaly was characterized at each time channel through its total NSMS strength. Discrete intrinsic features were selected and extracted for each object using the Pasion-Oldenburg decay law and then used as input for a support vector machine that classified the items.

Our study reveals that the ratio of an object's late response to its early response can be used as a robust discriminator when combined with the Pasion-Oldenburg amplitude k. Other mixtures of these parameters also result in good classifiers. Moreover, we can use Q directly, completely obviating the need for the Pasion-Oldenburg fit. In each case the classifier runs by itself and does not require any human intervention. The SVM can be trained very quickly, even when the feature space has more than 20 dimensions, and it is a simple matter to add more training data on-the-fly. It is also possible to use already processed data to classify examples as yet unseen.

We should stress that none of our classifications yielded false negatives: all UXO were identified correctly in every instance. (This is due in part to the clean, UXO-intensive training data provided by the examiners and may change under different conditions.) The number of false alarms (false positives) varies with the classification features, but is in general low and can be as low as 2 out of 36 reported positives. Figure 3.31, Figure 3.32 and Figure 3.33 show, among others, how these false alarms occur: Some of the clutter items have a response that closely resembles that of UXO. While this will inevitably arise, it may still be possible to make the SVM more effective—and perhaps approach 100% accuracy—by including some of these refractory cases during the training. That said, there will certainly be cases in the field where the non-uniqueness inherent to noisy inverse scattering problems will cause the whole procedure to fail and yield dubious estimates. In those cases it will be necessary to assume the target is dangerous and dig it up.

In a completely realistic situation, where in principle no training data are given and the ground truth can be learned only as the anomalies are excavated, one can never be sure

that the data already labeled constitute a representative sample containing enough of both hazardous and non-hazardous items. This difficulty is mitigated by two facts: 1) Usually at the outset we have some idea of the type of UXO present in the field, and 2) The (usually great) majority of detected anomalies will not be UXO and thus random digging will produce a varied sampling of the clutter present. Methods involving semi-supervised learning exploit this gradual revealing of the truth and have been found to perform better at UXO discrimination than supervised learning methods like SVM when starting from the point dipole model [63,66]. (Active learning methods, which try to infer which anomalies would contain the most useful information and could thus serve to guide the anomaly unveiling, show further, though fairly minor, improvement.) Combining this more powerful learning procedure with the excellent performance of the HAP/NSMS method may enhance the discrimination protocol and should be the subject of further research.

In summary, the results presented here show that our search and characterization procedure, whose effectiveness is apparent from several recent studies [64-65,67], can be combined with an SVM classifier to produce a UXO discrimination system capable of correctly identifying dangerous items from among munitions-related debris and other natural and artificial clutter.

We repeated the analysis using the semi-supervised Gaussian mixture approach. The solution process and results are presented in Section 0. We found that the method provides excellent classification performance and has the advantage over SVM that it is less dependent on training data. This made it our preferred statistical classification model, and we have continued to prefer it.

iv) Mixed model approach applied to Camp Sibert data

We also tested the mixed model approach [107-114]. on the 216-sample Camp Sibert data. Initially we took the time decay of the total NSMS over 25 time channels for all targets and parameterized it using the Pasion-Oldenburg law of equation. Taking the logarithm of that equation we arrive at the linear model

$$\ln Q(t) = \ln k - \beta \ln t - \gamma t$$

(77)

As features we use k and the ratio $Q(t_{15})/Q(t_1)$. Figure 3.35 is a log-log plot of $Q(t_{15})/Q(t_1)$ vs. k. Initially we used K-means clustering to estimate the number of target types; the algorithm found five clusters (see Figure 3.35). Then we proceeded to classify the targets. The resulting classification into the five classes is depicted in Figure 3.36 and the corresponding ROC curves are presented inFigure 3.37.

The results illustrated that the semi-supervised Gaussian mixture model provides excellent classification performance over the SVM. This made the semi-supervised Gaussian mixture our preferred statistical classification model, and was used in the consequence classification studies.
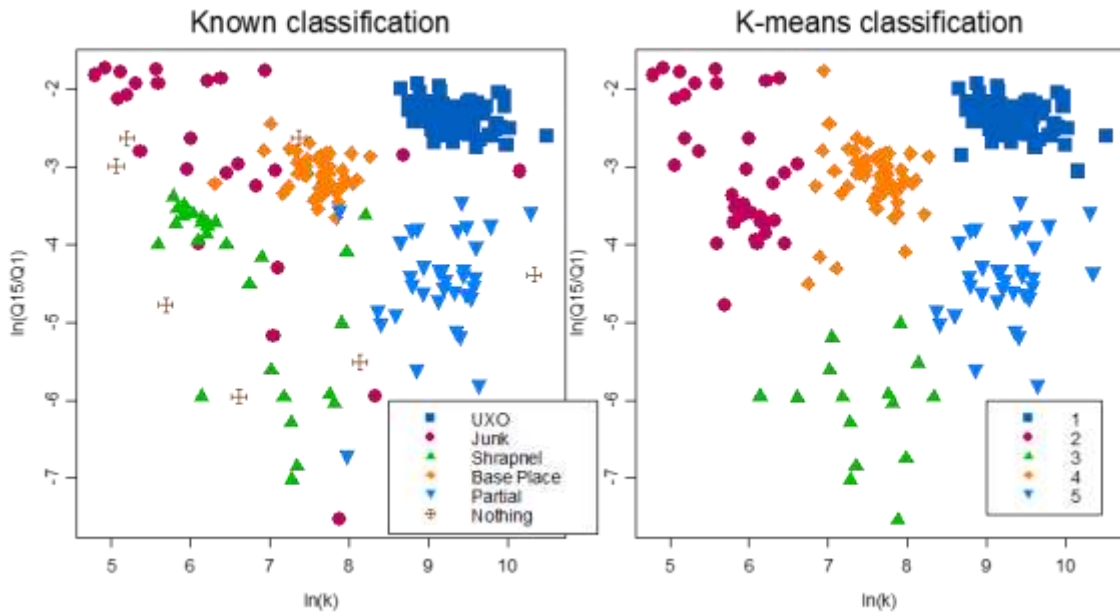
Figure 3.35: Log-scale plot of vs. for Camp Sibert data classification. Left: Ground truth. Right: K means clustering result.

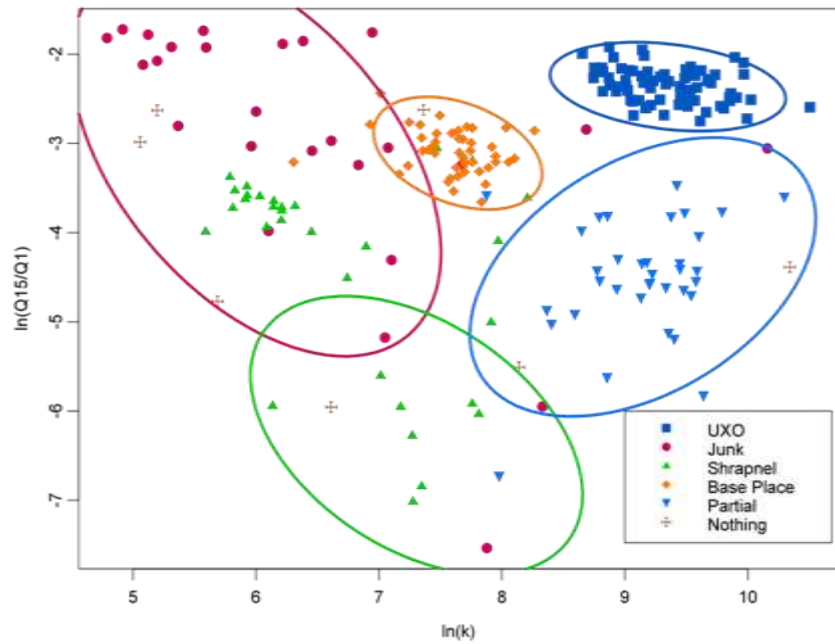
Figure 3.36: Classification of 216 targets into five classes using

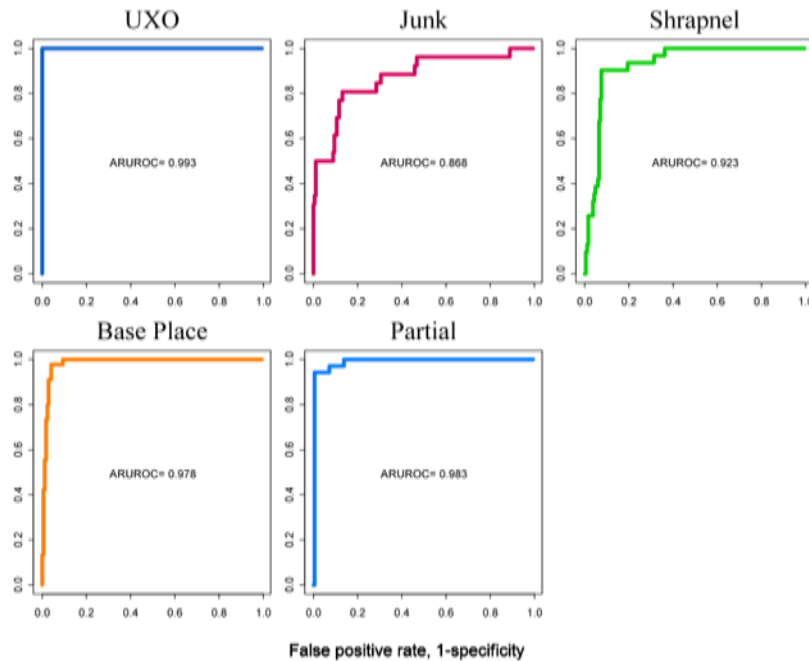a bivariate normal mixture. Also shown are the 95% confidence ellipses.

Figure 3.37: Five ROC curves that indicate the performance of the mixed model approach to Camp Sibert data.

b) Camp San Luis Obispo (TEMTADS, MM, BUD)

The discrimination test at Camp Sibert UXO site was relatively simple: it involved discrimination of large intact ordnance from smaller clutter using data from using first-generation EMI sensors. Real sites, however contain assorted types of ordnance, many smaller than 4.2″, and the need to tackle this more forbidding condition has prompted significant developments in both detection and discrimination technologies. Acceptance of these technologies requires demonstrating that they can achieve 100% discrimination confidence in terms of the range of ordnance types and their overlap with clutter, while taking into account the terrain/vegetation at the site and the effects of the geological setting on EMI sensors [3,7,**Error! Reference source not found.**,63,68,69].

To demonstrate the applicability of the classification technologies for a live-UXO site with more challenging topography and a wider mix of targets-of-interest, in 2009 ESTCP conducted a second discrimination study at the SLO live UXO site in California. Magnetometers and first-generation EMI sensors were deployed to the site and used in survey mode. Then the BUD and TEMTADS systems were used to perform cued interrogation of the detected anomalies. Simultaneously, the MetalMapper was used in

both survey and cued modes. The collected data were preprocessed by data collection demonstrators, who performed background subtraction, drift correction, and sensor positioning.

The classification demonstrators were provided with calibration data sets for algorithm testing and classification performance analysis. The goal was not only to identify if the target was harmful, but also to classify it completely; i.e., to identify its type, size, and caliber. The blind data sets contained one or more buried objects that could be either one of four ordnance items used at the site—60-mm mortar shells, 2.76″ rockets, 81-mm projectiles, and 4.2″ mortars—or a piece of clutter. The clutter items found on the site are UXO explosion byproducts like partial mortars (i.e., stretched-out half-shells), smaller shrapnel, and man-made metallic clutter; some examples appear in Figure 3.38.

This section presents the discrimination studies carried out on 1282 TEMTADS and 1407 MetalMapper cued blind data sets. The total parameterized NSMS amplitudes were used to discriminate TOI from metallic clutter and to classify the different hazardous objects. First we used the combined NSMS/DE algorithm to determine the total NSMS for each TOI from the training data provided by SERDP. We used the HAP method and a combined dipole/Gauss-Newton approach to validate the location and orientation estimates given by NSMS/DE. We then used the inverted total NSMS to extract time-decay classification features for all cases and input these to several multi-class statistical classification procedures to perform discrimination. Once our inversion and classification algorithms were tested on calibration data we repeated the procedure on the blind data sets. The inverted targets were ranked by target ID and submitted to SERDP for independent scoring.

Figure 3.38: Found Clutter Items on SLO UXO live sites.

i) The total NSMS for discrimination

The reader may recall from chapter (3) that the initial amplitude and the decay rate of the total NSMS depend on the size, the geometry, and the material composition of the object it represents. Early-time responses are associated with surface eddy currents and the associated early-time NSMS is directly proportional to the object's surface; at later times the currents diffuse gradually into the object and the response is related to the target's volume. Thus a small and thin target like the partial 2.36″ rocket has a relatively small initial NSMS that decays quickly, while a large object like the 4.2″ mortar of figure 46 has a strong immediate response that decays slowly, particularly along its axis of symmetry.

These considerations may be put on a more quantitative footing through discrimination features that summarize these characteristics for the different NSMS curves. To that end we employ the Pasion-Oldenburg law in its parameterized form. We tried different combinations of $B_{\alpha\alpha}$ $\beta_{\alpha\alpha}$, and $\gamma_{\alpha\alpha}$ for discrimination and in the end settled for $\log[M_{zz}(t_{82})/M_{zz}(t_1)]$ and $M_{zz}(t_1)$ as features for use with the model-based supervised clustering figure 47.

ii) SLO discrimination results

The SERDP Program Office provided us with 188 TEMTADS calibration data sets for the inversion and classification algorithms testing performance analysis. Our objective here was not only to identify if a given target was a UXO or not, but also to classify it completely; *i.e.*, to identify TOI type, size, and caliber. We had the same number of calibration data sets for the Metal Mapper sensor, but we used only two data sets for each TOI, for a total of ten data sets. The blind data sets contained a single or multiple buried objects that could be either one or more TOI.

We used the 188 TEMTADS calibration data to build a catalog of expected total NSMS values that were then tested on the 1282 other cells. The TEMTADS took data over 115 channels that span in approximately logarithmic fashion a lapse of time between 100 μs and 24 ms. The TEMTADS was always placed 30 cm above the ground. For each data set we run the combined NSMS-DE and NSMS-HAP method [4] to determine object locations.

The target response was approximated with set of magnetic dipoles distributed on a spherical surface of radius 5 cm. This sphere is divided into 17 sub-surfaces, each of which is assumed to contain a magnetic-dipole distribution of constant density. Once the location of the sphere's center is determined then the magnitude of each responding source is obtained and the total NSMS is calculated. The inverted total NSMS curves for SLO TEMTADS calibration (green lines) and blind data sets (red lines) are depicted in figure 45 and figure 46 for partial 2.36″ rockets, 4.2″ mortars, 81-mm projectiles, 2.36″ rockets, and 60-mm mortars. The results indicate that the inverted and calibration total NSMS time decay curves are similar and are good discriminators. Also, as the size of the TOI decreases the inverted total NSMS time decay curves show a larger spread, making them more difficult harder to discriminate.
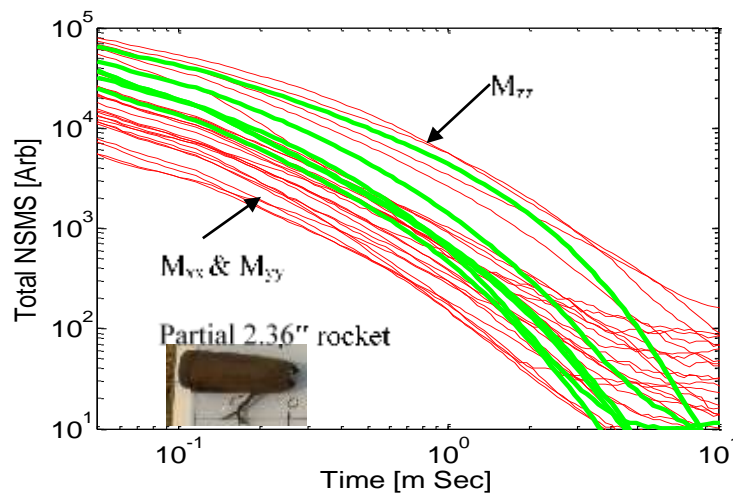

Figure 3.39: Inverted total NSMS time decay profiles for the

2.36 partial rocket. The green lines depict calibration data and the red lines correspond to blind SLO TEMTADS data sets.
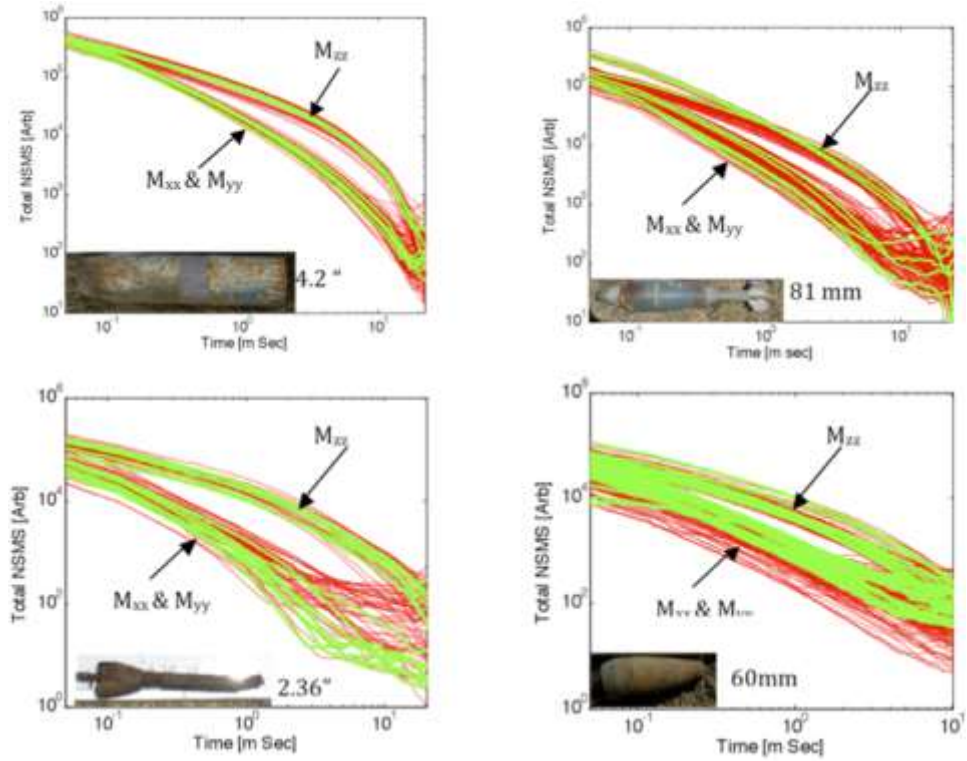

Figure 3.40: Inverted total NSMS time decay profiles for 4.2 mortars (top left), 81-mm projectiles (top right), 2.36 rockets (bottom left), and 60-mm mortars (bottom right) in the SLO TEMTADS test. The green lines depict calibration data and the red lines correspond to blind data sets.
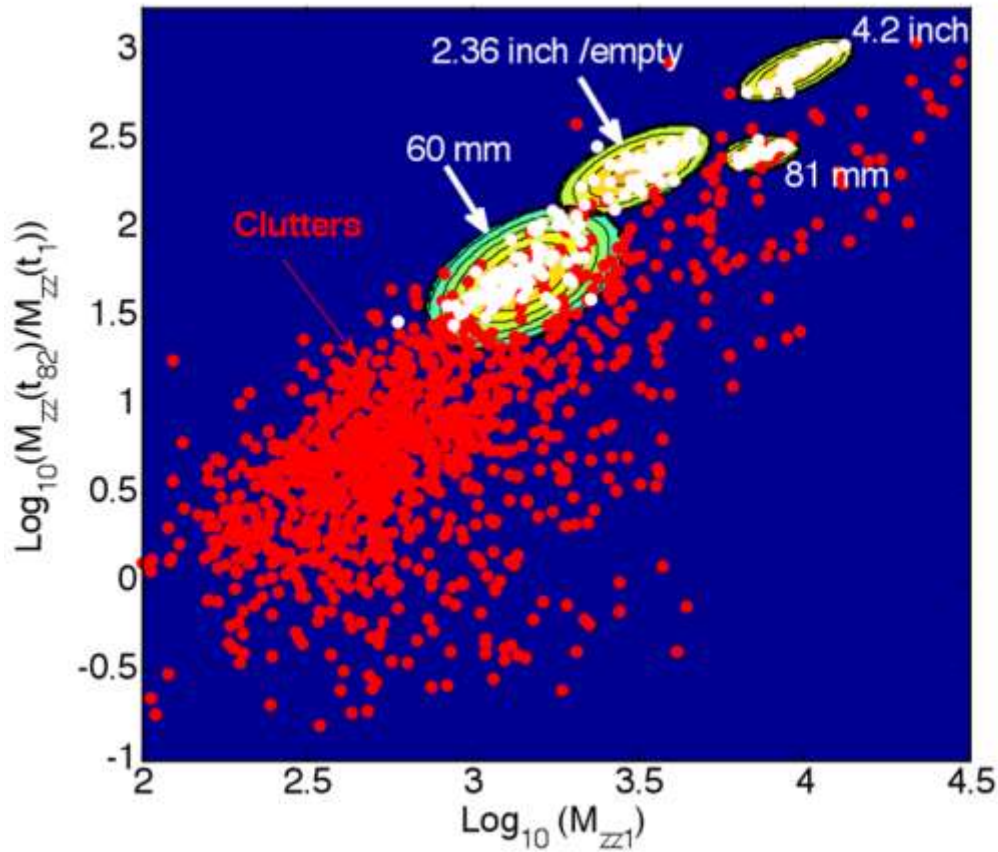
Figure 3.41: Result of the supervised clustering classification for the SLO-TEMTADS anomalies using the logarithms of and . The supervised clustering has been trained with calibration data. The red markers correspond to clutters and the white ones to TOI.

We also determine the Pasion-Oldenburg parameters $k_{\alpha\alpha}$, $\beta_{\alpha\alpha}$, and $\gamma_{\alpha\alpha}$ for each anomaly from equation (77); the inverted parameters were used in the supervised clustering algorithm. We have previously found [40] that the ratio of the inverted total NSMS at the 82nd time channel to that at the first time channel, which involves a fixed superposition of β and γ, shows discernible clustering for this particular data set when combined with the third parameter. The values of $\log_{10}(M_{\alpha\alpha}(t_1)/M_{\alpha\alpha}(t_{80}))$ versus $\log_{10}(M_{\alpha\alpha}(t_1))$ are plotted in figure 47 for all TEMTADS data sets. We see that the inverted parameters are well clustered, and for the most part noticeably distinct from those of the others, suggesting that this two-dimensional feature space is good for classification purposes. This suggestion is confirmed by the classification results that appear in Figure 3.42.
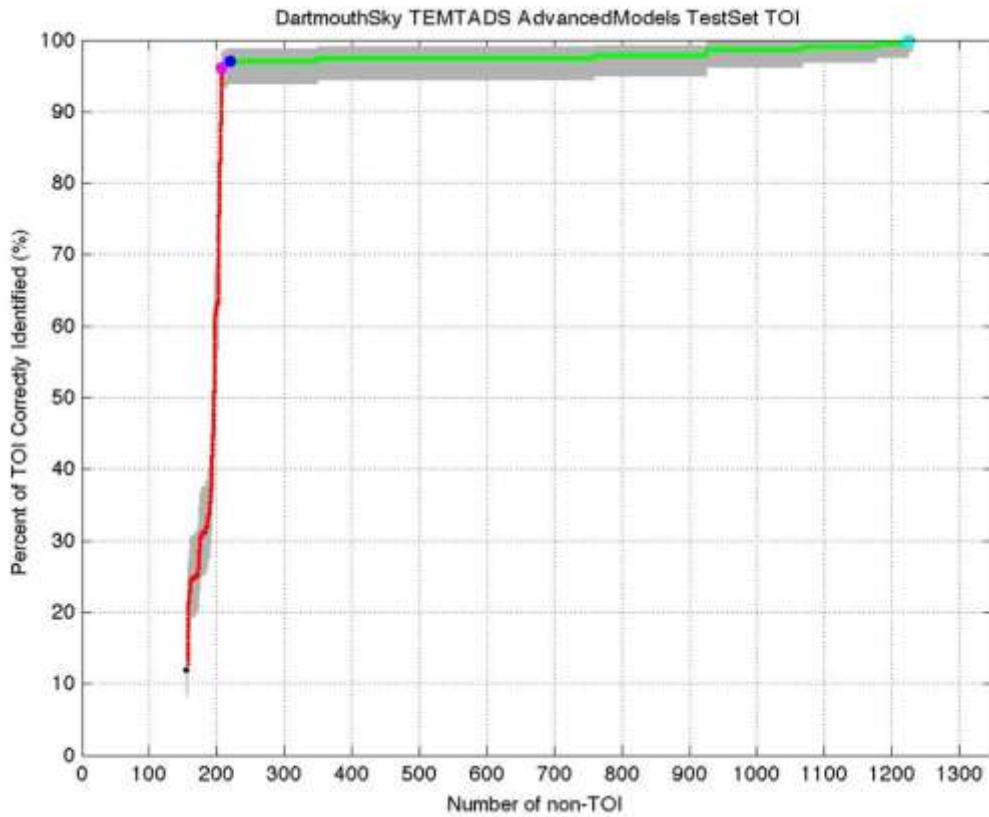
Figure 3.42: ROC curve for SLO TEMTADS test data.

The inverted SLO TEMTADS and MetalMapper test data were ranked by target type and caliber and submitted to the SERDP office for independent scoring, which was carried out by personnel from the Institute for Defense Analyses (IDA). Our discrimination results are summarized in figure 49, Figure 50 and Figure 51 Our classification technique was able to correctly identify all big UXO, (the 2.36″, 81-mm and 4.2″ projectiles) for both TEMTADS and MetalMapper data. The algorithm had only one false negative (a 60-mm mortar) for MetalMapper. In the case of TEMTADS the algorithm missed two 2.36″ rockets and five 60-mm mortars. These false negatives were mostly due to small signal-to-noise ratios.
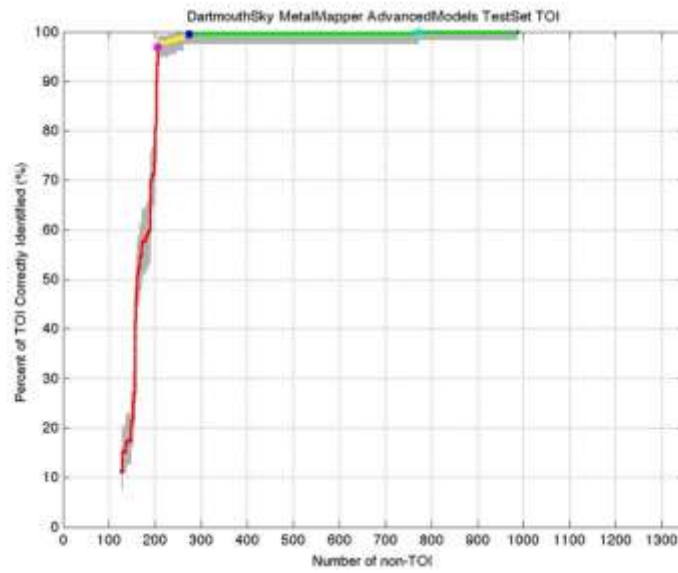
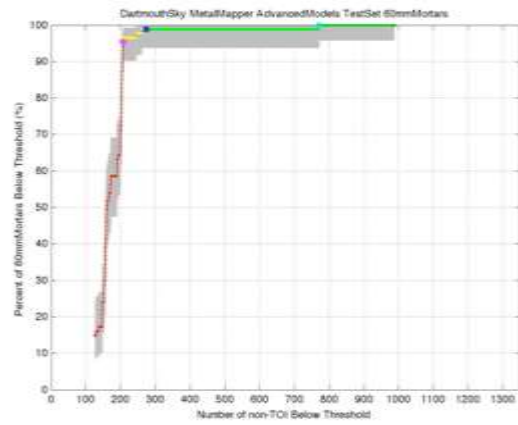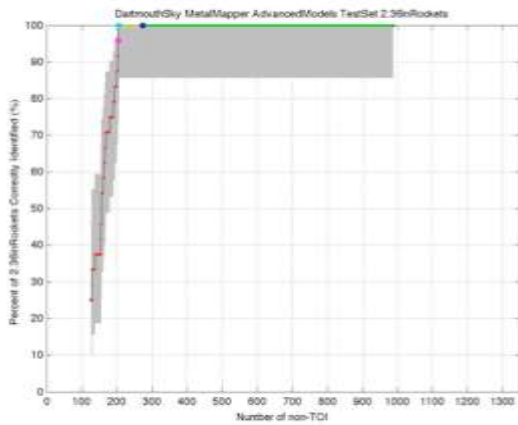Figure 3.43: ROC curve for SLO MetalMapper test data.
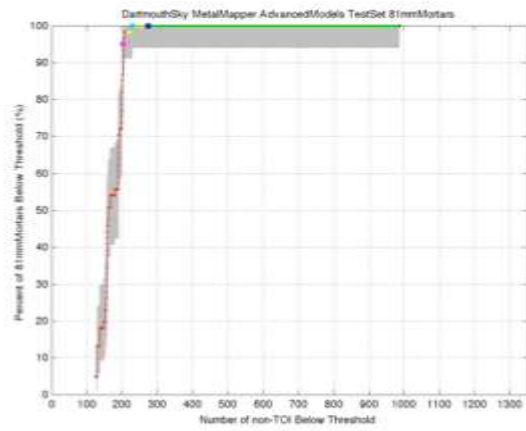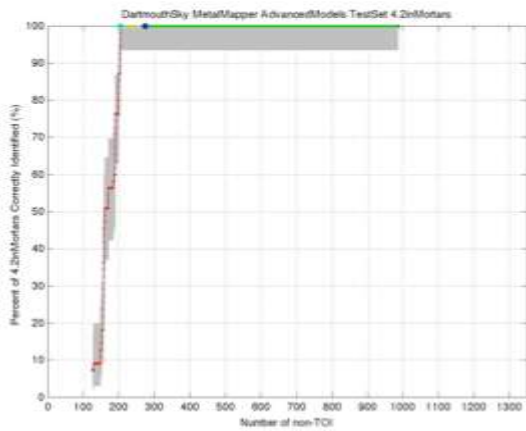
Figure 3.44: ROC for SLO TEMTADS data for individual TOI.
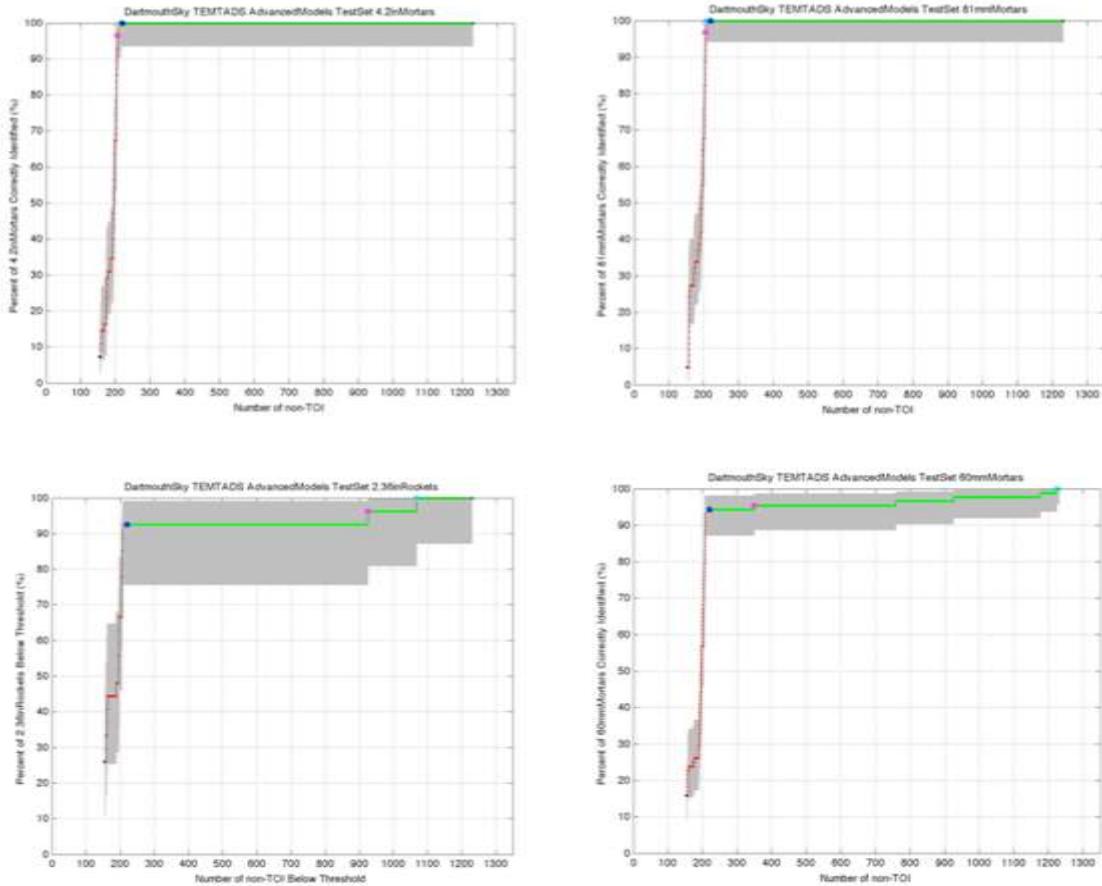
Figure 3.45: ROC for SLO MetalMapper data sets: individual TOI.

iii) Comparisons between NSMS and Dipole models

(1) Calibration SLO-TEMTADS data

We now compare the dipole and NSMS models as applied to SLO calibration data. The data were inverted using both gradient search and DE. For the gradient search 100 initial guesses were used to avoid local minima, with 30 iterations for each initial guess to guarantee convergence. For DE 100 iterations were used. Once the targets' locations were determined the dipole polarizability matrix and the total NSMS were determined and diagonalized using JD. The inverted dipole tensor principal elements and total NSMS for two calibration cells (410 and 489, shown in Figure 3.46) appear in Figure 3.47 he inverted dipole principal polarizability elements are seen to be totally different for the same 60-mm mortar. For Cell #489 the dipole elements are not symmetric, and their

inverted magnitudes are much higher than for the other cell even though the targets and burial depths are the same. The simple dipole model clearly breaks down while the NSMS technique predicts consistent results and is more stable and accurate. It is worth pointing out that other researchers reported the same problem with this cell when using the dipole model and overcame it using multiple dipoles.

Figure 3.46: 60-mm mortars actually found in calibration cells #410 and #489.
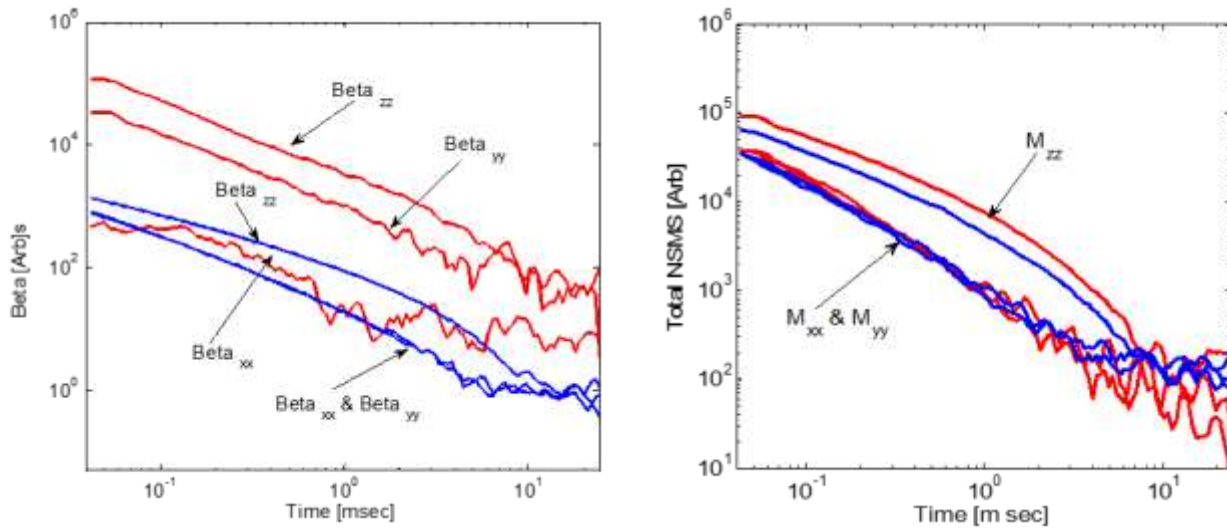
Figure 3.47: Left: Principal elements of the polarizability tensor versus time for a 60mm mortar in the SLO study. Right: Total NSMS time-decay curves for the same cases. The red curve corresponds to calibration Cell #489 and the blue curve to calibration Cell #410.

(2) Blind SLO-TEMTADS data sets

A similar performance was observed for deep targets in blind-test data. Figure 54 compares library and inverted data using the dipole and NSMS models. In this case a 60-mm mortar was buried 35 cm deep. Due to the low signal-to-noise ratio the dipole model was unable to predict stable, symmetric polarizability tensor elements, but the total extracted NSMS curves show axial symmetry and resemble the 60-mm library curve well.
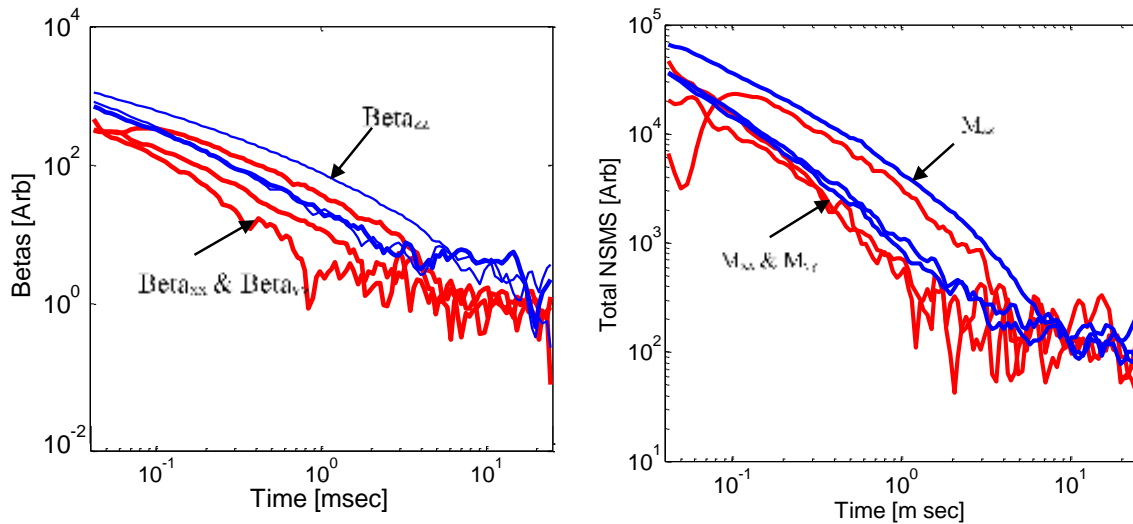
Figure 3.48: Comparison between library and inverted blind tests for the dipole model (left) and NSMS model (right).
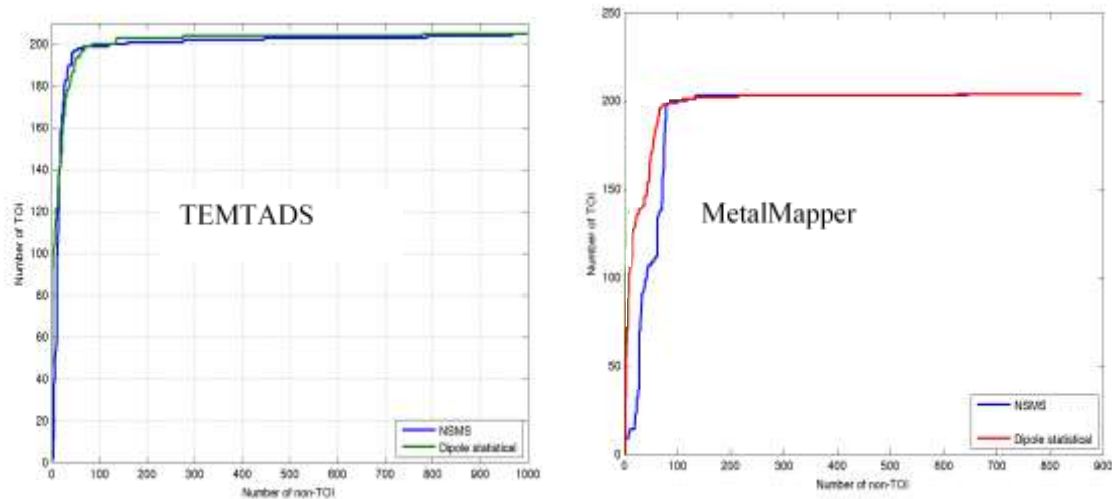
Figure 3.49: ROC curves for SLO TEMTADS and SLO MetalMapper
discrimination studies. Green and red curves: Sky/UBC dipole results;
blue curve: NSMS results obtained by our Dartmouth/Sky group.

(3) SLO-Discrimination studies

Using NSMS we inverted all SLO blind-test data sets and sorted them by target ID. The
same anomalies were inverted by researchers at SKY/UBC using the dipole model. The
ROC curves for the SLO TEMTADS and SLO MetalMapper discrimination studies are
depicted in Figure 3.49. The NSMS performs slightly better than the dipole statistical
approach for TEMTADS data. For the SLO MetalMapper data sets the NSMS shows
higher false positives in comparisons with the dipole model, but overall it has only one
false negative, while the dipole model had three false negatives.
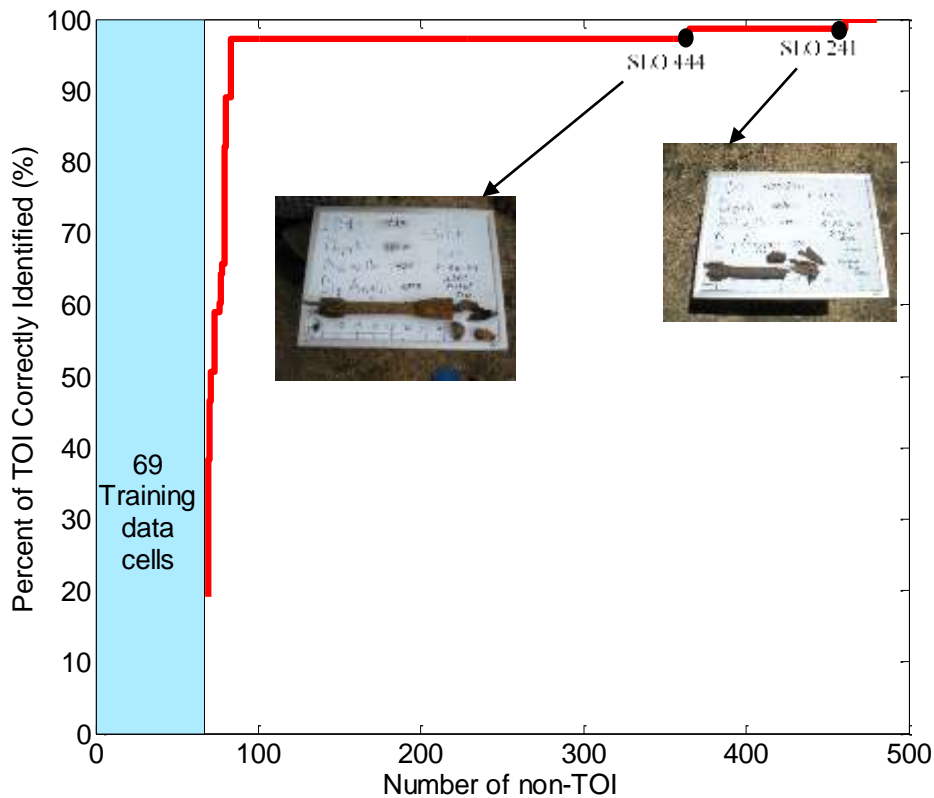
Figure 3.50: ROC curves for SLO BUD discrimination studies.

iv) SLO BUD data inversion and classification studies

The combined NSMS-DE algorithm was applied to the SLO live site BUD data sets (539 anomalies) and targets intrinsic (total NSMS) and extrinsic parameters were extracted for each anomalies. The discrimination features (size and shape information) were extracted from the total NSMS time decay history curve and anomalies were classified using the provided 69 training data set. In addition, the library matching technique, that uses the entire time decay history of the total NSMS, was also used for the classification. The inverted targets were ranked as TOI and non-TOI items. The ROC for the SLO BUD data sets is shown on figure 56. The studies showed that only two 2.36 inch rockets were misclassified.
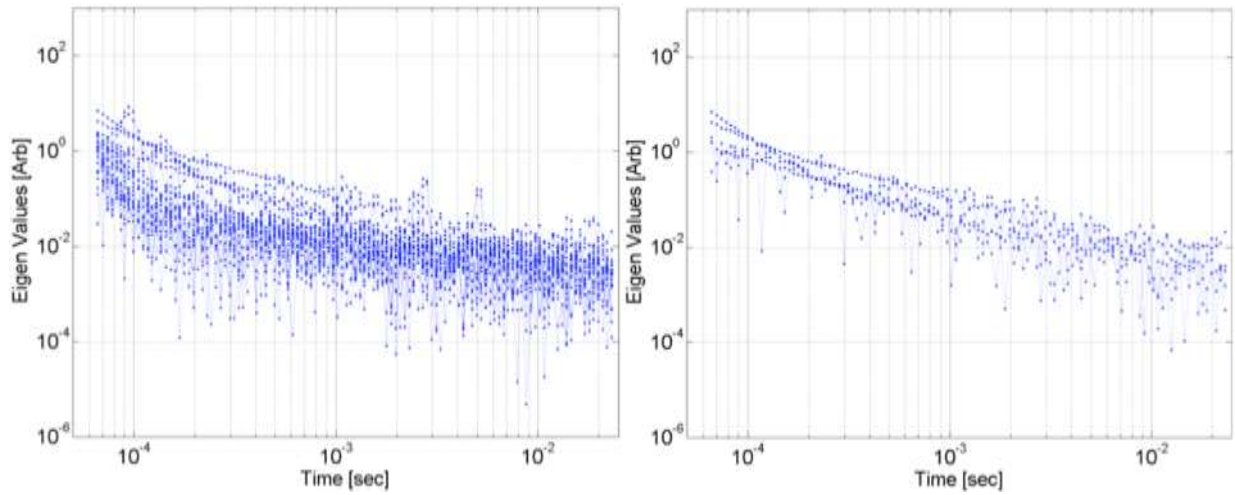
Figure 3.51 : SLO TEMTADS test Cell #16. *Left:* All 25 eigenvalues
vs. time. *Right:* Four highest eigenvalues vs. time. The target
response is weak and mixed with the sensor's electronic and
background noise.

Figure 3.52 : SLO TEMTADS test Cell #103. Left: All 25 eigenvalues
vs. time. Right: Above-threshold eigenvalues vs. time. Only two
eigenvalues are above the threshold, indicating a low signal-to-noise
ratio.

v) SLO retrospective analysis

During the SLO test our algorithms missed five 60-mm mortars and two 2.36″ rockets. The missed anomalies were in Cells #16, 103, 241, 441, 444, 748, and 1285. Figure 57 through **Error! Reference source not found.** present the results for each of these anomalies, along with our comments.

Figure 3.53: SLO TEMTADS test Cell #241. Left: All 25 eigenvalues vs. time. Right: Above-threshold eigenvalues vs. time. There more than three eigenvalues above the threshold, which indicates that the cell contains more than one target. The curves decay fast, illustrating that the targets are small.

Figure 3.54: SLO TEMTADS test Cell #441. Left: All 25 eigenvalues vs. time. Right: Above-threshold eigenvalues vs. time. There more than three eigenvalues above the threshold, indicating that the cell contained more than one target. The fast-decaying curves illustrate that the targets have thin walls or are small.

Figure 3.55: SLO TEMTADS test Cell #444. *Left:* All 25 eigenvalues vs. time. *Right:* Above-threshold eigenvalues vs. time. There more than three eigenvalues above the threshold, indicating that the cell contained several targets. In addition, the curves decay fast, illustrating that the targets are small.

Figure 62: SLO TEMTADS test Cell #748. Left: All 25 eigenvalues vs. time. Right: Above-threshold eigenvalues vs. time. More than three fast-decaying above-threshold eigenvalues indicate the presence of several small targets.
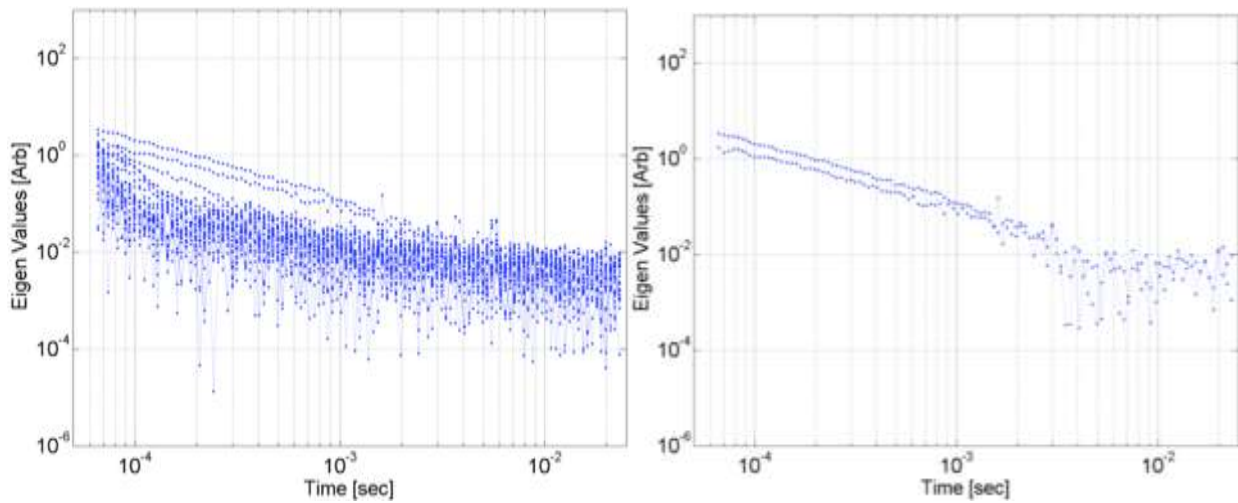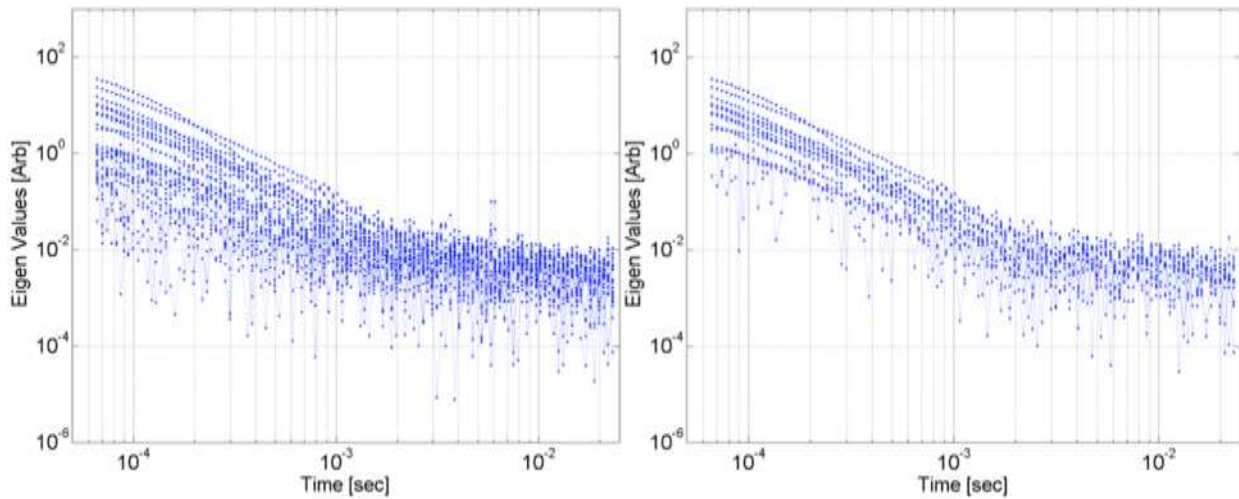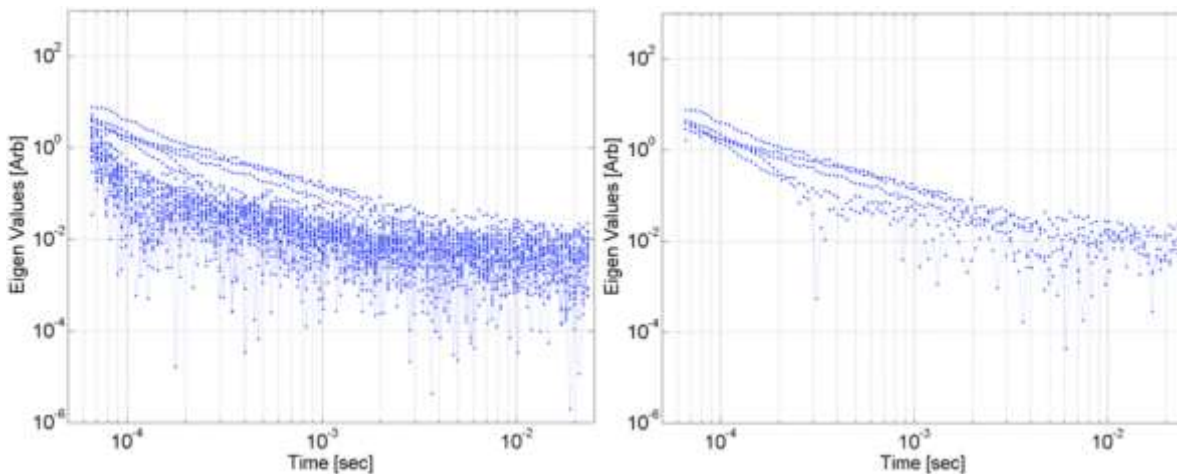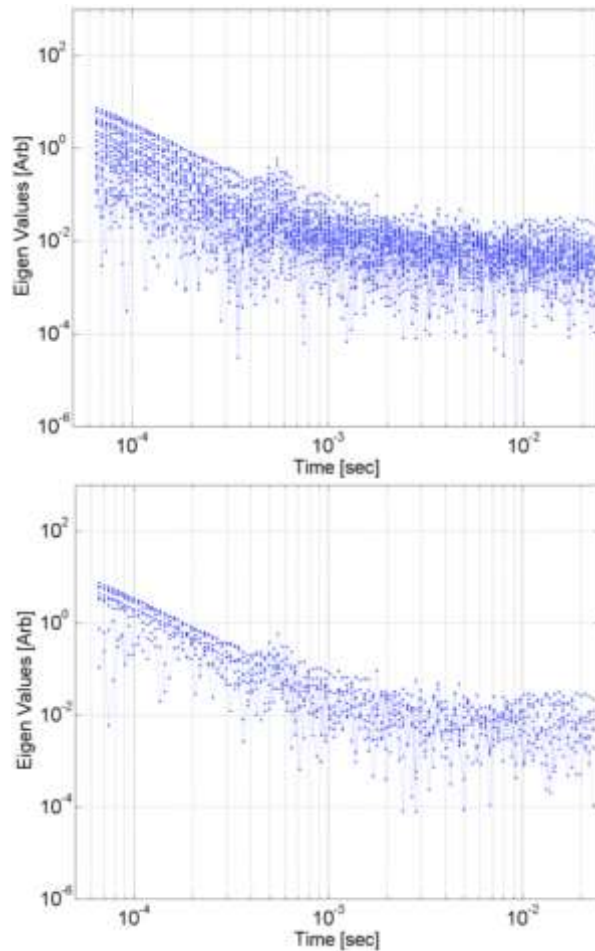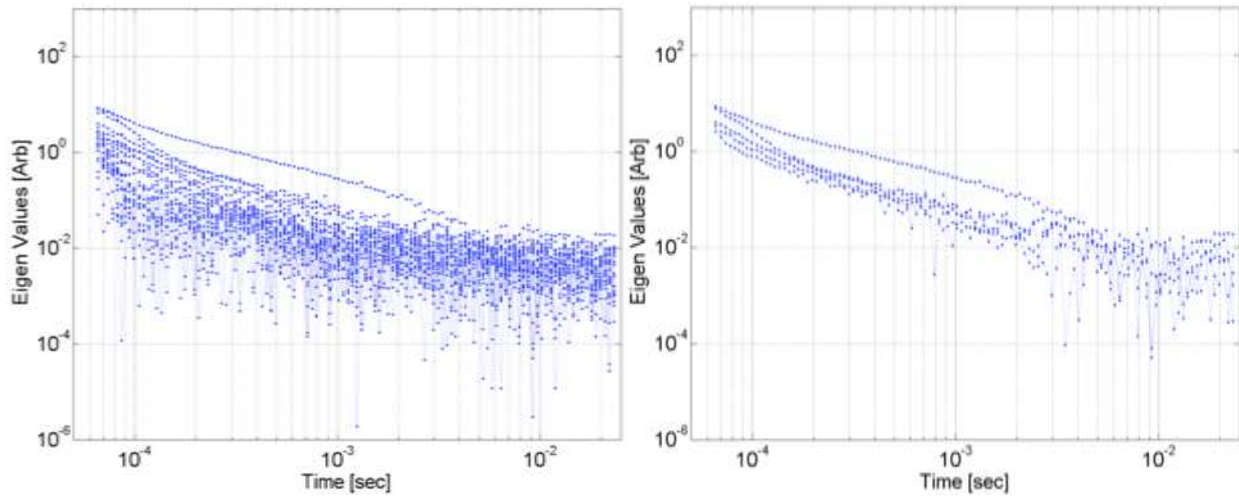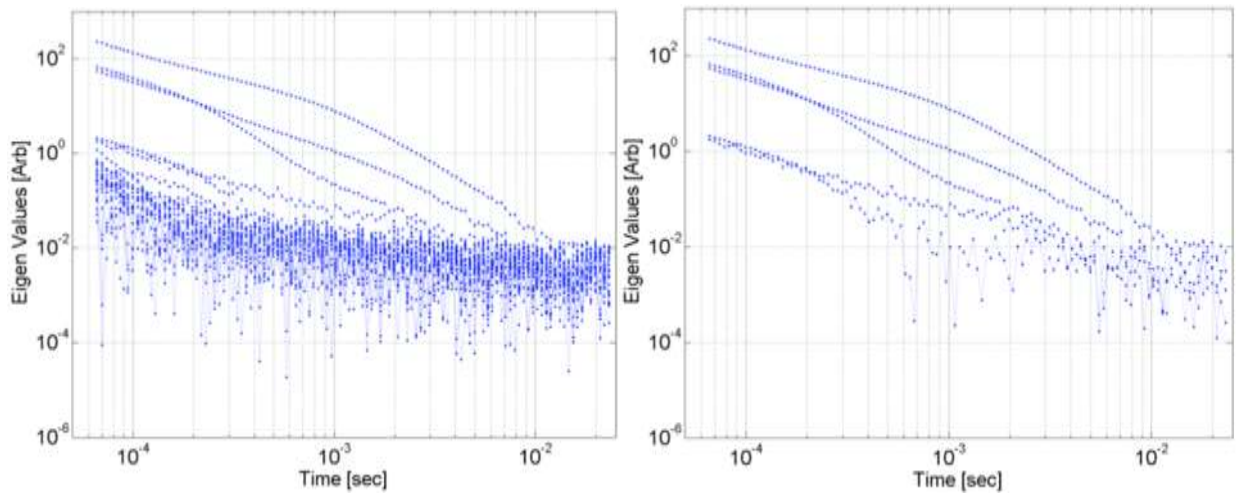

Figure 63: SLO TEMTADS test Cell #1285. Left: All 25 eigenvalues vs. time. Right: Above-threshold eigenvalues vs. time. Again, the eigenvalues indicate that there are several small targets in the cell.

c) Camp Butner

The former Camp Butner is a 40,384-acre site located approximately 15 miles north of Durham and straddling Durham, Granville, and Person Counties, all in North Carolina. The War Department acquired the property from private landowners in 1942 for use as a training and cantonment facility during World War II. The camp was primarily established for the training of infantry divisions (including the 78th, 89th, and 4th) and miscellaneous artillery and engineering units [58]. A large variety of munitions have been reported as used at the former Camp Butner, including rifle grenades, 2.36″ rockets, 37-mm and 40-mm rounds, 81-mm mortars, and 105-mm, 155-mm, and 240-mm projectiles. Although the historical records are not definitive, it is thought that the targets of interest at the site of the test are mostly 37-mm and 105-mm projectiles; some of the former have a copper band, others do not. The clutter items found on the site are for the most part UXO explosion byproducts like partial mortars (i.e., stretched-out half-shells), smaller shrapnel, and man-made metallic clutter. An initial surface clearance was carried out on the site prior to the collection of digital geophysical data. Then an EM61 survey was conducted on two $100′ \times 100′$ grids for site characterization. A surface clutter analysis and excavation of one of these $100′ \times 100′$ grids confirmed the identities of the targets of interest (TOI), provided an indication of their depth distribution, and gave the demonstrators some information about the clutter environment at the site.

At a live site such as this, the ratio of clutter to TOI is such that only a small number of TOI may be found in a 10-acre area, far from enough to determine any demonstrator's classification performance with acceptable confidence bounds. To avoid this problem, the site was seeded with enough TOI to ensure reasonable statistics. Three types of targets— 37-mm and 105-mm projectiles and M48 fuze assemblies—were thus used. The survey data for the study were collected with a line spacing of 50 cm. The detection threshold was set to detect all 37-mm projectiles at a depth of 30 cm [85], which for the EM61-MK2 carted survey corresponds to a threshold of 5.2 mV in the second time gate. Using this detection threshold a first anomaly list was produced. This list was used as a starting point for two detailed cued surveys carried out using TEMTADS and the MetalMapper.

Our team processed both data sets independently using our advanced EMI discrimination techniques and occasionally requesting training data to assist during the classification stage. The main objective of this section is to demonstrate the discrimination performance of the ONVMS model [99] in a live UXO site under realistic field conditions; the method is combined with DE optimization (the two-step approach described in Section 2.3) to determine the locations, orientations, and time-dependent total ONVMS of the subsurface targets. The latter depends on the intrinsic properties of the object in question and can be used for discrimination. To streamline the process we employed JD to estimate the number of potential targets before inverting. To classify the targets in the MM data sets we performed semi-supervised Gaussian-mixture model-based clustering on the total ONVMS in a process similar to that described. We now present the results of our discrimination and classification strategies when applied to the Camp Butner TEMTADS and MM blind cued data sets. The SERDP office provided us with 2291 cases interrogated with each system. We divided our team into two groups: One group

processed TEMTADS data and the other worked on the MM sets; each group worked independently using different classification strategies. Each team constructed a custom training list (amounting to less than 5% of the entire blind data) and requested the ground truth for those anomalies for use during the classification stage.

i) *TEMTADS data discrimination strategy and classification results using supervised clustering*

We processed all the TEMTADS data using the JD and ONVMS models. Initially we used JD to estimate the data quality and the number of potential targets. The JD algorithm constructs a multi-static response matrix using TEMTADS data and computes its eigenvectors and eigenvalues, the latter as a function of time. Studies show that these eigenvalues are intrinsic properties of the targets and that each target has at least three eigenvalues above the threshold (noise level). For example, Figure 3.57 shows the eigenvalues extracted for a 105-mm HE projectile, a 105-mm HEAT round, an M-48 fuze, and a 37-mm UXO. As the number of targets increases (as in Figure 3.56 and the third row of Figure 3.64), so does the number of eigenvalues above the noise level. We thus examined the eigenvalues versus time for each case and used them to estimate the number of targets.
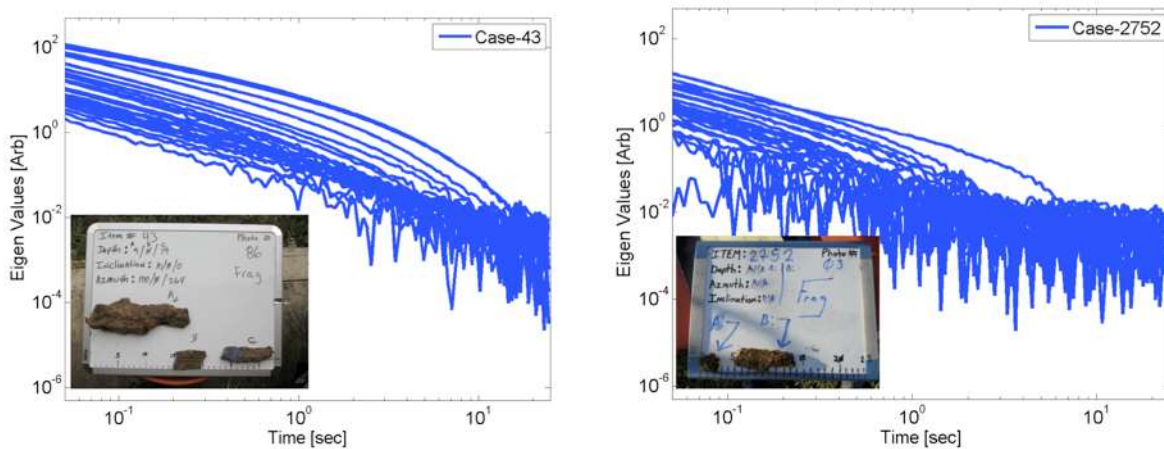

Figure 3.56: TEMTADS multi-static response matrix eigenvalues

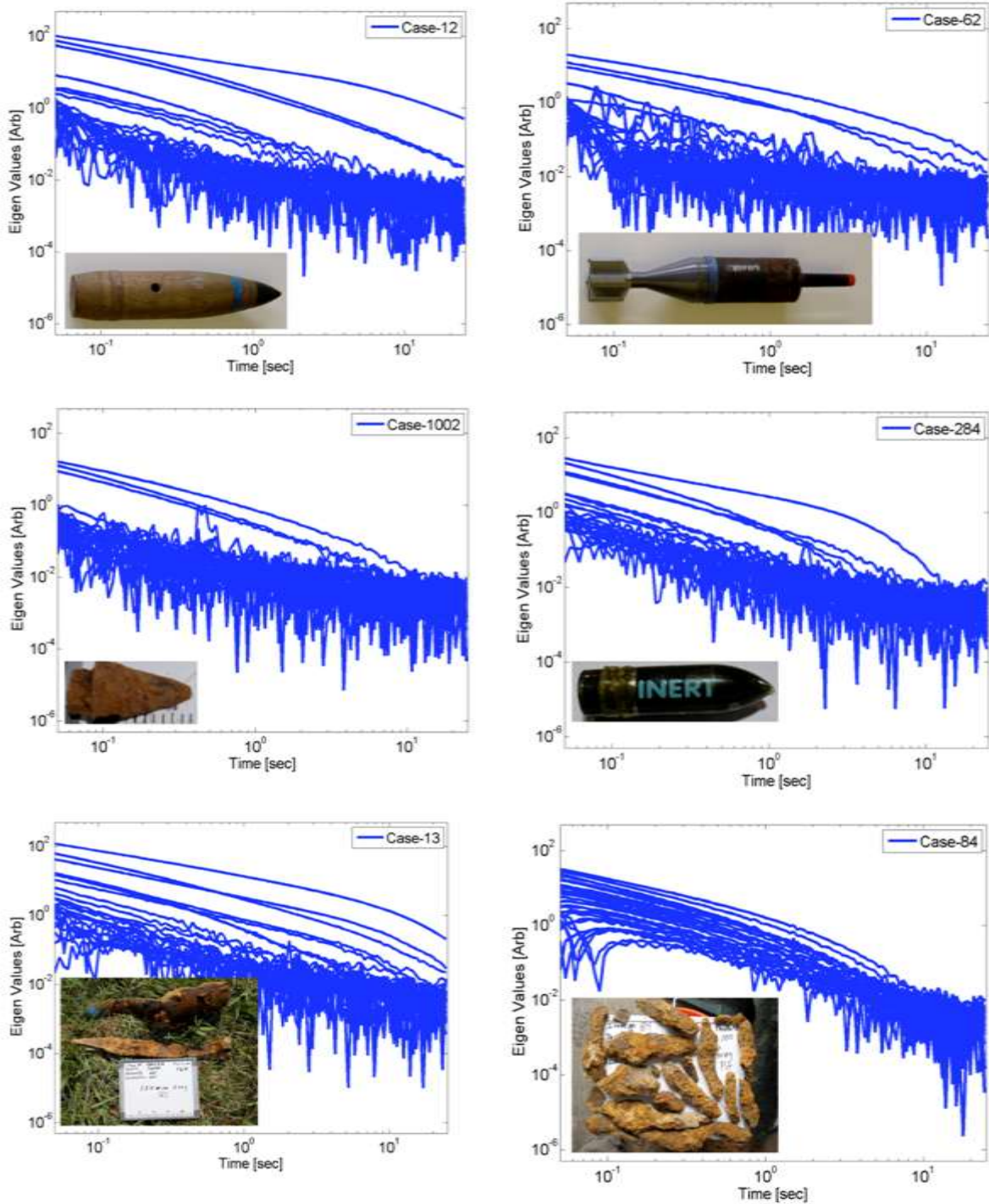versus time for some samples of requested anomalies.

Figure 3.57 : TEMTADS multi-static response matrix eigenvalues versus
time for a 105-mm HE projectile and a 105-mm HEAT round (top row),
an M-48 Fuze and a 37-mm munition (center row), and two clutter

scenarios, one with two items (left) and another with several (right) (third row).

In addition, based on the eigenvalues' time-decay characteristics we built a custom training list. For the most part, the list contained anomalies that had too many above-threshold eigenvalues, like the samples depicted in Figure 3.56. We requested two batches of training data. The first contained 65 anomalies, all of which were clutter; some had six eigenvalues above the noise level, while others had several eigenvalues mixed with the noise. The second batch consisted mostly of UXO. Once we had the ground truth for all 75 custom identified anomalies we proceeded to invert all TEMTADS data sets using a multi-target ONVMS algorithm combined with DE. We extracted the total ONVMS for every anomaly. Armed with the custom identified training list and the inverted total ONVMS for each case we created a library for M-48 fuzes and 37-mm projectiles without copper band. We did not request training data for either of the 105-mm UXO or for the 37-mm projectile with copper band because we already had TEMTADS test-stand data for these targets. The JD and ONVMS analysis clearly showed the presence of those items at the site. We implemented a library-matching technique in which we quantified the mismatch in total ONVMS between library samples and blind items and used it to classify UXO and non-UXO items. The inverted total ONVMS for the anomalies that were classified as 105-mm HE projectiles, 105-mm HEAT rounds, M-48 fuzes, and 37-mm UXO with and without a copper band are depicted in Figure 3.58 and Figure 3.59 All the inverted total ONVMS are seen to cluster well, and each target has a total ONVMS with features—such as its amplitude at the first time channel, its decay rate, or the separation between the primary (blue lines) and secondary (red and green lines) components at different time channels—that make it amenable to identification. (The most difficult differences to discern were between the M-48 fuzes figure 66 and the 37-mm projectiles without copper band of Figure 3.59). These features allowed us to classify targets as UXO or clutter and also let us sort the UXO by caliber. With this knowledge we created a prioritized dig list that we cross-validated using the time-decay curves of the JD eigenvalues.

The final prioritized dig list was submitted to the Institute for Defense Analyses (IDA) for independent scoring. The scored results were sent back in the form of a receiver operating characteristic (ROC) curve, which we depict in Figure 3.60. We can see that a) of the 75 targets that were dug for training, 68 targets were not TOI (shift along x-axis) and seven were (shift along y-axis); b) for 95% TOI classification (the pink dot in Figure 3.60) only seven extra (false positive) digs are needed; c) to classify all TOI correctly (the light blue dot) only 21 extra (false positive) digs are needed; d) for increased classification confidence the algorithm requested an additional thirty digs after all TOI had been identified correctly.
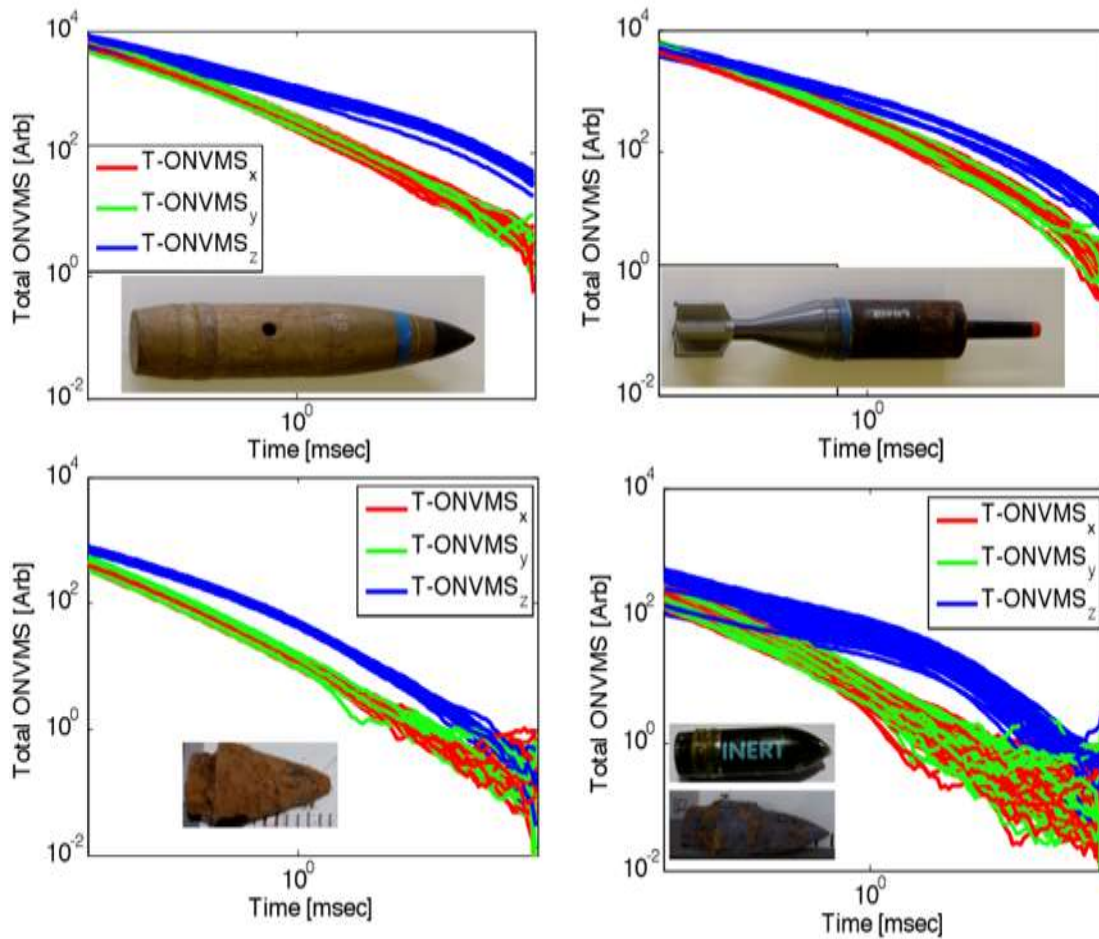
Figure 3.58: Inverted total ONVMS time-decay profiles for four
Camp Butner targets: (top row) 105-mm HE munition and 105-
mm HEAT round, and (bottom) M-48 Fuze and 37-mm
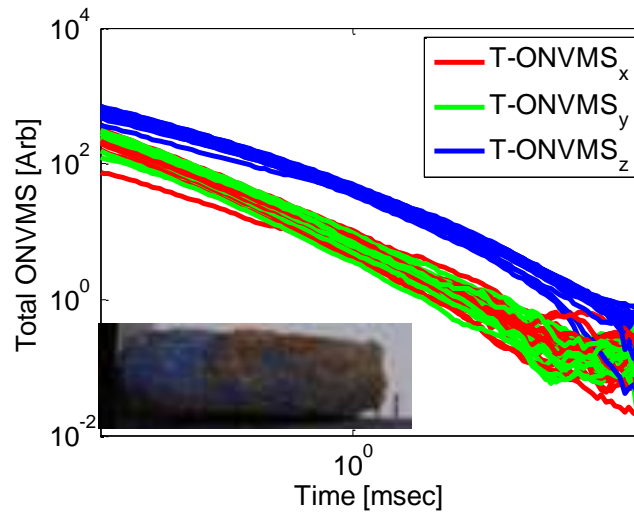projectile with copper band.

Figure 3.59: Inverted total cONSMS time decay profiles for a
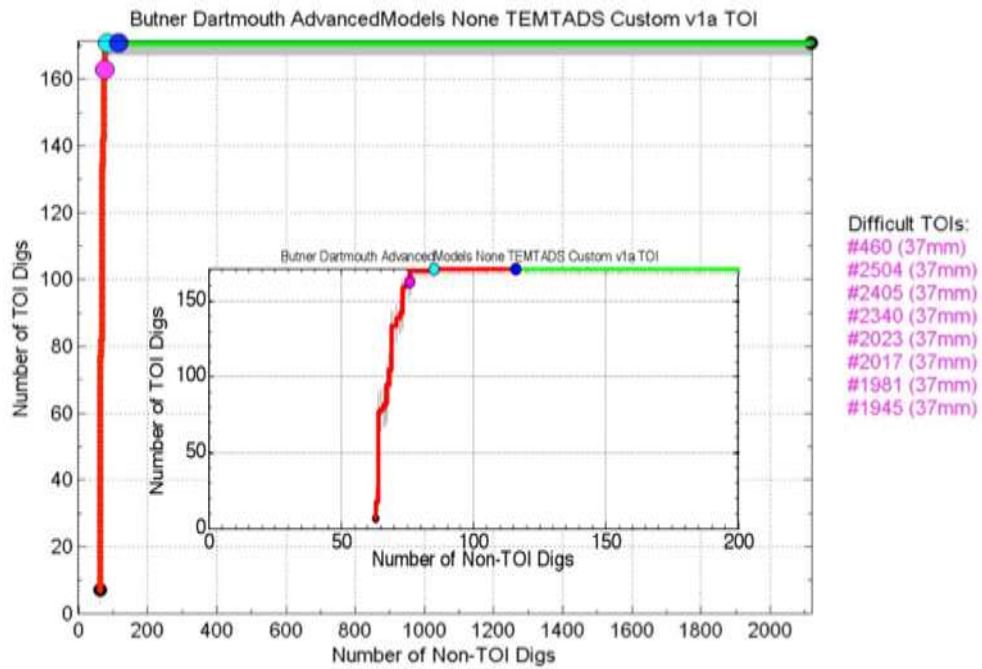37-mm projectile without copper band.

Figure 3.60: ROC curve for the Camp Butner TEMTADS test
data.

ii) MetalMapper data discrimination strategy and classification results using supervised clustering

All Camp Butner MM data sets were processed using a multi-object ONVMS/DE code. The combined procedure yields the total ONVMS for each anomaly, which, like the total NSMS, is intrinsic to the object it represents and can therefore be used for classification. As with the total NSMS, early-time ONVMS responses are associated with superficial eddy currents and thus directly proportional to the size of the object's surface, while late-time signals are due to volumetric currents and thus proportional to the target's entire volume.

These physics-based features were utilized in the supervised clustering algorithm. We used the ratio of the inverted total ONVMS at the 30th time channel to that at the first. The values of $\log_{10}[M_{zz}(t_1)/M_{zz}(t_{30})]$ vs. $\log_{10}[M_{zz}(t_1)]$ are plotted in figure 69(left) for all Camp Butner MM data sets. We see that the plotted quantities exhibit a wide spread of values. To use these features for statistical classification, and for determining clusters and a classification probability function, we started by dividing the scatter plot figure 69(left) into subsections. We then applied the Gaussian mixture model to each subsection assuming that there were five clusters. From the Gaussian mixture model we extracted the mean and standard deviations for each cluster and built a global classification probability function, depicted infigure 69 (right) that depended on the two feature parameters. The figure shows that there are 55 well-separated clusters. We next created a first custom training dig list that contained 55 anomalies, (i.e., one anomaly for each cluster) and requested the ground truth. The MM data for each scenario were inverted using the combined ONVMS-DE algorithm as though there were one, two, or three targets present, and the resulting total ONVMS amplitudes were compared. Whenever we spotted significant differences we examined the curves visually (a sample case is depicted in figure 70) and, based on this examination, requested the ground truth for an additional 60 datasets. Once we had the ground truth for a 121 custom training data set, we classified all targets as either TOI or non-TOI items using the probability function of Figure 3.61 The classification based on the supervised clustering is plotted in Figure 3.63: the red circles correspond to TOI, and the green dots to clutter.
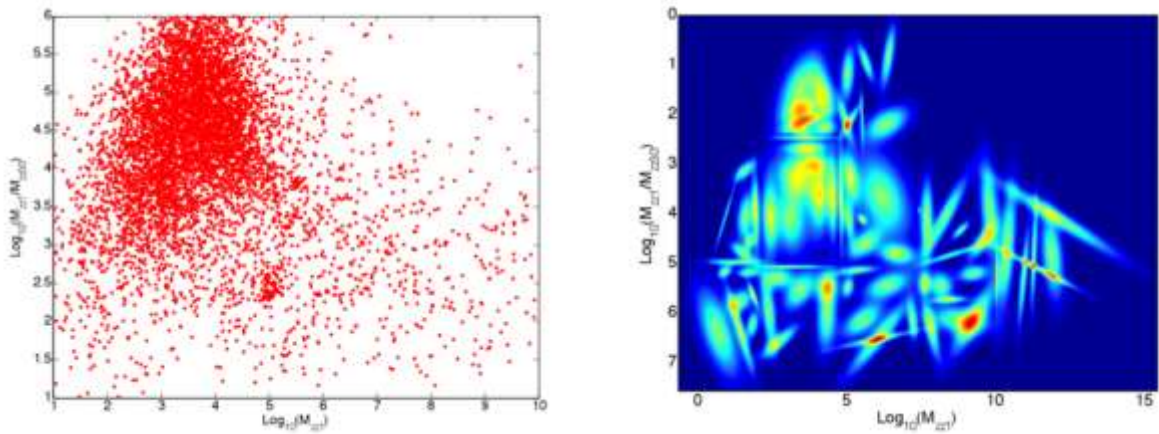
Figure 3.61: Left: Scatter plot for all MM anomalies based on the extracted total ONVMS. Right: Probability function for all MM anomalies.
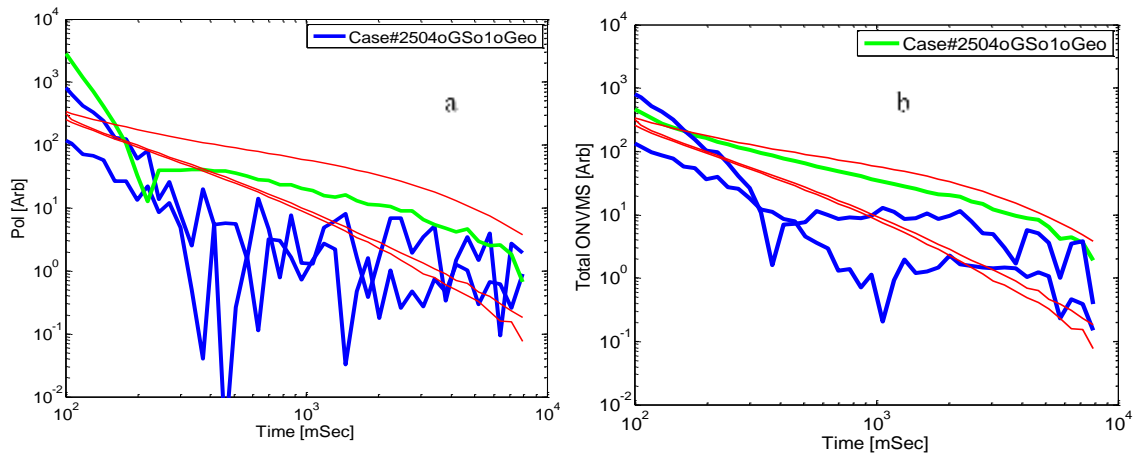
Figure 3.62: Inverted magnetic dipole polarizability (left) and total ONVMS (right) time-decay profiles for MM anomaly #2504. The thin red lines show a library sample, while the thick blue and green lines show the inversion results.
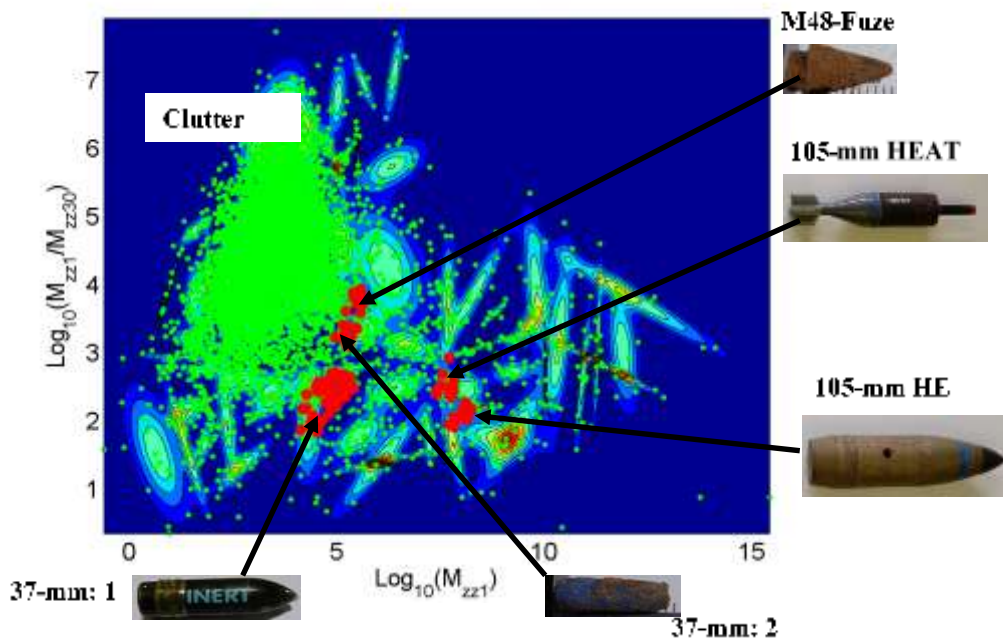
Figure 3.63: Result of the supervised clustering classification for the Camp Butner MM anomalies using the logarithms of M_{zz1} and M_{zz1}/M_{zz03}. The supervised clustering was trained with calibration data. The red markers correspond to clutter and the green ones to TOI.

We see that the Gaussian mixture model separates and clusters inverted parameters well. The clusters for the TOI are noticeably distinct from those of the others, suggesting that this two-dimensional feature space is appropriate for sound classification.

Using these results we created a prioritized dig list for the Camp Butner MM anomalies and again submitted the list to the Institute for Defense Analyses for scoring. Our classification results are summarized in the ROC curve of Figure 3.64. We see that a) of the 121 targets that were dug for training, 120 targets were not TOI (shift along x-axis) and one was (shift along y-axis); b) for 95% TOI classification (pink dot in Figure 3.64) eight extra (false positive) digs are needed; c) to classify all TOI correctly (light blue dot) only 32 additional digs are needed; d) for increased classification confidence the algorithm requested 33 additional digs after all the TOI were identified correctly.

Our classification results for both TEMTADS and MM were scored independently by the Institute for Defense Analyses. The scores we obtained reveal that our advanced models produce superb classification in all cases. There were no false negatives, and less than 5% of the anomalies had to be dug to achieve 100% correct classification. This is the third

time our advanced EMI and statistical models have shown successful classification performance on a realistic live-site blind test.
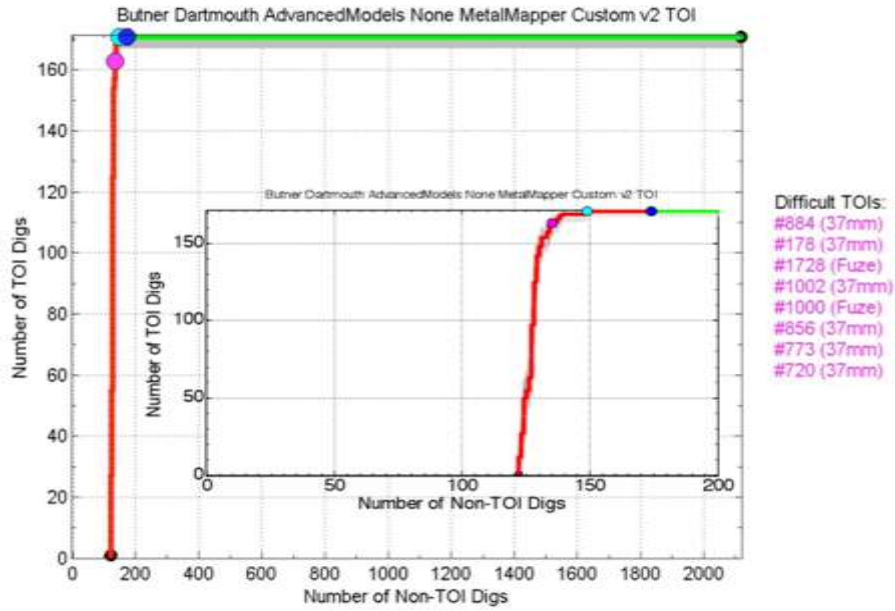
Figure 3.64: ROC curve for Camp Butner MetalMapper test data.
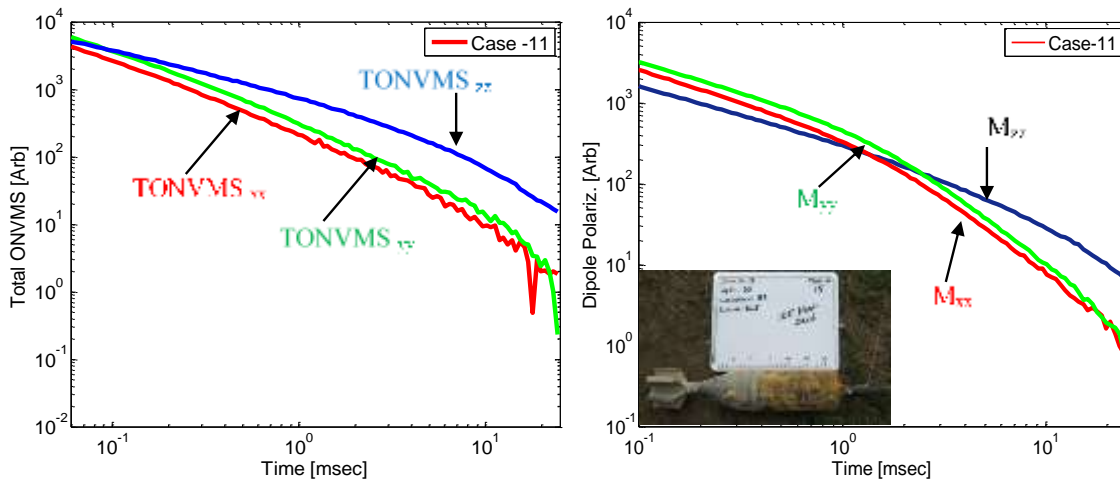
Figure 3.65: Left: Total ONVMS time-decay curves for a 105 mm projectile in the camp Butner, NC study. Right: Principal elements of the

polarizability tensor versus time for the same case.

iii) A Comparison between ONVMS and Dipole model

To illustrate the ONMVS superior classification performances over a simple dipole model, here we analyze extracted dipole polarizabilities and total ONVMS for 105 mm projectile. The data were collected at camp Beale, NC using the TEMTADS sensor. The object's intrinsic parameters were inverted using the ONVMS-DE and the simple dipole model-DE algorithms, with 100 iterations. The target dipole polarizability matrix and the total NSMS were determined and diagonalized using JD, and are illustrated in Figure 3.65. The results show that magnitudes of extracted dipole principal polarizabilities versus times are out of orders; namely, at early time gates amplitudes of the primary polarizability M_{zz} are less than the secondary M_{xx} and tertiary M_{yy} polarizabilities, while the TONVMS magnitudes have consistent orders for all time channels and provides good classification parameters.

Conclusions

My Theses supported the development of several innovative, robust, and noise-tolerant EMI forward models and statistical signal processing methodologies for use in subsurface target localization, characterization, and classification at live-UXO sites. In this thesis I have outlined the mathematical fundamentals, physical meaning, and practical realization of forward models such as the dipole model and the orthonormalized volume magnetic source (ONVMS) technique. Both of these procedures have been seen to provide an accurate representation of the EMI responses of subsurface metallic targets. The models were combined with data-inversion approaches—gradient search, direct search/differential evolution, and the like—to invert data collected by current advanced EMI sensors. We also developed and used the HAP method for estimating target locations directly. In addition, we explored several advanced statistical signal processing and classification approaches—support vector machines, Gaussian mixture models, etc.—as possible tools for discriminating UXO from non-hazardous anomalies.

We adapted every model we developed to a complete suite of next-generation sensors, including the MetalMapper, TEMTADS, MPV, and BUD. Comparison between gradient search, DE, and HAP showed DE to be the most robust, noise-tolerant and reliable method to determine extrinsic parameters of targets; the procedure, moreover, requires no regularization, and works quite well when confronted with multi-target cases. For these reasons we consider DE to be our foremost choice to estimate target location and orientation. The combination of DE with the NSMS and ONVMS models was extensively tested on actual data and provided excellent agreement with the ground truth at every instance, regardless of the number of targets in the cell. The models were further combined with state-of-the-art classification algorithms and applied to live-UXO sites.

Initially, we tested the NSMS-HAP-SVM and NSMS-HAP-Gaussian combinations on EM-63 data taken by ESTCP over 216 test cells at Camp Sibert in Alabama. The Gaussian mixture model provided excellent classification performance, with neither false

positives nor false negatives, while SVM had a tiny number of false alarms. In the next test we applied the NSMS-HAP and NSMS-DE combinations to TEMTADS data taken at the APG standardized test site. We found that the inverted classification feature parameters (the total NSMS in this case) were well-constrained for all objects and that the locations inverted using DE were in good agreement with the ground truth. There were 214 anomalies and six types of targets in the APG data set: 25-mm, 37-mm, 60-mm, 81-mm, and (two kinds of) 105-mm projectiles. For each cell we determined the total NSMS, extracted discrimination features from the NSMS decay curves, and classified the features using the Gaussian mixture model and a library-matching technique with the help of test-stand and calibration data. The results of independent scoring were the following: 1) All UXO were correctly identified as such and correctly identified by type/caliber. 2) There was a false positive rate of ~5%.

The classification abilities of the NSMS-HAP and NSMS-DE algorithms in combination with the Gaussian mixture model and library matching were again put to the test with data taken at Camp San-Luis Obispo in California using TEMATDS, MM, and BUD. There were four types of TOI: 60-mm, 81-mm, 2.36″, and 4.2″ munitions. Comparisons between the different methods demonstrated NSMS-DE to be more robust and stable than NSMS-HAP when extracting extrinsic parameters from to actual live-site data sets, particularly in multi-target cases. This made us adopt DE as our "official" procedure for target pinpointing. The blind test at SLO showed that NSMS-DE can be combined with the Gaussian mixture model and library matching to reliably classify single well-separated targets and anomalies with high SNR. However, the method was unable to identify all targets correctly (it missed respectively one, five, and one targets for MM, TEMATDS, and BUD). We then conducted a retrospective study that clearly demonstrated the main difficulties at the SLO site: a low SNR and the abundance of multi-target cases. To address those issues we extended the NSMS technique, developed the ONVMS model, and adapted the JD method to next-generation sensors.

The ONVMS model assumes that measured secondary fields are due to a volume distribution of interacting magnetic dipoles; the corresponding Green functions are Gram-Schmidt orthonormalized to avoid the ill-conditioning and instabilities that plague multi-object inversion and to make the method run faster. The JD technique, based on diagonalizing a multi-static response matrix and associating the number of eigenvalues above a certain threshold with the number of illuminated targets, is reliable and robust and, since it requires no inversion, essentially instantaneous. Additionally, the eigenvalues allow one to perform a preliminary target discrimination.

The resulting ONVMS-DE-JD combined technique was first used to conduct a retrospective analysis of the SLO data. After that we applied the procedure to yet another ESTCP blind test, this one held at Camp Butner, North Carolina, using the MetalMapper and TEMTADS instruments. The TEMATDS and MM data were analyzed independently of each other. The total time-dependent ONVMS was extracted, inverted, and classified for each cell using ONVMS-DE-JD and both the Gaussian mixture model and library matching. Our results, scored by the Institute for Defense Analyses, consistently demonstrated that our methods do a superb job of classifying anomalies. There were no

false negatives, and less than 5% of the anomalies had to be dug to achieve 100% correct classification. A high-quality automated UXO discrimination process based on machine-learning techniques has been demonstrated for reducing the expert workload and improving the process speed.

Both the SLO retrospective study and the Camp Butner blind test clearly demonstrated that the suite of advanced modeling and classification tools developed by our group are robust and noise-tolerant and provide excellent classification results using real-world data collected by next-generation EMI sensors. ONVMS proved superior to *NSMS and simple dipole model* for inversion and classification purposes and shall remain our preferred method of analysis. The ONVMS-DE-JD combination, supplemented by our classification algorithms, was further tested under ESTCP Project 201101 using MetalMapper, MPV, and 2×2 3D TEMATDS data collected at Camp Beale in California. Not only were the advanced EMI models able to classify all "easy seed UXO items", they also managed to identify all other targets, no matter how unexpected or site-specific, and as small as 3-cm fuzes [**Error! Reference source not found.**].

References

1. O. O. Bilukha, M. Brennan, and M. Anderson, "Injuries and deaths fromlandmines and unexploded ordnance in Afghanistan 2002–2006," *J. Amer.Med. Assoc.*, vol. 298, no. 5, pp. 516–518, Aug. 2007
2. I. Shamatava, F. Shubitidze, K. A. O'Neill, K. Sun, and K. D. Paulsen, "Simple magnetic charge model for representation of emi responses from a buried UXO," in *DIPED*, 2004, pp. 155-159.
3. F. Shubitidze, K. A. O'Neill, B. E. Barrowes, I. Shamatava, J. P. Fernández, K. Sun, and K. D. Paulsen, "Application of the normalized surface magnetic charge model to UXO discrimination in cases with overlapping signals," *Journal of Applied Geophysics,* vol. 61, pp. 292-303, 2007.
4. F. Shubitidze, K. ONeill, I. Shamatava, K. Sun, and K. D. Paulsen, "A simple magnetic charge model for classification of multiple buried metallic objects in cases with overlapping signals," in *SAGEEP*, 2005.
5. F. Shubitidze, K. A. O'Neill, I. Shamatava, K. Sun, and K. D. Paulsen, "Combined differential evolution and surface magnetic charge model algorithm for discrimination of UXO from non-UXO items: simple and general inversions," in *SPIE*, 2005, p. 346.
6. S. D. Billings, "Practical Discrimination Strategies for Application to Live Sites," presented at the SERDP and ESTCP Partners in Environmental Technology Technical Symposium & Workshop, Washington, DC, 2006.
7. Y. Zhang, L. M. Collins, H. Yu, C. E. Baum, and L. Carin, "Sensing of unexploded ordnance with magnetometer and induction data: Theory and signal processing," *IEEE Transactions on Geoscience and Remote Sensing,* vol. 41, pp. 1005-1015, 2003.
8. W. Hu, S. L. Tantum, and L. M. Collins, "EMI-based classification of

multiple closely spaced subsurface objects via independent component analysis," *IEEE Transactions on Geoscience and Remote Sensing,* vol. 42, pp. 2544-2554, Nov 2004.

9.　　E. Gasperikova, J. T. Smith, H. F. Morrison, A. Becker, and K. Kappler, "UXO detection and identification based on intrinsic target polarizabilities - A case history," *Geophysics,* vol. 74, pp. B1-B8, Jan-Feb 2009.

10. J. T. Smith and H. F. Morrison, "Optimizing receiver configurations for resolution of equivalent dipole polarizabilities in situ," *IEEE Transactions on Geoscience and Remote Sensing,* vol. 43, pp. 1490-1498, Jul 2005.

11. J. T. Smith and H. F. Morrison, "Estimating equivalent dipole polarizabilities for the inductive response of isolated conductive bodies," *IEEE Transactions on Geoscience and Remote Sensing,* vol. 42, pp. 1208-1214, Jun 2004.

12. T. H. Bell, B. J. Barrow, and J. T. Miller, "Subsurface discrimination using electromagnetic induction sensors," *IEEE Transactions on Geoscience and Remote Sensing,* vol. 39, pp. 1286-1293, 2001.

13. J. T. Miller, T. H. Bell, J. Soukup, and D. Keiswetter, "Simple phenomenological models for wideband frequency-domain electromagnetic induction," *IEEE Transactions on Geoscience and Remote Sensing,* vol. 39, pp. 1294-1298, 2001.

14. F. Shubitidze, B. E. Barrowes, J. P. Fernández, I. Shamatava, and K. A. O'Neill, "APG UXO discrimination studies using advanced EMI models and TEMTADS data," presented at the Detection and Sensing of Mines, Explosive Objects, and Obscured Targets XIV, Orlando, FL, 2009.

15. N. Geng, C. E. Baum, and L. Carin, "On the low-frequency natural response of conducting and permeable targets," *IEEE Transactions on Geoscience and Remote Sensing,* vol. 37, pp. 347-359, Jan 1999.

16. L.-P. Song, F. Shubitidze, L. R. Pasion, D. W. Oldenburg, and S. D. Billings, "Computing transient electromagnetic responses of a metallic object using a spheroidal excitation approach," *IEEE Geoscience and Remote Sensing Letters,* vol. 5, pp. 359-363, 2008.

17. J. P. Fernández, B. E. Barrowes, T. M. Grzegorczyk, N. Lhomme, K. A. O'Neill, and F. Shubitidze, "A Man-Portable Vector Sensor for Identification of Unexploded Ordnance," *IEEE Sensors Journal,* vol. 11, pp. 2542-2555, Oct 2011.

18. B. E. Barrowes, K. A. O'Neill, T. M. Grzegorczyk, X. Chen, and J. A. Kong, "Broadband analytical magnetoquasistatic electromagnetic induction solution for a conducting and permeable spheroid," *IEEE Transactions on Geoscience and Remote Sensing,* vol. 42, pp. 2479-2489, 2004.

19. B. E. Barrowes, K. A. O'Neill, D. D. Snyder, D. C. George, and F. Shubitidze, "New man-portable vector time domain EMI sensor and discrimination processing," 2006.

20. F. Shubitidze, K. A. O'Neill, I. Shamatava, K. Sun, and K. D. Paulsen, "Analysis of EMI scattering to support UXO discrimination: heterogeneous and multiple objects," 2003, p. 928.

21. F. Shubitidze, K. A. O'Neill, I. Shamatava, K. Sun, and K. D. Paulsen, "Use of standardized source sets for enhanced EMI classification of buried heterogeneous objects," 2004, p. 263.

22. F. Shubitidze, K. A. O'Neill, I. Shamatava, K. Sun, and K. D. Paulsen, "Fast and accurate calculation of physically complete EMI response by a heterogeneous metallic object," *IEEE Transactions on Geoscience and Remote Sensing,* vol. 43, pp. 1736-1750, 2005.

23. K. Sun, K. A. O'Neill, F. Shubitidze, I. Shamatava, and K. D. Paulsen, "Fast data-derived fundamental spheroidal excitation models with application to UXO discrimination," *IEEE Transactions on Geoscience and Remote Sensing,* vol. 43, pp. 2573-2583, 2005.

24. K. Sun, K. O'Neill, F. Shubitidze, S. A. Haider, and K. D. Paulsen, "Simulation of electromagnetic induction scattering from targets with negligible to moderate penetration by primary fields," IEEE Trans. Geosci.Remote Sensing, vol. 40, pp. 910–927, Apr. 2002.

25. F. Shubitidze, K. O'Neill, S. A. Haider, K. Sun, and K. D. Paulsen,"Application of the method of auxiliary sources to the wide-band electromagneticinduction problem," *IEEE Trans. Geosci. Remote Sens.*, vol. 40,no. 4, pp. 928–942, Apr. 2002.

26. F. Shubitidze, B. E. Barrowes, K. O'Neill, I. Shamatava, and J. Fernández, "NSMC for UXO discrimination in cases with overlapping signatures," pp. 65530F-1.

27. H. Braunisch, C. O. Ao, K. A. O'Neill, and J. A. Kong, "Magnetoquasistatic response of conducting and permeable prolate spheroid under axial excitation," *IEEE Transactions on Geoscience and Remote Sensing,* vol. 39, pp. 2689-2701, 2001.

28. P. Gao, L. Collins, P. M. Garber, N. Geng, and L. Carin, "Classification of landmine-like metal targets using wideband electromagnetic induction,"IEEE Trans. Geosci. Remote Sensing, vol. 38, pp. 1352–1361,2000.

29. L. Carin, H. Yu, Y. Dalichaouch, A. R. Perry, P. V. Czipott, and C. E.Baum, "On the wideband EMI response of a rotationally symmetry permeable and conducting target,"IEEE Trans. Geosci. Remote Sensing, vol. 39, pp. 1206–1213, June 2001.

30. J. He, T. Yu, N. Geng and L. Carin, "Method of moments analysis of electromagnetic scattering from a general three dimensional dielectric target embedded in a multi layered medium," Radio Science, vol. 35,pp. 305-313, Mar.Apr. 2000.

31. Bell, T., B. Barrow and J. Miller, "Subsurface Discrimination Uusing Electromagnetic Induction Sensors," IEEE Transactions on Geoscience and Remote Sensing , 39(6), pp. 1286-1293, June 2001.

32. Pasion, L. and D. Oldenburg, "A Discrimination Algorithm for UXO Using Time Domain Electromagnetics," J. Environmental and Engineering Geophysics, 6(2), pp. 91-102, June 2001

33. T. Bell, "Geo-location Requirements for UXO Discrimination", SERDP Project # MM0413, May 2008, http://www.dtic.mil/dtic/tr/fulltext/u2/a487619.pdf.

34. F. Shubitidze, J. P. Fernández, B. E. Barrowes, I. Shamatava, A. Bijamov, K. O'Neill, D. Karkashadze, "The Orthonormalized Volume Magnetic Source Model for Discrimination of Unexploded Ordnance," *IEEE Transactions on Geoscience and Remote Sensing,* vol 8, pp 5218-5229.

35. F. Shubitidze, J. P. Fernández, I. Shamatava, B. E. Barrowes, and K. O'Neill, "Joint diagonalization applied to the detection and discrimination of unexploded ordnance," *Geophysics*, vol. 77, no. 4, pp. WB149–WB160, 2012.

36. C. O. Ao, H. Braunisch, K. A. O'Neill, and J. A. Kong, "Quasi-magnetostatic solution for a conducting and permeable spheroid with arbitrary excitation," *IEEE Transactions on Geoscience and Remote Sensing,* vol. 40, pp. 887-897, 2002.

37. J. T. Smith, H. F. Morrison, and A. Becker, "Resolution depths for some transmitter-receiver configurations," *IEEE Transactions on Geoscience and Remote Sensing,* vol. 42, pp. 1215-1221, 2004.

38. B. E. Barrowes and H. Nelson, "Model-based characterization of electromagnetic induction signatures obtained with the MTADS electromagnetic array," *IEEE Transactions on Geoscience and Remote Sensing,* vol. 39, pp. 1279-1285, 2001.

39. L. Beran and D. W. Oldenburg, "Selecting a discrimination algorithm for unexploded ordnance remediation," *IEEE Transactions on Geoscience and Remote Sensing,* vol. 46, pp. 2547-2557, 2008.

40. F. Shubitidze, J. P. Fernández, I. Shamatava, L. R. Pasion, B. Barrowes, and K. O'Neill, "Application of the normalized surface magnetic source model to a blind unexploded ordnance discrimination test," *Applied Computational Electromagnetics Society Journal* 25, 89–98 (2010).

41. J. P. Fernández, K. Sun, B. E. Barrowes, K. A. O'Neill, I. Shamatava, F. Shubitidze, and K. D. Paulsen, "Inferring the location of buried UXO using a Support Vector Machine," presented at the Detection and Remediation Technologies for Mines and Minelike Targets XII, Bellingham, WA, 2007.

42. A. Aliamiri, J. Stalnaker, and E. L. Miller, "Statistical Classification of Buried Unexploded Ordnance Using Nonparametric Prior Models," *IEEE Trans. Geosci. Remote Sens.,* vol. 45, pp. 2794-2806, September 2007.

43. S. J. Hart, R. E. Shaffer, S. L. Rose-Pehrsson, and J. R. McDonald, "Using physics-based modeler outputs to train probabilistic neural networks for unexploded ordnance (UXO) classification in magnetometry surveys," *IEEE Transactions on Geoscience and Remote Sensing,* vol. 39, pp. 797-804, 2001.

44. F. Shubitidze, D. Karkashadze, B. E. Barrowes, I. Shamatava, and K. A. O'Neill, "A New Physics-based Approach for Estimating a Buried Object's Location, Orientation and Magnetic Polarization from EMI Data," *Journal of Environmental and Engineering Geophysics,* vol. 13, pp. 115-130, Sep 2008.

45. K. A. O'Neill, I. J. Won, A. Oren, F. Shubitidze, K. Sun, and I. Shamatava, "A new handheld vector EMI sensor with precise 3-D positioning," 2004.

46. E. Gasperikova, J. T. Smith, H. F. Morrison, and A. Becker, "Berkeley UXO Discriminator (BUD)," 2007.

47. L. M. Collins, Y. Zhang, J. Li, H. Wang, L. Carin, S. J. Hart, S. L. Rose-Pehrsson, H. H. Nelson, and J. R. McDonald, "A comparison of the performance of statistical and fuzzy algorithms for unexploded ordnance detection," *IEEE Transactions on Fuzzy Systems,* vol. 9, pp. 17-30, Feb 2001.

48. J. Byrnes, Ed., *Unexploded Ordnance Detection and Mitigation* (NATO Science for Peace and Security Series B: Physics and Biophysics. Dordrecht: Springer

Netherlands, 2009, p.^pp. Pages.

49. J. P. Fernández, B. E. Barrowes, K. A. O'Neill, K. D. Paulsen, I. Shamatava, F. Shubitidze, and K. Sun, "Evaluation of SVM classification of metallic objects based on a magnetic-dipole representation," presented at the Detection and Remediation Technologies for Mines and Minelike Targets XI, Bellingham, WA, 2006.

50. X. Chen, "Inverse problems in electromagnetics," 2005.

51. B. Zhang, K. A. O'Neill, J. A. Kong, and T. M. Grzegorczyk, "Support vector machine and neural network classification of metallic objects using coefficients of the spheroidal MQS response modes," *IEEE Transactions on Geoscience and Remote Sensing,* vol. 46, pp. 159-171, Jan 2008.

52. E. Bermani, A. Boni, S. Caorsi, and A. Massa, "An Innovative Real-Time Technique for Buried Object Detection," *IEEE Trans. Geosci. Remote Sensing,* vol. 41, pp. 927-931, April 2003.

53. A. Massa, A. Boni, and M. Donelli, "A Classification Approach Based on SVM for Electromagnetic Subsurface Sensing," *IEEE Trans. Geosci. Remote Sensing,* vol. 43, pp. 2084-2093, September 2005.

54. A. B. Tarokh, E. L. Miller, I. J. Won, and H. Huang, "Statistical classification of buried objects from spatially sampled time or frequency domain electromagnetic induction data," *Radio Science,* vol. 39, Jun 12 2004.

55. F. Shubitidze, K. O'Neill, I. Shamatava, K. Sun, and K. D Paulsen, "Implementation of hybrid MAS and SPA algorithm for broadband electromagnetic induction problems,", in Proc. 7th Int. Workshop Direct and Inverse Problems of Electromagnetic Acoustic Wave Theory Tbilisi, Georgia, Oct. 10 13, 2002

56. M. Prouty, "Detection and Classification with the MetalMapper™ at Former Camp San Luis Obispo," presented at the ESTCP Project No. MM-0603, Geometrics, Inc, 2009.

57. ESTCP, "2009 ESTCP UXO Classification Study, Former Camp San Luis Obispo, CA," presented at the Environmental Security Technology Certification Program Demonstration Plan, Arlington, VA, 2009.

58. ESTCP, "2010 ESTCP UXO Classification Study, Former Camp Butner, NC," presented at the Environmental Security Technology Certification Program Demonstration Plan, Arlington, VA, 2010.

59. H. Nelson, K. Kaye, and A. Andrews, "ESTCP Pilot Program, Classification Approaches in Munitions Response," in *Environmental Security Technology Certification Program*, Arlington, VA, 2007.

60. F. Shubitidze, "Camp Butner UXO Data Inversion and Classification Using Advanced EMI Models," presented at the SERDP and ESTCP Partners in Environmental Technology Technical Symposium & Workshop, Washington, DC, 2010.

61. A. Paski, "Former Camp Butner Site Description and EM61 Data Collection and Analysis," presented at the SERDP and ESTCP Partners in Environmental Technology Technical Symposium & Workshop, Washington, DC, 2010.

62. L. R. Pasion, "UXO Discrimination Using Full Coverage and Cued

Interrogation Data Sets at Camp Butner, NC," presented at the SERDP and ESTCP Partners in Environmental Technology Technical Symposium & Workshop, Washington, DC, 2010.

63. Y. Zhang, X. Liao, and L. Carin, "Detection of buried targets via active selection of labeled data: Application to sensing subsurface UXO," *IEEE Transactions on Geoscience and Remote Sensing,* vol. 42, pp. 2535-2543, 2004.

64. F. Shubitidze, J. P. Fernández, B. E. Barrowes, I. Shamatava, and K. A. O'Neill, "Normalized Surface Magnetic Source Model Applied to Camp Sibert Data: Discrimination Studies," presented at the Applied Computational Electromagnetics Symposium (ACES), Monterey, CA, 2009.

65. F. Shubitidze, J. P. Fernández, I. Shamatava, L. R. Pasion, B. E. Barrowes, and K. A. O'Neill, "Application of the Normalized Surface Magnetic Source Model to a Blind Unexploded Ordnance Discrimination Test," *Applied Computational Electromagnetics Society Journal,* vol. 25, pp. 89-98, Jan 2010.

66. Q. Liu, X. Liao, and L. Carin, "Detection of unexploded ordnance via efficient semisupervised and active learning," *IEEE Transactions on Geoscience and Remote Sensing,* vol. 46, pp. 2558-2567, Sep 2008.

67. I. Shamatava, F. Shubitidze, B. E. Barrowes, J. P. Fernández, and K. A. O'Neill, "Physically complete models applied to BUD time-domain EMI data," presented at the Detection and Sensing of Mines, Explosive Objects, and Obscured Targets XIV, Orlando, FL, 2009.

68. S. D. Billings, "Discrimination and classification of buried unexploded ordnance using magnetometry," *IEEE Transactions on Geoscience and Remote Sensing,* vol. 42, pp. 1241-1251, 2004.

69. R. E. Grimm, "Triaxial Modeling and Target Classification of Multichannel, Multicomponent EM Data for UXO Discrimination," *Journal of Environmental and Engineering Geophysics,* vol. 8, pp. 239-250, 2003.

70. J. D. McNeill and M. Bosnar, "Application of time domain electromagnetic techniques to UXO detection," 1996, pp. 34-42.

71. F. Shubitidze, D. Karkashadze, J. P. Fernández, B. E. Barrowes, K. O'Neill, T. M. Grzegorczyk, and I. Shamatava, "Applying a Volume Dipole Distribution Model to Next-Generation Sensor Data for Multi-Object Data Inversion and Discrimination," in *Proceedings of SPIE*, 2010.

72. D. Williams, Y. Yu, L. Kennedy, X. Zhu, and L. Carin, "A bivariate Gaussian model for unexploded ordnance classification with EMI data," *IEEE Geoscience and Remote Sensing Letters,* vol. 4, pp. 629-633, Oct 2007.

73. D. Williams, C. P. Wang, X. Liao, and L. Carin, "Classification of unexploded ordnance using incomplete multisensor multiresolution data," *IEEE Transactions on Geoscience and Remote Sensing,* vol. 45, pp. 2364-2373, Jul 2007.

74. F. Shubitidze, K. O'Neill, K. Sun, I. Shamatava, and K.D. Paulsen, "A hybrid full MAS and combined MAS-TSA algorithm for broadband electromagnetic induction problem", *Applied computational electromagnetic society Journal*, pages: 112-126, March, 2004

75. Y. Zhang, L. M. Collins, and L. Carin, "Unexploded ordnance detection using Bayesian physics-based data fusion," *Integr. Comput.-Aided Eng.,* vol. 10, pp.

231-247, 2003.

76. J. R. Wait, "A conducting sphere in a time varying magnetic field, "Geophysics, vol. 16, pp. 666–672, 1951.

77. J. R. Wait and K. P. Spies " Quasi-static Transient Response of a Conducting Permeable Sphere", GEOPHYSICS, October 1969, p. 789 792.

78. F. S. Grant and G. F. West, "Interpretation Theory in Applied Geophysics". New York: McGraw-Hill, 1965.

79. A. Sebak, L. Shafai, and Y. Das, "Near-zone fields scattered by three-dimensional highly conducting permeable objects in the field of an arbitrary loop,"IEEE Trans. Geosci. Remote Sensing , vol. 29, pp. 9–15, Jan. 1991.

80. V. Kupradze, "About approximates solution mathematical physics problem," in Success of Mathematical Sciences, vol. 22, Moscow, 1967,pp. 59–107.

81. R. S. Popovidi-Zaridze and Z. S. Tsverikmazashvili, "Numerical studyof a diffraction problems by a modified method of nonorthogonal series," in Zurnal. Vichislit. Mat. Mat Fiz., vol. 17, Moscow, 1977.

82. Y. Leviatan, A. Boag, and A. Boag, "Generalized formulations for electromagnetic scattering from perfectly conducting and homogeneous material bodies—Theory and numerical solution,"IEEE Trans. Antennas Propagat. , vol. 36, pp. 1722–1734, Dec. 1988.

83. Y. Leviatan and A. Boag, "Analysis of electromagnetic scattering from dielectric cylinders using a multifilament current model," IEEE Trans. Antennas Propagat. , vol. AP-35, pp. 1119–1127, 1987.

84. D. Karkashadze and R. Zaridze, "The method of auxiliary sources in applied electrodynamics," in LATSIS Symp., Zurich, 1995.

85. R. S. Zaridze, G. Bit-Babik, K. Tavzarashvili, D. P. Economou, and N. K. Uzunoglu, "Wave field singularity aspects in large-size scatterers and inverse problems," *IEEE Transactions on Antennas and Propagation,* vol. 50, pp. 50-58, 2002.

86. K. Tavzarashvili, C. Hafner, X. D. Cui, R. Vahdieck, D. Karkashadze, and G. Ghvedashvili, "Model-based parameter estimation (MBPE) for metallic photonic crystal filters," *Applied Computational Electromagnetics Society Journal,* vol. 22, pp. 228-235, Jul 2007.

87. N. Bliznyuk, R. J. Pogorzelski, and V. P. Cable, "Localization of Scattered Field Singularities in Method of Auxiliary Sources," in *Proceedings of the IEEE AP-S/URSI Symposium*, 2005.

88. A. G. Kyurkchan, B. Y. Sternin, and V. Shatalov, "Singularities of continuation of wave fields," *Physics-Uspekhi,* vol. 39, p. 1221, 1996

89. J. D. Jackson, *Classical Electrodynamics*, 3rd ed. New York: Wiley, 1999.

90. G. A. Korn and T. M. Korn, *Mathematical Handbook for Scientists and Engineers*. New York: McGraw-Hill, 1968.

91. J. E. Gentle, *Matrix algebra : theory, computations, and applications in statistics*. New York, N.Y. ; London: Springer, 2007.

92. P. Comon, "Independent Component Analysis, a New Concept," *Signal Processing,* vol. 36, pp. 287-314, Apr 1994.

93. A. Belouchrani, K. AbedMeraim, J. F. Cardoso, and E. Moulines, "A blind source

separation technique using second-order statistics," *IEEE Transactions on Signal Processing,* vol. 45, pp. 434-444, Feb 1997.

94. S. Harmeling, A. Ziehe, M. Kawanabe, and K. R. Muller, "Kernel-based nonlinear blind source separation," *Neural Computation,* vol. 15, pp. 1089-1124, May 2003.

95. B. N. Flury and W. Gautschi, "An Algorithm for Simultaneous Orthogonal Transformation of Several Positive Definite Symmetrical-Matrices to Nearly Diagonal Form," *Siam Journal on Scientific and Statistical Computing,* vol. 7, pp. 169-184, Jan 1986.

96. J. F. Cardoso and A. Souloumiac, "Jacobi angles for simultaneous diagonalization," *Siam Journal on Matrix Analysis and Applications,* vol. 17, pp. 161-164, Jan 1996.

97. R. Storn and K. Price, "Differential evolution - A simple and efficient heuristic for global optimization over continuous spaces," *Journal of Global Optimization,* vol. 11, pp. 341-359, Dec 1997.

98. R. Storn, "System design by constraint adaptation and differential evolution," *IEEE Transactions on Evolutionary Computation,* vol. 3, pp. 22-34, 1999.

99. D. W. Marquardt, "An Algorithm for Least-Squares Estimation of Nonlinear Parameters," *Journal of the Society for Industrial and Applied Mathematics,* vol. 11, pp. 431-441, 1963.

100. K. Levenberg, "A method for the solution of certain problems in least squares," *Quarterly of Applied Mathematics,* vol. 2, pp. 164-168, 1944.

101. J. E. Dennis and R. B. Schnabel, *Numerical methods for unconstrained optimization and nonlinear equations*. Philadelphia: Society for Industrial and Applied Mathematics, 1996.

102. M. V. Berry, "Waves as catastrophes," *Physics Bulletin,* vol. 107, p. 108, 1976.

103. V. I. Arnold, *Catastrophe theory*: Springer, 1992.

104. J. A. Stratton, *Electromagnetic theory*, 1st ed. New York, London,: McGraw-Hill book company, inc., 1941.

105. A. J. van der Veen, M. C. Vanderveen, and A. Paulraj, "Joint angle and delay estimation using shift-invariance techniques," *IEEE Transactions on Signal Processing,* vol. 46, pp. 405-418, Feb 1998.

106. I. J. Won, D. A. Keiswetter, and T. H. Bell, " Electromagnetic induction spectroscopy for clearing landmines," IEEE Trans. Geosci. Remote Sensing, vol. 39, pp. 703-709, Apr. 2001

107. E. Demidenko, *Mixed models : theory and applications*. Hoboken, N.J.: Wiley-Interscience, 2004.

108. T. W. Anderson, *An introduction to multivariate statistical analysis*: John Wiley & Sons, 1958.

109. G. A. F. Seber and C. J. Wild, *Nonlinear regression* vol. 503: LibreDigital, 2003.

110. T. F. Cox and M. A. A. Cox, *Multidimensional scaling*, 2nd ed. Boca Raton: Chapman & Hall/CRC, 2001.

111. R. O. Duda, P. E. Hart, and D. G. Stork, *Pattern classification* vol. 2: wiley New York, 2001.

112. A. C. Rencher, *Methods of multivariate analysis*: Wiley New York, 1995.

113. B. D. Ripley, *Pattern recognition and neural networks*: Cambridge Univ Pr, 2008.

114. J. Chen and X. Tan, "Inference for multivariate normal mixtures," *Journal of Multivariate Analysis,* vol. 100, pp. 1367-1383, 2009.

115. C. Cortes and V. N. Vapnik, "Support-Vector Networks," *Machine Learning,* vol. 20, pp. 273-297, Sep 1995.

116. A. J. Smola and B. Schölkopf, "A tutorial on support vector regression," *Statistics and Computing,* vol. 14, pp. 199-222, August 2004.

117. C.-W. Hsu and C.-J. Lin, "A Comparison of Methods for Multiclass Support Vector Machines," *IEEE Trans. Neural Netw.,* vol. 13, pp. 415-425, 2002.

118. M. A. Aizerman, E. M. Braverman, and L. I. Rozonoer, "Theoretical foundations of the potential function method in pattern recognition learning," *Automation and Remote Control,* vol. 25, pp. 821-837, 1964.

119. C. J. C. Burges, "A Tutorial on Support Vector Machines for Pattern Recognition," *Data Mining and Knowledge Discovery,* vol. 2, pp. 121-167, 1998.

120. O. L. Mangasarian and D. R. Musicant, "Lagrangian Support Vector Machines," *Journal of Machine Learning Research,* vol. 1, pp. 161-177, March 2001.

121. J. Mercer, "Functions of positive and negative type and their connection with the theory of integral equations," *Philos. Trans. Roy. Soc. London, A,* vol. 209, pp. 415-446, 1909.

122. E. Bermani, A. Boni, A. Kerhet, and A. Massa, "Kernels evaluation of SVM-based estimators for inverse scattering problems," *Progress in Electromagnetic Research,* vol. 53, 2005.

123. U. Kreßel, "Pairwise classification and Support Vector Machines," in *Advances in Kernel Methods: Support Vector Learning*, B. Schölkopf*, et al.*, Eds., ed Cambridge, MA: MIT Press, 1999, pp. 255-268.

124. C.-C. Chang and C.-J. Lin, "(LIBSVM): a library for support vector machines," 2001.

125. N. Cristianini and J. Shawe-Taylor, *An Introduction to Support Vector Machines and other Kernel-Based Learning Methods*. Cambridge: Cambridge University Press, 2000.